3D Image Analysis and Microstructure Models for Simulation of Materials Properties

by
Dascha Dobrovolskij

A dissertation submitted in fulfillment of the requirements for the degree of
— Dr. Ing. —

1st supervisor:	Prof. Dr. P. Maaß
2nd supervisor:	Prof. Dr. H.-G. Stark
Patronate:	Dr. Ronald Rösch
Submission date:	02.04.2024
Date of oral exam:	15.05.2024

Fachbereich 3 - Mathematik und Informatik
Bibliothekstraße 5 | D-28359 Bremen
https://www.uni-bremen.de/fb3

"Man ist sozusagen selbst nur ein Instrument, auf dem das Universum spielt."
Gustav Mahler

Abstract

The rising availability of computational power allows for a steady improvement of simulation techniques. As the awareness for the limits of our natural resources increases, the use of numerical simulation for understanding existing materials and their mechanical behavior is receiving increasing attention. Recently, Diebels and Rjasanow 2019 incorporate knowledge about a material (glass fiber reinforced polymers) w.r.t. the physical scale into a multi-scale approach, leading to a chain of conclusions. They study the microstructure of the composite material on the microscale, develop modelling and simulation techniques for mechanical properties on the micro- and macro scale. Microstructure models help us to gain knowledge at one scale and deducing to the following. In this context, this work contributes to the exploration of mechanical properties of microscopically heterogeneous materials.

I analyze 2D or 3D data of materials' microstructure by means of stochastic geometry and fit geometric microstructure models. First, I model polycrystalline metals using a Laguerre tessellation. Second, glass fiber reinforced polymers are modeled by a union of cylinders. This modelling step enables the connection between a geometrical microstructure model and a simulation of mechanical properties of microscopically heterogeneous materials.

In ultrasonic non-destructive testing, the scattering theory (Hirsekorn 2014) originally predicts the scattering in a polycrystal w.r.t. grain mean diameters and the frequency of an ultrasonic wave. I implement a new simulation technique for the computation of a scattered ultrasonic time-domain signal in a fitted Laguerre tessellation. Hence, this approach allows to simulate the noise which appears in ultrasound signals caused by microstructers. An investigation of scattering due to microstructural variation in a polycrystal is now possible, which should be employed in context of non-destructive material testing in the future.

Destructive sample extraction from composite components for estimation of fiber orientation distribution belongs to the state-of-the-art. We demonstrate success in two main scenarios: First, virtual experiments for tensile tests now can replace destructive tensile testing. Second, we demonstrate that truly non-destructive scanning of regions of interests is now possible.

Zusammenfassung

Die zunehmende Verfügbarkeit von Rechenleistung ermöglicht eine beständige Verbesserung von Simulationswerkzeugen. Das ansteigende Bewusstsein für Ressourcenknappheit erzwingt die Integration der Simulationswerkzeuge, um die vorhandenen Werkstoffe besser zu verstehen. Diebels and Rjasanow 2019 integrieren in einem Multiskalenansatz das Wissen über ein Material (glasfaserverstärkte Polymere) in Bezug auf die physikalische Skala und bilden so eine Kette von Schlussfolgerungen. Sie untersuchen die Mikrostruktur des Verbundwerkstoffs auf der Mikroskala und entwickeln Modellierungs- und Simulationstechniken für mechanische Eigenschaften auf der Mikro- und Makroskala. Dieser Ansatz profitiert durch Mikrostrukturmodelle, da diese dazu beitragen, den Werkstoff auf einer Skala zu verstehen, um somit das Wissen auf die nächste Ebene zu übertragen. Damit trägt diese Arbeit zur Erforschung der mechanischen Eigenschaften von mikroskopisch heterogenen Materialien bei.

Ich analysiere 2D- oder 3D-Daten der Mikrostruktur von Werkstoffen auf Basis der stochastischen Geometrie und passe geometrische Mikrostrukturmodelle an. Zum einen modelliere ich polykristalline Metalle durch ein Laguerre-Mosaik. Zum Zweiten werden die glasfaserverstärkten Polymere durch eine Vereinigung von Zylindern modelliert. Dieser Modellierungsschritt gewährleistet die Schnittstelle zwischen den Mikrostrukturen und einer Simulation von mechanischen Eigenschaften der mikroskopisch heterogenen Materialien.

Mithilfe der Streutheorie (Hirsekorn 2014) kann die Streuung in einem Polykristall abhängig vom mittleren Korndurchmesser und der Frequenz der Ultraschallwelle geschätzt werden. Ich implementiere ein neues Simulationsverfahren zur Berechnung des gestreuten Ultraschallsignals in der Zeit-Domäne in einem angepassten Laguerre-Mosaik, was eine Untersuchung des simulierten mikrostrukturellen Rauschens ermöglicht. Eine Untersuchung der Streuung aufgrund mikrostruktureller Variationen

in einem Polykristall ist nun möglich, was in Zukunft im Rahmen der zerstörungsfreien Materialprüfung eingesetzt werden soll

Die zerstörungsfreie Probenentnahme aus Verbundbauteilen zur Abschätzung der Faserorientierungsverteilung gehört zum Stand der Technik in Wissenschaft und Produktionsumgebung. Wir demonstrieren Erfolg in zwei Szenarien: Virtuelle Zugversuche können nun die realen Experimente ersetzen; wirklich zerstörungsfreies Scannen und Analysieren der interessierenden Regionen ist nun möglich.

Acknowledgement

I need to thank my family for endless support. I am grateful for this unconditional love. Also, I need to thank my second family, with Katja Schladitz and Jörg Wenzel ahead. Katja, it was a pleasure to have this mixture of work, spending free time and in general running life with you. I appreciate the many helpful talks with you and the proofreading done by you.

I have enjoyed the great support of Ronald Rösch. It was a pleasure to work with my supervisors, Hans-Georg Stark and Peter Maaß. Also, I need to thank Martin Spies, for providing the initial topic idea of the ultrasonic scattering in polycrystals. I would like to thank Sigrun Hirsekorn for the trust and the valuable explanations and discussions regarding the scattering theory. I would also like to thank Claudia Redenbach for her attentive manner and some advice during my work. Also, I appreciate the support by Joachim Ohser and Markus Rauhut.

At different stages of this thesis, I have worked at different institutions, where I've been able directly or indirectly to continue. I need to acknowledge the following places: Fraunhofer-Institut für Techno- und Wirtschaftsmathematik in Kaiserslautern, Fraunhofer-Institut für Zerstörungsfreie Prüfverfahren in Saarbrücken, Deutsche Gesellschaft für Zerstörungsfreie Prüfung in Berlin, Hochschule Darmstadt, Technische Hochschule Aschaffenburg, Hochschule Kaiserslautern, and of course Universität Bremen.

After all this, I know about my stubbornness as well as about my patience, which are sometimes curse and blessing at the same time. Thank you to all my friends, especially to Tobias Bühler and Oliver Wirjadi. Oliver, thank you for your patience and the proofreading, you have done. All of you are great companions.

Contents

1 Introduction

The fast technological progress impacts our life strongly in many ways. On the one side, the technical and aesthetic requirements on construction elements grow. Simultaneously, the demand for more reliable and exact testing techniques to ensure the increased quality requirements rises. Moreover, the apparent limitation of various resources drives the need for long-lasting and well constructed products. On the other side, computational power increases rapidly and computational techniques improve. These developments call and allow for mirroring all design, construction, and production steps, as well quality management in the virtual world.

Hawking and Mlodinow 2010 discuss the general idea of a scientific model which describes a particular subject. The authors claim that humans cannot be absolutely certain about any subject, and thus the models should be measured by their usefulness. Thus, the desired models should be as sophisticated as needed to describe the specific subject, but not more than required.

This requires for structure models and simulation methods suitable to the physical scale where the question arises. More precisely, the detailedness and accuracy of a microstructure model or a simulation technique is useful w.r.t. the problem solution and the corresponding physical scale, and is inefficient in the best case or is even useless otherwise. Typically, a product evolves in a sequence of production stages, i.e. starting with design and selection of materials, subsequently predicting product properties and finally allowing for a robust, objective, and reproducible quality assurance. This leads to the incorporation of models and methods at distinct production stages and enforces a multi-scale approach (Diebels and Rjasanow 2019). Diebels and Rjasanow 2019 demand a bottom-up validation of physical scale levels, where a level is validated by data and analysis from lower scales.

In general, Figure 1 emphasizes the common idea of the contributing publications in this thesis. I analyze material images which depict material structure at a nm-µm

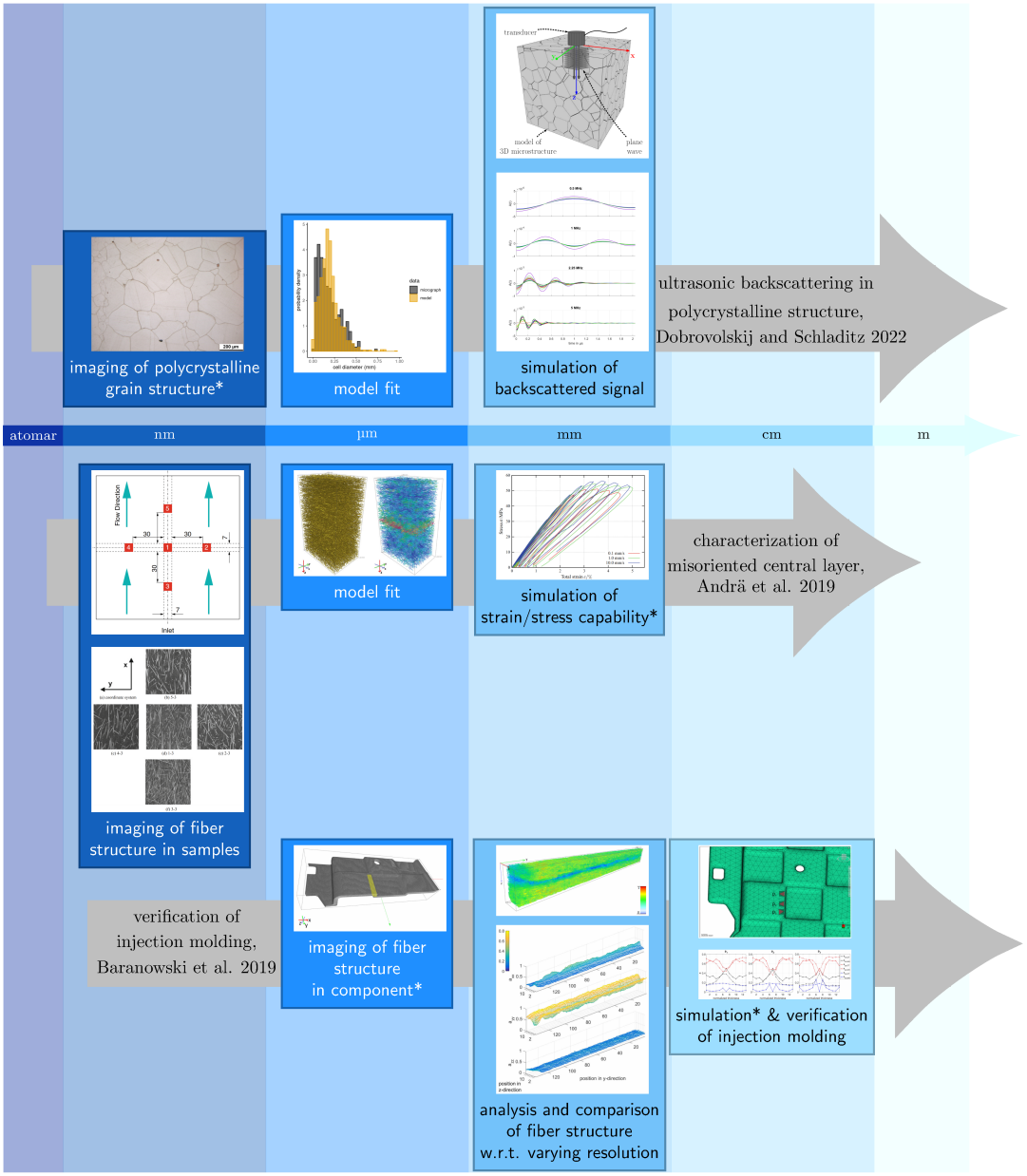

Figure 1: Visual summary of the contributions Dobrovolskij and Schladitz 2022, Andrä et al. 2019, and Baranowski et al. 2019. The scale axis is divided in sections, which are marked by different shades of blue. Each of these sections marks distinguished parts of my work. * identifies parts of work contributed by project partners. The reader is invited to take a look into the contributions for images in better resolution.

level, and derive microstructure models at the next physically larger level (µm-mm). Then, the microstructure model fits in to a simulation routine and therefore allows for material behavior prediction. This approach blends well into the multi-scale

modelling, as discussed by Diebels and Rjasanow 2019.

Virtual, digital or computational material design is an entire research area aiming to study real world materials in a virtual environment, see e.g. Huber et al. 2022; Jeulin 2021; Lee 2016. This approach saves material resources, on the one hand, but requires virtual representations of both the real material and the experimental set-up, on the other hand. Every real world material requires its own handling, including structural modelling as well as the simulation of desired material properties. This implies a variety of material models as large as the real world materials' variety.

In this context, two main applications give the motivation for the investigations, which I present here. The following publications deal with materials whose properties are determined to a significant extent by geometric or crystallographic properties.

First, polycrystalline metallic alloys are fundamental for many construction elements where the weight is negligible but extreme load bearing capabilities and long life cycles are demanded. Polycrystals form a system of grains whose size distribution is a decisive feature for the material's macroscopic behavior. Ultrasonic testing is a non-destructive testing technique where an ultrasonic wave of a certain frequency propagates in the material and reflects whenever the wave faces obstacles, i.e. defects. The propagating wave is scattered by the polycrystalline grain structure, causing energy loss and velocity fluctuations. Thus, defect detection and evaluation gets more difficult the more the propagating wave interacts with the polycrystalline microstructure due to its wavelength (Mason and McSkimin 1947, Truell et al. 1969, Stanke and Kino 1984). A 3D tessellation of a volume parcels space in a structure similar to the polycrystalline structure, with grains and boundaries between them (Alpers et al. 2015, Šedivỳ et al. 2018). For our application, the main idea is to find an appropriate 3D tessellation as a representative of a single phase polycrystal, and to use this 3D tessellation for simulation of ultrasonic backscattering.

Simulation techniques allow for prediction of scattering effects and thus support a deeper understanding of ultrasonic wave propagation in polycrystalline media. Recently, realistic models for polycrystalline microstructure have become computationally more accessible. The upper row of Figure 1 gives a short visual summary of my work regarding this application. Figure 1 references the publications Dobrovolskij and Schladitz 2022, Andrä et al. 2019, and Baranowski et al. 2019. Each of

the gray arrows indicates the work flow of the corresponding publication.

Second, glass fiber reinforced polymers (GFRP) are widely used in production of construction elements where light weight and strength are requested. Glass fibers are thin and long and usually embedded in a macroscopically homogeneous polymer matrix. Thus, this composition improves the load bearing capability of the material in certain directions. The orientation distribution of embedded fibers mainly determines the load which can be resisted by the material and thus needs to be controlled and analyzed.

Injection molding is a complex process in which the liquid material flows, cools down, and finally forms the desired part. This process determines the orientation of the incorporated glass fibers. During the molding process, the liquid material is injected at designated points. Fibers align with the flow. However, rheological effects and fiber-fiber-interactions cause deviations from this general rule (Yasuda et al. 2005). The difficulty of controlling and predicting the resulting spatial distribution of the fibers increases with the complexity of the shape of the component, the fiber volume content, and the fiber length. In principle, the local fiber orientation can be analyzed by the analysis of polished 2D sections (Chiu et al. 2013, Section 11.6.4). A sliced fiber of circular cross-section appears as an ellipse in a 2D section, and thus the orientation of this fiber can be estimated. The estimated orientation is however not unique, and small errors in the 2D sections can lead to large estimation errors. X-ray micro computed tomography allowing for analysis of the fiber component in 3D and at high resolutions is therefore highly preferable.

The misalignment of fibers needs to be understood. Furthermore, it is still a challenge to derive locally well resolved orientation estimation in large components without extracting samples of a size that actually means destroying the component. This application is addressed in two publications, see Figure 1 in the lower two rows.

In both applications, GFRP and polycrystalline metals, I use image processing algorithms in order to analyze either 2D or 3D images of the real material's microstructure. A wide variety of tools had to be used and assembled into complex and widely differing algorithms as images from four imaging methods had to be processed, while the general workflow for all these tasks is similar. Moreover, the analysis aimed at different goals, too – size and shape distributions of compact objects on the one hand and local orientation distribution of a fibrous component on the other.

The derived geometric properties enable the next step: setting up the model that represents the real material virtually. In both applications, stochastic geometry (Jeulin 2021) provides the necessary mathematical tools. Randomly packed straight cylinders model the fibrous component of the GFRP material. The model allows for a broad variation of its parameters, i.e. length and thickness of fibers, volume fraction of the fiber component, and mean fiber orientation. A random Laguerre tessellation models the polycrystalline microstructure, where cells represent grains. The grain volume distribution determines the polycrystal's microstructure. Thus, a change of cell volume distribution allows adapting the virtual model to the observed real polycrystal.

My personal contribution also comprises simulation of materials properties in the first application. Here, I interpret the analytical scattering coefficients grain-wise and establish a previously non-existent relationship between them and a numerical approximation method for ultrasonic wave propagation. This method allows studying ultrasonic scattering depending on both frequency and microstructure.

1.1 Structure of the Thesis

This manuscript is designed in two main parts: the preliminary part and the second part consisting of three attached published articles. The preliminary part offers the reader a description of a framework with a fundamental understanding of analysis and modeling of microstructures. Also, we describe the interface between microstructure modelling and the simulation tools. More precisely, the first part consists of three chapters. In chapter 2, I present the mathematical background required for geometric analysis and modelling of microstructures. The applications with the specific process of data analysis and modelling, as well as the simulation of material properties, follow up in chapter 3. In the last chapter 4, I summarize the diverse results, draw the conclusion, and give a short outlook regarding the applications.

The preliminary part does not contain figures, but the publications in the second part of this thesis contain several illustrative opportunities. I might invite the reader to take a look for better understanding into the publications.

1.2 Publications and Contributions of the Author

Ultrasonic Backscattering in Polycrystalline Microstructures, Dobrovolskij and Schladitz 2022

Dobrovolskij, D. and K. Schladitz (2022). "Simulation of Ultrasonic Backscattering in Polycrystalline Microstructures". In: MDPI Acoustics 4, pp. 139–167.

Contribution

This peer reviewed work is almost completely mine, except for two aspects. First, the input image data comes from external institutions. Second, K. Schladitz guided and supervised the publication process.

Publication Status and Availability

Published as a full length and open access article in a special issue "Elastic Wave Scattering in Heterogeneous Media" of Acoustics Journal of Multidisciplinary Digital Publishing Institute (MDPI).

Description

I analyze two single-phase polycrystals: a fine-grained titanium based on 3D computed X-ray diffraction data, and a coarse-grained Inconel-617 based on 2D light-microscopic images of planar sections. Then, we fit to each of both polycrystals a Laguerre tessellation. These parametrized models allow to generate realizations with adjustable number of cells and cell size distribution. This enables studying the interaction of the microstructure with ultrasonic waves by numerical simulations.

I propose a completely new simulation approach for computing a backscattered time-domain ultrasonic signal. Assuming a testing frequency, this simulation of a propagating ultrasonic wave accounts for backscattering contributions from each single cell. We superpose all the contributions at a receiver position and derive a backscattering response from the microstructure. Based on the simulation results, I conclude, that the mean grain diameter of a polycrystal does not suffice to explain the microstructural ultrasonic noise. This contradicts common knowledge specific to the ultrasonic testing community. Consequently, the testing frequency should be chosen not only depending on the mean grain diameter, but on the entire grain volume distribution.

Fiber Orientation Analysis in Injection Molded Samples, Andrä et al. 2019

Andrä, H., **D. Dobrovolskij**, K. Schladitz, S. Staub, and R. Müller (2019). "Modelling of Geometrical Microstructures and Mechanical Behaviour of Constituents". In "Multi-scale Simulation of Composite Materials: Results from the Project MuSiKo", Springer, pp. 31–56.

Contribution

I planned and revised the acquisition of 3D image data based on the sample provided by project partners. I analyzed the image data, passed on required parameters to project partners, and wrote an essential part of the contribution.

Publication Status and Availability

This chapter belongs to a book, which is dedicated to recent insights in the field of engineering and understanding of GFRP.

Description

We analyzed a sequence of five samples from an injection molded plate with a constant plate thickness of 2 mm. The plate material consists of 20 weight percent short glass fibers which are embedded in a polybutylene terephthalate (PBT) matrix. The radius of the processed glass fibers varies from 10 to 12 µm and their length is considered as constant with 250 µm. During the injection molding occur a misorientation of a central layer due to rheological effects. We found a dependency of the misoriented central layer in the sample w.r.t. inlet position. The thickness of this layer varies from 60 to 110 µm. The layer thickness is computed by averaging the differently oriented fiber component over the entire sample size. Also, the orientation distribution of the fibers in the misoriented central layer depends on its positioning towards the inlet. We simulate the fiber orientation in a plate and show results of comparable quality to those from X-ray scans. The co-authors used our orientation analysis for generating of a representative volume elements (RVEs) of a GFRP. Then, these results are analyzed w.r.t. damaging on a microscale and verified on larger scales (mm to cm) by simulated and real tensile testing experiments. In this interdisciplinary project, we validated a simulation technique for homogenization on the microscale and thus justified to shift cycling tensile tests from real to virtual.

Analysis of large GFRP components, Baranowski et al. 2019

Baranowski, T., **D. Dobrovolskij**, K. Dremel, A. Hölzing, G. Lohfink, K. Schladitz, and S. Zabler (2019). "Local fiber orientation from X-ray region-of-interest computed tomography of large fiber reinforced composite components". In: Composites Science and Technology 183, p. 107786.

Contribution

This peer reviewed article is a result of a project funded by the Fraunhofer Society. It involves work from representatives of a GFRP part production company, an automotive company, and two research institutions. On the project organization level, I worked on the attuning to requirements of all project partners in order to write this contribution. I analyzed the extensive amount of data, matched imaged data of varying resolution and different X-ray measurement set-ups. I wrote the analysis and results parts of the publication.

Publication Status and Availability

The original publication is first published in Journal "Composites Science and Technology". A preprint of identical content is available on arXiv (https://arxiv.org/pdf/2005.06431).

Description

We analyze data from a half meter long GFRP automotive bearing part. A novel X-ray scanning device allows for scanning of large GFRP parts. To the best of our knowledge and for the first time, we proved the accessibility of micrometer precision in the 3D imaged data without a destructive extraction of a sample before scanning. The GFRP part is scanned at varying resolutions by the same X-ray device, as well as by another X-ray device. All scans are performed without any extraction of samples, meaning non-destructive testing. We acquired and analyzed data of varying resolution of 45 down to 3 µm. I analyzed the acquired 3D images and compared them w.r.t. image resolution vs. quality of fiber orientation decrease. The analysis results show an evidence of the misoriented central layer, as previously stated in Andrä et al. 2019. I prove that consistent estimation of orientation distribution of the glass fiber component w.r.t. all acquired resolutions is possible. Moreover, we validate the simulation of injection molding by comparison of the estimated and the simulated orientation distributions.

Part I

Preliminaries

2 Modelling of Microstructure

In general, solid materials and their physical properties are determined by their inner structure. This inner structure is called microstructure. Vander Voort et al. 2004 define microstructure as a structure of a material's prepared surface, which can be imaged by an optical microscope above 25 times magnification. We assume that another imaging device can capture the same microstructure, except for an error caused by measurement inaccuracy and sample preparation. Then, this work is dedicated to the spatial microstructure characterization and the consequences for some of the material properties. I study image data of material microstructures and apply stochastic modelling in order to find a suitable and compact microstructure representation. The stochastic modelling approach addresses the randomness of a heterogeneous structure on the microscopic scale. As discussed by Jeulin 2021, there are two reasons justifying the stochastic modelling approach. First is the quantification of influence caused by random structure at small scale and the corresponding characteristics at the global scale. The second is the influence of local variation of imaged microstructure caused by limited sample size and number. Following this argumentation, Jeulin 2021 suggests the probabilistic approach for microstructure representation for heterogeneous media.

The stochastic modelling procedure requires a specific model choice which needs to be suitable for the considered material. Then, the chosen model is defined by one or more objects following parametric statistical distributions. A high number of involved model parameters implies a more complex model and accordingly a complex modelling procedure. The number of parameters yields from the specification of objects and the considered distributions. The modelling procedure comprises a model fitting. While model fitting, parameters need to be estimated from acquired material data. The model fit ensures optimal parameters for a stochastic representation of the microstructure of a specific material. Then, a random structure can

be realized. The realization can be depicted in a visual 3D image and thus become visually observable.

In the literature, there are attempts for acquisition of digital material data sets which serve as a virtual material representation, as demonstrated by Bhandari et al. 2007. In this digitalization method, the discrete acquired data of the microstructure becomes transformed into a finite element mesh. The fundamental difference of the two approaches lies in the presence or absence of limitations to one digital sample representation and the sample size. Comparing to the digitalization method, the stochastic modelling approach has the following advantages:

- The random structure is scalable in terms of physical object size and the number of observed objects.
- The discretized image resolution of the random structure can be changed.
- The parametrized model can be studied w.r.t. material properties allowing for virtual material design, as for instance Diebels and Rjasanow 2019 do successfully.

Usually, virtual material design has a context given by the material's application in a specific engineering field. In this context, questions might emerge from one or multiple of the following areas: acoustic, mechanical, thermal, electric, chemical, particle flow or multibody system's properties. Each of these fields sets up various requirements for the considered material's model and thus determines the required model characteristics. Materials arrange themselves in patterns which depend on the considered scale and the material itself. Multi-scale modelling is a research field which attempts to solve problems by involving considerations at different scale of time or space (Horstemeyer 2010). The upper scale requires the knowledge from the lower scale in order to be analyzed. According to Diebels and Rjasanow 2019, each of the smaller scales provides information to the upper scales. In this context, the stochastic model can provide information at lower scale in order to analyze properties of the material at higher scale. Moreover, the here proposed stochastic model can be customized at a smaller scale, leading to a change of materials properties at higher scale. Figure 1 indicates the dependence of the material's characteristics on the scale by the horizontally aligned arrows. Altogether, the stochastic modelling approach is advantageous in the context of virtual material design, as it increases its informative value and allows for virtual studies.

2.1 Data Acquisition

A physical property of a certain material is determined by the inner structure of the material. Thus, we need to analyze the inner structure w.r.t. the arising question about the physical property. This leads to analysis of image data of the microstructure in order to determine the characteristics of the topological structure, before model fitting. Even before the analysis of image data, we need to think about the data acquisition. The image data should reveal the topological structure. Simultaneously, the measurement error should be as small as possible for the data acquisition technique. Each acquisition technique operates differently and correspondingly introduces its own measurement error. Our knowledge about the acquisition technique and the microstructure of interest is always limited by our insight in evidence. This means, there is nothing more precise than a ground truth. We can verify the acquired image data by the ground truth, if the ground truth exists. Either, the ground truth exists due to previous measurements, e.g. as a result of another acquisition technique, or as a result of a simulation technique. If the ground truth is unavailable, then other reasonable data can serve as a less precise approximation. In general, the acquired data or measurement results need a validation by some other data, where at least a reasonable comparison of magnitude is possible.

Each physical scale of material demands measurement techniques which can cope with specifics of the particular physical scale. The utilized acquisition technique differs due to

- the acquisition equipment,
- feasibility limitations,
- preparation of sample,
- type of acquired data (e.g. dimensionality, data type).

The arising question about the microstructure of material determines mainly the data we want to acquire in order to yield some insight. In any case, once the data is acquired, it determines the steps ahead: the geometric characterization of the data and the model fit. The analysis depends significantly on the type of data. Typically, the observed data should reveal the general spatial pattern of random character. The idea usually is, to study the observed data and to derive a probabilistic model

serving as a parametrized representative of the observed structure. Before that, we introduce the general idea of a model fit and the corresponding mathematical terms, so that we can use them in the data analysis part and the model fit procedure. The acquired data is usually a 2D or a 3D image data on a regular grid consisting of marked points on this grid.

2.2 General Outline of Stochastic Microstructure Modelling

The characterization of random geometric objects requires an exact mathematical definition of the space and corresponding metrics. The Bertrand paradox (Bertrand 1889; Walz 2004) is an impressive historical proof for this statement. In stochastic microstructure modelling, the most central and essential concept is the random closed set, also called RACS in literature. There exists a stack of literature on the topic stochastic microstructure modelling. Separated by motivation, there is the theoretically oriented work by Daley and Vere-Jones 2003; Schneider and Weil 2008, and the application oriented ones by Chiu et al. 2013; Jeulin 2021; Ohser and Mücklich 2000; Ohser and Schladitz 2009; Torquato 2013.

The modelling procedure usually starts by studying observed data and choosing a suitable model. Jeulin 2021 points out what is mathematically needed for the conceptual building of random structures. In order to define random closed sets, we need to define an analogy to a classical a random variable whose values are sets. A classical variable is a measurable mapping from an abstract probability space $(\Omega, \mathcal{A}, P)$ into a measurable space (E, Σ), where Σ is a suitable σ-algebra. A natural choice for a σ-algebra is the Borel-σ-algebra $\mathcal{B}(E)$ generated by the open subsets of E. In our case, E is the space $\mathcal{F}$ of closed subsets of $\mathbb{R}^n$. We need to equip $\mathcal{F}$ with a σ-algebra and want to use the Borel-σ-algebra. To this end, we need open subsets of $\mathcal{F}$. Therefore, we introduce a topology on $\mathcal{F}$.

We follow for the precise definitions Schneider and Weil 2008 in particular chapter 2, where a **probability space** is a triple $(\Omega, \mathcal{A}, P)$ of a sample space (or a set) Ω, a σ-algebra $\mathcal{A}$, and a positive measure (the probability) P, with $P(\Omega) = 1$. A **σ-algebra** $\mathcal{A}$ is a family of sets $A \in \mathcal{A}$ satisfying the following axioms:

i) $\Omega \in \mathcal{A}$, $\varnothing \in \mathcal{A}$

ii) $\forall A \in \mathcal{A}$, $A^C \in \mathcal{A}$ with the complementary set $A^C = \Omega \setminus A$

iii) For any finite and denumerable set $A_i \in \mathcal{A}$: $\bigcup_{i=1,\ldots,n} A_i \in \mathcal{A}$ and therefore $\bigcap_{i=1,\ldots,n} A_i \in \mathcal{A}$.

A Borel-σ-algebra is a version of a σ-algebra, where the generating set consists of the open sets of a topological space. We now define a topology on $\mathcal{F}$ in order to use the Borel-σ-algebra $\mathcal{B}(\mathcal{F})$. Let $\mathcal{C}$, $\mathcal{F}$, and $\mathcal{G}$ be the systems of compact, closed, and open subsets of $\mathbb{R}^n$, each including the empty set $\emptyset$. For sets $A, A_1, \ldots, A_m \subset \mathbb{R}^n$ we define

$$\begin{aligned} \mathcal{F}^A &= \{F \in \mathcal{F} : F \cap A = \emptyset\}, \\ \mathcal{F}_A &= \{F \in \mathcal{F} : F \cap A \neq \emptyset\}, \\ \mathcal{F}^A_{A_1,\ldots,A_m} &= \mathcal{F}^A \cap \mathcal{F}_{A_1} \cap \ldots \cap \mathcal{F}_{A_m}, \qquad m = 0, 1, \ldots, \end{aligned}$$

where $\mathcal{F}^A_{A_1,\ldots,A_m} = \mathcal{F}^A$ for $m = 0$. The desired topology on the space $\mathcal{F}$ is the one generated by the system

$$\{\mathcal{F}^C : C \in \mathcal{C}\} \cup \{\mathcal{F}_G : G \in \mathcal{G}\}.$$

This definition corresponds to Schneider and Weil 2008, i.e. Definition 2.1.1 (topology of closed convergence).

Any of the systems, either $\{\mathcal{F}^C : C \in \mathcal{C}\}$ or $\{\mathcal{F}_G : G \in \mathcal{G}\}$, generates the Borel-$\sigma$-algebra $\mathcal{B}(\mathcal{F})$ (Schneider and Weil 2008, Lemma 2.1.1).

Finally, a **random closed set** is a measurable mapping $Z : (\Omega, \mathcal{A}, P) \to (\mathcal{F}, \mathcal{B}(\mathcal{F}))$. In the following, we will need special cases of random closed sets.

We need one further definition for the characterization of random closed sets. Let $\mathcal{C}$ be is the system of compact subsets of $\mathbb{R}^n$. The **Choquet capacity** $T_Z : \mathcal{C} \to \mathbb{R}$ of the random closed set Z on $(\Omega, \mathcal{A}, P)$ is defined as

$$T_Z(C) = P\{C \cap Z \neq \varnothing\},$$

for all compact subsets of $C \in \mathcal{C}$, whereat $T_Z \in [0, 1]$ and $T_Z(\varnothing) = 0$. Assuming the monotone convergence of C_i to C for $i \in \mathbb{N}$ and $C_i \in \mathcal{C}$, implying $C_{i+1} \subset C_i$

and $\bigcap_{i\in\mathbb{N}} C_i = C$. Then, the Choquet capacity converges $T(C_i) \to T(C)$. Hence, the Choquet capacity determines the distribution of a random closed set. Jeulin 2021 defines a model of a random structure by its Choquet capacity. The Choquet capacity ensures the statistical evaluation of the compact sets by moments of the probability function (Jeulin 2021; Ohser and Schladitz 2009).

A **point process** (PP) could be defined as a locally finite random closed set. In order to allow for multiple or marked points, PP are usually defined as random counting measures. Let $\mathfrak{N}$ be the set of all counting measures on $\mathbb{R}^n$ and $\mathcal{N}$ the corresponding Borel-σ-algebra (for details see Schneider and Weil 2008, chapter 3), then a PP on $\mathbb{R}^n$ is defined as a measurable mapping from the probability space $(\Omega, \mathcal{A}, P)$ to $(\mathfrak{N}, \mathcal{N})$.

Let $\mathcal{C}' = \mathcal{C} \setminus \{\varnothing\}$ be is the system of nonempty compact subsets of $\mathbb{R}^n$. We consider a marked PP $\tilde{X}$ with the mark space $\mathcal{C}'$. Then,

$$X := \sum_{(x,C)\in\tilde{X}} \delta_{x+C}$$

defines a **germ-grain process**, if the local finiteness of the counting measures on the right side is guaranteed.

To complete the definitions of basic concepts used in the following, we finally define a **mosaic** M in $\mathbb{R}^n$ as a countable system of subsets, that satisfy the following conditions:

i) M is a locally finite system of nonempty topological sets;

ii) the sets $K \in M$ are compact, convex and have interior points;

iii) the sets of M cover the space

$$\bigcup_{K\in M} K = \mathbb{R}^n$$

iv) If $K, K' \in M$and $K \neq K'$, then $\operatorname{int} K \cup \operatorname{int} K' = \varnothing$.

2.2.1 Microstructure Models

Stochastic PP are fundamental in stochastic geometry, as they are a basic ingredient to many spatial models. Stochastic PPes have been applied to many areas such as astronomy for planet and star distributions, plants in fields, cells in biological tissues or material cracks, as pointed out by Jeulin 2021. A stochastic PP is a sequence of random variables that are indexed by a well-defined set.

A **Poisson PP** is the simplest PP and is briefly a point process that defines a perfect disorder. More precisely, a Poisson PP defines a random variable $N(K)$ for a Borel set K with the intensity $\theta(K)$. This parameter describes the number of independent points of the process in the compact set K. Then, the Poisson distribution is:

$$P\{N(K) = n\} = \frac{\theta(K)^n}{n!} \exp(-\theta(K)).$$

A constant intensity w.r.t. translation along space means a proportionality w.r.t. the Lebesgue measure. This means simultaneously the stationarity of the process. A Poisson PP is homogeneous as the Lebesgue measure is invariant to rotations of the compact set K.

A **Laguerre tessellation** of $\mathbb{R}^n$ is an extension of a marked PP, as by definition to each random point x_k is attached a random radius R_k. Let $\mathcal{P}$ be a Poisson PP in $\mathbb{R}^n$ with intensity θ. Then, a Laguerre tessellation is a union of cells defined by

$$C(x_k, R_k) = \{x \in \mathbb{R}^n | d(x, x_k) - R_k < d(x, x_l) - R_l, x_k \in \mathcal{P}, x_l \in \mathcal{P}, x_k \neq x_l\},$$

where d denotes the Euclidean distance. The inequality defines which x belong to cell C. This process generates a random set with non-overlapping cells based on a PP, where the "perfect disorder" is not present anymore.

In order to generate a realization of a Laguerre tessellation, we apply the **force biased** (FB) collective rearrangement algorithm (Ohser and Schladitz 2009). The FB algorithm realizes a hard-core process, where a packing of non overlapping spheres is computed. This algorithm starts with a Poisson PP, where each point serves as a generator. The algorithm attaches to each generator point a radius and rearranges the resulting spheres in an observation unit window until the spheres do not overlap, and the sphere packing satisfies the preset volume fraction.

The sphere packing serves as a set of cell generators. Then, the cells emerge by bisectioning the distances between each pair of neighboring generators.

Also, the **Random Sequential Addition** (called RSA by Torquato 2013, SSI by Chiu et al. 2013) is a process which allows for generation of a random set of non-overlapping objects, which is also called a hard-core process. The RSA is defined by the following sequence:

1. Define a random closed set by
   a) its shape and size distributions
   b) and its uniformly distributed random position in the observation window.
2. Check for object intersection with already placed objects and accept if no intersections occur, and go back to step 1a. Otherwise, the object placement is rejected, and the number of rejections incremented.
3. If the number of rejections is lower than a preset number of rejections in a row, or the desired volume fraction is not reached, then go back to step 1a. Otherwise, the random sequential addition finishes the computation.

This sequence generates a macroscopically homogeneous random packing of topological objects.

2.2.2 Geometric Characteristics

A realization of a model becomes comparable to existing image data by a generation of an image of the realization. The compact sets represent objects of certain shape and size. Quantitative measures give these objects a numerical meaning. Thus, by measuring the objects observed in acquired image data, we can numerically compare these to the corresponding characteristics of the chosen stochastic model, yielding a quantitative measure for the quality of the chosen models. The corresponding measures are the so-called Minkowski functionals and are summarized in Table 1. Minkowski functionals suffice the experimentally required constraints: the invariance by translation, continuity and additivity of a random closed set.

In some cases it is necessary to quantify a structure, which consists of non-separable objects, e.g. a porous medium or a mineralogical texture. The Crofton relation

space	measure	description w.r.t. a compact set A
$\mathbb{R}$	$\ell(A)$	length
$\mathbb{R}^2$	$A(A)$	area
	$L(A)$	circumference
	$N(A)$	connectivity
$\mathbb{R}^3$	$V(A)$	volume
	$S(A)$	surface area
	$M(A)$	integral of mean curvature
	$N(A)$	integral of total curvature or connectivity number

Table 1: Minkowski functionals for isolated objects (Jeulin 2021).

(Ohser and Schladitz 2009) determine the specific measurements, which are summarized in Table 2. The specific measurements are evaluated in the context of stationary processes and keep the properties of Minkowski functionals. The specific measurements have the subscript L for length, A for area, and V for volume, w.r.t. the considered space and the entire random process. More precisely, the quantities are normalized by the corresponding measure corresponding to the dimensionality of the stationary random set. These measures are also called as intrinsic volumes, e.g. by Ohser and Schladitz 2009.

space	measure	description
$\mathbb{R}$	L_L	specific length
	N_L	specific number of connected components
$\mathbb{R}^2$	A_A	area fraction
	L_A	specific boundary length
	N_A	density of the Euler number
$\mathbb{R}^3$	V_V	volume fraction
	S_V	specific surface area
	M_V	density of the integral of mean curvature
	χ_V	density of the Euler number

Table 2: Specific measures for a stationary random set or its parts, as discussed by Jeulin 2021.

The considered measures depend on various aspects of the fitting procedure: the model and the considered objects, as well as the image data of the microstructure and its analysis. Hadwiger 1959 proves the existence of $n + 1$ linear independent specific measures in n dimensions. Consequently, a sequence of measures needs to be evaluated in order to evaluate a microstructure numerically.

Once an average object is topologically well described and a distribution of the variation of the objects is known, we can have a recourse to a random PP and a generation of well-defined objects. We start by a random PP leading to a parametric distribution. A sequence of random variables yields correspondingly a sequence of distribution functions with a variety of parameters. This sequence belongs then to the same stochastic PP. All parameters determine the parametric space. Consequently, the parameter variation entails a change of the model appearance, which can be measured by the Minkowski functionals or specific measures. Practically, the model and parameter choice depend on the morphological analysis of the structure to be modelled. The parameter space is determined by the number of parameters. Mathematically, a material model is found if a distance between a representative of real material and its model is minimal. Minimization is an iterative process, the complexity of which depends on the number of parameters which need to be fit.

The observation window is usually in stochastic geometry uniformly sized, and the observed microstructure gets its physical meaning after scaling up this observation window. A representative volume element (RVE) is the smallest volume of the material which can represent the material's characteristics over its entire volume, as discussed by Jeulin 2021. This means, the RVE is large enough to capture small local deviations in material's characteristics and simultaneously non-sensitive to those variations due to averaging out over the accounted volume.

2.2.3 Estimation of the Characteristics Based on Image Data

In context of stochastic microstructure modelling, there are mainly two types of data. First, the measured data coming from the acquisition technique and having a data structure specific to the acquisition device. More precisely, the size of the 2D- or 3D-images is determined by the physical dimensions of the built-in components, leading to a specific size and resolution of the image. The resolution is the physical scale equivalent to one pixel or voxel. Thus, the resolution is a decisive parameter which ensures a well depicted microstructure. Usually, a small resolution number leads to well depicted objects, as a high number of grid points allow for a better visibility of an object. Also, the field of view is limited by the sensor or detector size, which is a built-in component of the device. Field of view mainly determines,

the size of area or volume which can be imaged. Altogether, a high resolution and a large field of view allow for an image of well depicted objects in a large neighborhood, allowing for a large observation window of the structure to be studied. The coloring scheme of the images is predetermined by the technical abilities of a particular device as well. The range of depicted color values impacts the perceived quality of image data. In our context, the color range usually corresponds to $2^8 = 256$ or $2^{16} = 65\,536$ color values. A region of interest defines a particular depicted region of a sample, if the sample is not scanned entirely.

Second, the image data is generated after the realization of a model with a specific parameter choice. In this case, the virtual resolution can be chosen as needed but is limited due to the raising data amount which needs to be processed consequently. The color range can also be chosen as variable as needed. The number of realized objects, which are depicted is called region of interest (see Ohser and Schladitz 2009) and is related to the physical field of view. All in all, the choice on the resolution, the color range and the number of observed objects depends on the physically acquired data since it needs to be comparable.

We use the software packages MAVI (Fraunhofer ITWM, BV 2021) and ToolIP for all image processing routines. The difference between these two tools is due to their abilities to process the data differently. MAVI enables an application of algorithms to single images and provides a 3D visualization of results. However, ToolIP allows for an application of a sequence of algorithms with preset parameters for a stack of data sets where no user interaction is indispensable. Also, we use R for all other analysis steps.

3 Applications

3.1 Analysis and Modelling of Microstructure

In both applications, the polycrystalline microstructure and the GFRP, I aim at finding a geometric model consisting of random compact sets following parametric random distributions. Jeulin 2021 indicates these models as those which require prior general properties, as the invariancy w.r.t. distribution. The considered models, the polycrystalline microstructure as well as the GFRP, require a PP. But, the points of a Poisson PP are statistically independent by definition, meaning no spatial interaction between points. This fact enforces an introduction of a repulsion, which on the one hand distorts the PP with its analytical properties, but introduces features which are useful in the context of real materials.

3.1.1 Polycrystalline Metals

In the first application, we analyze two different data sets of two polycrystals. We rely on the microstructure data provided by independent third parties. We received two types of data, which show the microstructure of two alloys, i.e. Inconel-617 and titanium. These two imaging techniques share the physical scale of the depicted microstructure, which is nanometer to micrometer, as also indicated in Figure 1. Each acquisition technique has specific limitations due to experimental issues, which enforces a sample size limitation and/or limitations w.r.t. material of the sample. In our case, the coarse grained Inconel-617 is captured by a light microscope and the fine grained titanium by a X-ray diffraction contrast tomography (DCT). In general, the choice of imaging technique depends on the microstructure scale and material characteristics, e.g. the microstructure of Inconel-617 is impossible to capture by DCT, probably due to its coarse grains consisting of subgrains.

A polycrystalline microstructure is homogeneous and isotropic if the metallic material has not been welded or similarly treated, see work by Tromans 2011 for examples. A polycrystal has its typical granular microstructure, which can be modelled by a 3D tessellation. A Laguerre tessellation suits this purpose, as it generates cells of distinct size due to the attached radii, see publications by Fan et al. 2004 and Redenbach 2009. Typically, a log-normal distribution suits the polycrystalline grain volumes, as well as the corresponding sphere packing, which is needed for the generation of the Laguerre tessellation. After all, the parametrized Laguerre tessellation yields a realization consisting of non-overlapping convex polyhedra. These parameters are either expected number of cells in the observation window, or the mean volume of a cell, and its variance.

We employ stochastic models following suggestions from literature. More precisely, Torquato 2013 and Chiu et al. 2013 portray tessellations as a suitable model for polycrystals, i.e. Voronoi and Delaunay tessellations. The Laguerre tessellation is a weighted version of the Voronoi tessellation. The cell generators are the same for both tessellations. But, the sectioning rule between two neighboring cells is governed by a weight which is attached to the generator. We build up on this knowledge and accordingly utilize the control mechanism of the cell volume during the generation of a Laguerre tessellation. Fan et al. 2004 investigate several polycrystals w.r.t. to numerical measures, which are typical for this closely packed granular media. More precisely, they study the average number of faces, edges, and the volume per cell, as well as the coefficient of variation (CV). The CV is the ratio of variance to average of cell volume. We use this coefficient while generating the packing of non-overlapping spheres, which serves as controlling mechanism for the desired distribution of cell volume. The force biased collective rearrangement algorithm ensures this condition. Although, the for this purpose required packing of spheres is computationally expensive, it is necessary since cell volume is of prime importance in the context of ultrasound applications. More precisely, it is the grain diameter which impacts the propagating ultrasound wave and causes its energy loss for high wave frequencies.

Coarse Grained Inconel-617

First, the data from a light microscope reveals the microstructure of Inconel-617 by the depicted grain size distribution in 2D sections, i.e. the Feret diameter of the

observed grains. More precisely, quantitative analysis of the acquired data yields discrete distribution of the aforementioned diameter. For the acquisition of this type of data, a laboratory equipment requires a light microscope and the necessary tools for cutting the metal and surface preparation. The surface preparation includes etching and polishing, which leads to a visibility of grain boundaries.

In case of Inconel's polycrystalline microstructure, we build on the available data and accordingly study the corresponding grain diameter in 2D sections. The actual micrograph images are studied in a previous study by Walte et al. 2015. This data provides a discrete distribution of Feret diameters in 2D sections of the observed microstructure. More precisely, a Feret diameter is the maximum linear distance fitting into a grain's planar section. The discrete distribution appears to be log-normal, which aligns with previous studies of polycrystals, see the work of Fan et al. 2004. The log-normal distribution is a two-parametric distribution. These two parameters are equal to the mean value and a standard deviation of the natural logarithm of the random variable. We summarize this model fitting approach in three main stages:

1. choosing the initial number of cells in a region of interest,
2. adapting the number of spheres to be packed until the Feret diameter in 2D sections fits for a fixed coefficient of variation,
3. choosing in a naive grid search the mean cell volume and its standard deviation and computing the realization of Laguerre tessellations until these two parameter correspond to the observed in micrographs.

By this approach, we can find a suitable coefficient of variation for the 3D Laguerre tessellation, which fits the observation in micrographs. This approach is time-consuming and requires numerous manual data analysis steps.

Fine Grained Titanium

Second, the X-ray DCT data shows the granular structure of titanium providing the entire three-dimensional size distribution of the grains, including the orientation of each single grain. For this sophisticated acquisition technique, a synchrotron radiation facility is needed. Also, the sample preparation is demanding. Moreover, this imaging technique is suitable for a limited number of polycrystals, only, i.e.

polycrystals with a low subgrain misorientation, a low density and subatomic number (see Ludwig et al. 2009 for more details). The acquired DCT data is available as a three-dimensional image, where an image is a regular grid of pixels or voxels. To each of the discrete points is assigned a color value. In this DCT image, each voxel belongs to exactly one set of pixels, which are called labels. Each scanned grain is assigned exactly to one label during the reconstruction procedure. The number of depicted labels corresponds to the number of grains, plus one label for the background. Correspondingly, the 3D image is a label image, where the depicted sample consists of enumerated grains.

The microstructure of the entire titanium sample is available in a 3D data set, allowing for a relatively accessible modelling procedure. This simple data structure allows for counting the pixels per label and multiply by the physical resolution, leading to the volume per grain. This grain volume yields a discrete distribution of log-normal shape. The standard deviation of the grains' volume and the mean value yield immediately the desired coefficient of variation for the Laguerre tessellation. In the last step, the suitable number of cells per region of interest and the coefficient of variation can be used to generate a model's realization, which is large enough for the simulation purpose.

3.1.2 Glass Fiber Reinforced Polymers

In the second application, we acquire and analyze image data from three different X-ray devices. All three devices are laboratory set-ups with different specifications. Andrä et al. 2019 utilize X-ray device which is a well known equipment with a large experimental experience in the past. The X-ray device for large components, as presented by Baranowski et al. 2019 is a completely novel set-up at the point of publication. The acquired data is validated by image data of the same large component acquired by a third X-ray device. Two of the three devices require a sample extraction, which is state of the art, at least in the research environment. In this case, a small sample of approximately some millimeters along each of the three dimensions needs to be cut out from the component. Then, the sample can be placed on the sample holder of an X-ray device and be scanned. After a sequence of rotations of this sample, single scanning projections are collected and can be reconstructed, leading to a 3D image of the sample. An X-ray device has its own

internal coordinate system, which is composed of the source, the sample stage, and the detector local coordinate systems. Based on this composition, single projections are collected and can be reconstructed. The sample itself has no own coordinate system which would allow for identification of precise sample orientation. Hence, the coordinate system of the reconstructed 3D image depends on how the sample was mounted on the sample holder prior to scanning. All three devices produce a slightly different X-ray intensity, and depict slightly different scanned values due to different technical components built into the X-ray set-up. The imaging technique of all X-ray devices is tainted by the partial volume effect, which has been studied by Hoffman et al. 1979. Shortly, the size of small objects is underestimated due to change of X-ray absorption inside and outside the object. This effect can be reduced by increasing resolution, but not eliminated. The acquired image data has the dimensionality and data type in common, where all 3D images are gray value images, even if their histograms vary slightly. This is due to the technical components but also due to the imaged material, which absorbs differently depending on the chemical and/or geometrical composition of the material to be scanned.

The microstructure of a GFRP is anisotropic in general, and heterogeneous macroscopically, as discussed by Diebels and Rjasanow 2019. GFRP consists of glass fibers and a polymer matrix, where the geometric arrangement of both components are variable and depend on the material purpose. 3D image data of the GFRP samples are analyzed by Andrä et al. 2019 and Baranowski et al. 2019. The 3D image data is acquired in different laboratories, but has in common the data type. All 3D images are gray value images with a range of 2^{16} gray values. Wirjadi et al. 2016 gives an overview of possible tools for orientation analysis in gray value images. Given a mask for the glass fiber component, the gray values are averaged over a neighborhood inside the mask leading to a local orientation. The orientation distribution leads to an estimation of the orientation tensor. The orientation tensor is a quantity and is usually required in context of engineering applications. The quality of the estimation depends on the resolution of the image, as a fiber should be depicted by at least 5 voxels per its diameter, see the work by Pinter et al. 2016.

Otherwise, the orientation determination becomes distorted due to a poor or non-precise mask. The data sets of the GFRP samples differ in their histograms, partially due to the differences in samples themselves, the resolution, the size of images, and the alignment of the coordinate system. In the publication Andrä et al. 2019, we

study five samples having each a volume of 2^3 mm^3, which are depicted by $1\,024^3$ voxels respectively. The samples are extracted from one plate of a constant thickness, and are scanned by the same device with a resolution of $1.2-1.3$µm. Thus, we treat the data sets equivalently, so that the processing steps affect the results in the same way. The processing steps are:

1. Denoising the image data by a $5 \times 5 \times 5$ median filter.

2. We calculate the mask by a computation of Frangi's index, which calculates a local eigenvalue decomposition of the Hessian matrix, see Frangi et al. 1998. The idea is to detect the fibrous structure by the eigenvalue with the smallest magnitude. This approach allows for a better segmentation of the pixels belonging to the fiber core.

3. Based on the gray value images, we estimate the thickness of misoriented central layer by gray value projections along the mold flow direction.

4. Using the thickness of misoriented layer, we separate the image data in layers.

5. Then, we determine the mean fiber direction in layers and their corresponding orientation tensors.

In Baranowski et al. 2019, we analyze a large amount of data from one sample component. This half meter large sample component has a complex 3D shape. 3D images from four regions of interest are acquired at different laboratories by two X-ray devices. The main difference w.r.t. previous publication is the fact, that no destructive sample extraction has been undertaken and samples with various geometrical complexity have been scanned. We acquire overall eight data sets, where five of them are referencing to one region of interest but resolve parts of this region at varying resolution, which reaches from 3 to 44 µm. At the highest resolution, the physically largest region of interest we scanned leads to a data set of $1\,944 \times 8\,832 \times 1\,944$ voxel at a 16-bit color depth. This leads to a data size of approx. 67 GB, which is in the best case cumbersome to handle even during the simplest image loading procedure. We compute the local fiber orientation and the orientation tensor w.r.t. the resolution change. We omit the computation of a designated fiber mask in case of the coarse resolution, since the fiber component cannot be reasonably separated from the polymer matrix. We compare the derived orientation results w.r.t. resolution change. The determined local orientation looses its significance and washes out

as the resolution drops. This comparison is founded on a manually carried out registration of corresponding regions of interest. An automatic comparison, in terms of image registration (Brown 1992), is in this case not possible yet, due to a missing alignment in coordinate systems of the data sets and the large amount of data.

While modelling the microstructure of GFRP, we rely on the prior modelling knowledge about GFRP. The GFRP are mainly characterized by the definition of single objects and their distribution in the observation window. This is possible due to the fact of entirely artificial production of the GFRP material. Thus, the topology of a cylinder of an expected radius and an expected length is assumed to suite the shape of short glass fibers. If a straight cylinder of a known radius and length is placed in an observation window, then its position is well-defined by its, radius, length, and an orientation. Then, the orientation distribution, the length distribution and a radius distribution, yields a stochastic model for the GFRP material, which can be realized by the previously described RSA algorithm.

Thus, we utilize the cylinder model in context of new data in order to answer new questions. Similar to the sphere packing in Laguerre tessellations, we also use here a hard core PP. The used RSA places cylinders of a constant radius and length in an observation window and checks for possible overlaps with the already existing cylinders. If there is no overlap, then the process keeps adding cylinders, and otherwise the process removes the overlapping cylinder and attempts again. The process finishes after reaching a preset volume density of placed cylinders, or no further cylinders can be added. In the best case, the RSA achieves a realization of a cylinder packing w.r.t. the volume ratio and spatial orientation distribution of the fiber component. Andrä et al. 2019 successfully demonstrate the application of RSA in order to model GFRP, where the co-authors generate a layered microstructure model by application of the RSA.

3.2 Simulation of Material Properties

In context of simulation, the computation time and precision of the algorithms shifted in past years from weeks to hours. Thus, the simulation techniques are becoming common in various disciplines. We introduce this section as one of the last due to the procedure follow up, since the simulation part requires a material

model. But, the simulation of a specific physical behavior of a material is closer to the original question about the material itself and thus indispensable. A simulation can sufficiently build up on the microstructure model, if the microstructure model provides the necessary detailedness. In the following, we give a short overview of simulation techniques, as we utilized them to gain insights about metallic polycrystals and GFRP materials.

3.2.1 Ultrasonic Scattering in Polycrystals

The metal changes its inner structure while a change of the state of matter. The most natural crystalline materials arrange themselves in a collection of grains, which are separated by grain boundaries. Nuclei are distributed in the liquid metal and initiate solidification at certain physical conditions, as discussed by Desch 1912. During this solidification period, each of the grains grows in random crystallographic orientation until neighboring grains meet and form a grain boundary. After the solidification state, whenever a wave propagates in this polycrystal, the energy of the propagating wave becomes scattered at the grain boundaries due to the shift of crystal orientation in neighboring grains, as pointed out by Hirsekorn 2014.

Many technical components are products of metallic polycrystals and hold security relevant tasks in mechanical constructions. Non-destructive testing techniques ensure a defect-free, and long-lasting lifetime of these components. Ultrasonic testing is one of the possible non-destructive testing techniques. It is advantageous due to its relatively high penetration depth and its ability to serve as a mobile device. Since an ultrasonic wave is a pressure wave, it interferes with the microstructure of the polycrystal. Hirsekorn 2014 points out, that the scattering of ultrasound wave is caused by energy flux at grain boundaries. Scattering of the propagating wave is one of the contributions to the general attenuation, or total loss. Besides scattering, absorption, diffraction, geometrical and coupling losses contribute to the total loss of energy, as Truell et al. 1969 discusses. That means, that scattering is experimentally not measurable as separate from the other contributions. However, the propagating wave becomes attenuated w.r.t. to the penetration depth and is usually captured in an attenuation value. The attenuation value is a material dependent constant and is experimentally acquired.

In publication (Dobrovolskij and Schladitz 2022), we investigate the backscattering in metallic polycrystals. Hirsekorn 2014 follows the idea of unified scattering theory (Stanke and Kino 1984) and solves the elastodynamic equation of motion for closely packed scatterers. The assumption of small deviations due to microstructural variations leads to a formulation of scattering coefficients. Hirsekorn 2014 formulates the scattering coefficient as a function of scattering direction, w.r.t. incoming and scattered wave. We interpret the scattering coefficient as a spatial function and deploy this spatial scattering function in context of simulation of backscattered wave contributions.

We assume one of the simplest scenarios of ultrasonic testing, a puls-echo technique. In puls-echo technique, the transducer operates simultaneously as a generator and receiver of longitudinal (or pressure) waves at a mid-band frequency. The emitted wave becomes scattered by closely packed scatterers, which are in our microstructure model the cells of the Laguerre tessellation, and grains in polycrystalline microstructure of a metal. The transducer is simulated by a sequence of discrete source points which emit the propagating wave. Then, we compute the usual and the scattered displacement field at the center point of each cell caused by the propagating wave of a specific frequency inside the frequency bandwidth. We use the reciprocity relation as introduced by Auld 1979 for computation of the resulting displacement on the receiver, which is derived by accounting for the scattered and the non-scattered displacement fields. We superpose then the contributions over all cells of the Laguerre tessellation and the entire bandwidth. Finally, we transform the computed result into time domain by an application of a Fourier transform.

3.2.2 Simulation Techniques for GFRP

The approach as described shortly in Section 2.2.3, and in detail by Andrä et al. 2019, leads to a microstructure volume of 2^3 mm^3 with a 20% fiber content. The glass fibers are embedded in a PBT, which is modelled by an elastoplastic material. This model allows for an expansion of micro-cracks and cavities. Thus, the elastoplastic material model is able to handle a composition of plastic and elastic energy, and a regularization damage component. This material model accounts for damage accumulation in the polymer component. Real PBT samples are undertaken in cycling loading tests, where the deformation and mechanical load is measured.

The measurements show a good agreement with the simulated tensile test under consideration of the elastoplastic material model.

Then, a RVE is defined by these two components: the PBT matrix and the glass fiber component. An image of the RVE is resolved by 1024^3 voxels, where a fiber diameter is resolved by 5 voxels. The deformation field is computed on the microscopic level by a finite element approach. Thus, a homogenization step allows for accounting of appropriate microstructure characterization on the macroscopic level. Then on macroscopic level, real and virtual tensile tests are conducted and result in a good agreement. This means that virtual cyclic tensile tests can replace real ones in the future.

As already portrayed in Section 2.2.3, we estimate the local fiber orientation based on the local gray values in the reconstructed three-dimensional CT-image. Besides of modelling the microstructure, we used the gray value 3D images of GFRP material for validation of a simulation technique of an injection molding process. Injection molding is a complex process, since it usually depends on many parameters: geometry of the component to be molded, the aspect ratio of fiber length l to fiber radius d, the percentage of fiber content Φ and the technical abilities of the production device. The component shape introduces an uncertainty in the distribution of fiber orientation as the suspension flow changes due to junction. The suspension is classified as dilute, semi-dilute or concentrated by the factor $\Phi l/d$. In general, a larger aspect ratio l/d introduces a higher chance of fibers being bent while the injection molding procedure. A higher volume fraction of fibers rises the chance of interaction between fibers. The technical abilities could be the number and placement of inlets of the suspension. Altogether, the injection molding is a complex procedure and its understanding and prediction reduces costs in production, as published by Lu et al. 2006. Our work (Baranowski et al. 2019) shows tangible reassurance of the injection molding simulation carried out by the commercial software Moldflow. More precisely, we compare the simulation results to the computed orientation tensor values from the gray value CT images in a 0.6 cm $\times$ 2.3 cm region.

4 Wrap-up

4.1 Summary

In general, stochastic geometry allows for geometric microstructure modelling based on observations. Prior to modelling, one should know Man sollte wissen was das Mikrostrurmodell leisten muss, um das physikalische Phänomen zu erklären. It is advantageous to have a suitable idea in mind, which suits the purpose of investigation, prior to starting the modelling process. Usually, a virtual investigation begins with the need to understand or explain some phenomena about a particular material. At this stage, any kind of conjecture about the phenomena to be explained and the microstructure of the material is helpful, as it leads to decisive choices of experiments, in particular acquisition techniques and the data. Once the data is acquired, its analysis should reveal a spatial pattern of random character. Then, an appropriate model choice is to be made. A broad variety of literature serves for this purpose: Chiu et al. 2013; Jeulin 2021; Ohser and Mücklich 2000; Ohser and Schladitz 2009; Torquato 2013. The detailedness and accuracy of a stochastic model needs to be as high to be sufficiently high to link to materials' properties and thus enable us to answer the arising questions. Then these steps contribute to a multi-scale modelling and help to understand complex material behavior. In the following, we summarize our results in the context of metallic polycrystals and GFRP materials.

We initiate our investigation with a need for explanation for backscattering of ultrasonic waves in a polycrystalline microstructure. The grain diameter is the most decisive parameter in the context of ultrasonic scattering. Hence, we use the corresponding parameter, the cell volume, for the model fitting procedure. For the model fitting, we use the log-normal distribution, which has two parameters, as a distribution of cell volume. We carry the model fit out for two polycrystals. First, we

analyze the microstructure of coarse polycrystal Inconel-617 based on 2D sectioning image data, which is acquired by a light microscope. For this model fit, we compute a sequence of model realizations, section them and thus compare the 2D grain diameter distribution stepwise until reaching the desired model parametrization. Second, we study the 3D DCT data of fine polycrystalline microstructure of titanium. This data allows for a relatively accessible model fitting procedure, where we compute model realization and compare the 3D volume of the cells to the grains' volume. These two microstructures are important in the context of ultrasonic backscattering investigation, as they feature different grain size, on average. Coarse microstructure is known to be difficult in the context of non-destructive ultrasonic testing, as the propagating wave becomes stronger attenuated by coarse microstructure. This phenomenon is also called microstructural noise. I implemented a novel simulation technique in order to compute the backscattered ultrasonic response based on the microstructure, which is represented by a realization of a Laguerre tessellation. In this simulation, each cell represents a scatterer of a volume equivalent diameter and contributes w.r.t. the frequency, its relative position to the receiver and its diameter. These results are the subject of the work by Dobrovolskij and Schladitz 2022.

We study GFRP components on a microscopic level in order to explain the macroscopic loading and failure conditions of the microscopically heterogeneous material. A large amount of 3D image data is acquired by X-ray devices. On the one hand, a plate with a constant plate thickness is scanned by a laboratory X-ray device. An image analysis part allows for a determination of layers and the corresponding orientation tensors. Based on this knowledge, we fit a stochastic microstructure model, which serves in two ways in this study. Firstly, based on this microstructure model, microscopic failure mechanisms are simulated and are found to correspond well to real measurements. Secondly, cyclic tensile tests are conducted virtually and compared to real measurements. The bearing capacities consist and consequently the real tensile testing routing can be avoided in the future. Diebels and Rjasanow 2019 dedicate a book to the understanding of GFRP materials, their behavior during mechanical loading and the processes during failure. In this book, we contribute a chapter (Andrä et al. 2019) where we publish our results. On the other hand, a large and complexly shaped bearing component from automotive application has been scanned by a novel laboratory X-ray device. Different regions of interest of this component have been scanned at different resolutions. We can confirm the usability of the non-destructive scanning for complex and large components. Then, we an-

alyze the excessive amount of 3D gray value images and determine the orientation tensors. Also, we show the accessibility for determination of local glass fiber distribution. However, the locally determined orientation tends to lose its significance w.r.t. the decreasing resolution, as the local orientation becomes washed out due to the averaging over a larger neighborhood. Also, we use the locally determined orientation tensor information for validation of injection molding procedure. The results agree well despite the fact of the complex region of interest, where fibers and the embedding matrix are bent. We publish these results in the work done by Baranowski et al. 2019.

4.2 Conclusion

To conclude, we adhere as closely as possible to the strategy of the minimum of detailedness and effort to answer a question or to come closer to the answer of that question. In context of both applications, we can hold on the made progress. I demonstrate success in the analysis of 2D or 3D data materials' microstructures, the subsequent modelling of 3D geometrical microstructure, and simulation of mechanical properties of material based on the microstructure models. The analysis of 2D or 3D data is essential and reasonable, as it leads to the model fit of microstructure by means of stochastic geometry. The stochastic geometry ensures finding a quantifiable and thus suitable model representation of the material's microstructure. After a model fitting, simulation methods can be applied. I execute this approach for two entirely different materials: fine and coarse grained polycrystalline metals and a composite material, a GFRP.

The proposed approach leads to the following insights regarding the polycrystals:

- The coarse grained Inconel-617, and fine grained titanium feature a log-normal grain distribution, which corresponds to previous research by Fan et al. 2004.
- The studied polycrystals can be successfully modelled by a Laguerre tessellations following a well-defined parametric log-normal distribution of cell volumes.

- The model can be fit, taking as a reference either a distribution of 2D diameters or a 3D grain volume distribution. A distribution of 2D diameters increases the computation effort and the amount of required data analysis.
- I implement a novel numeric simulation technique for computation of backscattered time-domain signals based on the previously fitted Laguerre tessellations.
- I analyze the computed domain-signals in order to estimate the variation of backscattered signal w.r.t. generated Laguerre tessellations in a first attempt of quantification.

The proposed approach suits well the idea of multi-scale modelling, as the generated microstructure model shows a similar behavior to the microstructural noise for specific frequency regions at the macroscopic scale, where the variation of signal amplitude increases. This behavior is still not verified by real experiments.

In context of GFRP, we gain the following insights:

- A GFRP off-shelf-part can be truly non-destructive scanned by a new X-ray device.
- The micro computed tomography allows for acquisition of regions of interest at resolutions from 45 to 3 µm.
- Analyzing the glass fiber component, we show a consistency of the orientation distribution in data acquired at all resolutions, as well as in data from two different X-ray devices.
- We confirm a presence of misoriented central layer in all analyzed samples. Moreover, we can quantify the change of orientation of the fiber component w.r.t. the inlet position in a simple plate sample.
- We employ the orientation distribution of the fiber component and generate geometric models consisting of non-overlapping straight cylinders.
- The generated model serves as an input in a finite element method for simulation of the microscopic deformation field.

- Then, a homogenization step allows for a generation of a virtual sample for cyclic tensile testing. The cyclic tensile tests correspond well to the results from real tensile tests. Thus, the simulation of mechanical load bearing capacity can replace real tensile tests.
- We verify the orientation distribution of the glass fiber component simulated by a commercial software moldflow. To this end, we compare the locally determined orientation tensor components determined from gray value 3D images to the simulated.

In context of multi-scale modelling, we certainly make large progress as we can acquire reliable data of the composite material's microstructure, find a suitable model representation of the fiber component, use this geometrical model in a simulation technique and verify it by real experiments. This means a consistency along the physical scale, which I stated in the introduction.

4.3 Outlook

In future work regarding the microstructural noise in polycrystals, several aspects are open to investigate. There is still the question to answer, if the observed distribution of cell diameters can be efficiently accounted for by a few moments of the observed distribution. In our investigation we did not go beyond the negotiation, that the first moment, i.e. the mean grain diameter is not sufficient in context of ultrasonic microstructural noise. The chances are that the uncertainty is higher if the model fit is based on a distribution of 2D diameter than the 3D measure of grains. As the acquisition of 3D DCT data is expensive and available just for a narrow range of polycrystals, the uncertainty caused by 2D data should be quantified in the future. The proposed simulation technique of backscattered ultrasonic signals might be verified by real experiments. Here is a large gap to close, since physical methods do not exist for measuring the isolated effect of ultrasound scattering. A possible, even if complex attempt to quantify the attenuation in its contributing parts: absorption, diffraction, geometrical and coupling losses, and the scattering.

The gain of insights regarding the GFRP materials is high, i.e. for GFRP with short glass fibers and up to 20 weight percents. This is due to the previously available knowledge about GFRP materials, but also due to large researching effort from

interdisciplinary contributors involved in the projects. Diebels and Rjasanow 2019 dedicate a book to the understanding of GFRP materials, their behavior during mechanical loading and the processes during failure, where our contribution is a part of. However, our analysis of the data available does not tap the full potential (Baranowski et al. 2019). The exploitation of the acquired data to the full potential is currently beyond the computational possibilities. One possible attempt to face this problem could be to utilize machine learning methods.

Bibliography

Alpers, A., A. Brieden, P. Gritzmann, A. Lyckegaard, and H. F. Poulsen (2015). "Generalized balanced power diagrams for 3D representations of polycrystals". In: *Philosophical Magazine* 95.9, pp. 1016–1028.

Andrä, H., D. Dobrovolskij, K. Schladitz, S. Staub, and R. Müller (2019). "Modelling of Geometrical Microstructures and Mechanical Behaviour of Constituents". In: Springer, pp. 31–56.

Auld, B. (1979). "General electromechanical reciprocity relations applied to the calculation of elastic wave scattering coefficients". In: *Wave motion* 1.1, pp. 3–10.

Baranowski, T., D. Dobrovolskij, K. Dremel, A. Hölzing, G. Lohfink, K. Schladitz, and S. Zabler (2019). "Local fiber orientation from X-ray region-of-interest computed tomography of large fiber reinforced composite components". In: *Composites Science and Technology* 183, p. 107786.

Bertrand, J. (1889). *Calcul des probabilités*. Gauthier-Villars.

Bhandari, Y., S. Sarkar, M. Groeber, M. Uchic, D. Dimiduk, and S. Ghosh (2007). "3D polycrystalline microstructure reconstruction from FIB generated serial sections for FE analysis". In: *Computational Materials Science* 41.2, pp. 222–235.

Brown, L. G. (1992). "A survey of image registration techniques". In: *ACM computing surveys (CSUR)* 24.4, pp. 325–376.

Chiu, S. N., D. Stoyan, W. S. Kendall, and J. Mecke (2013). *Stochastic geometry and its applications*. John Wiley & Sons.

Daley, D. J. and D. Vere-Jones (2003). *An introduction to the Theory of Point Processes: Elementary Theory and Methods*. 2nd. Vol. 1. New York: Springer.

Desch, C. H. (1912). "The structure of metals". In: *Science Progress in the Twentieth Century (1906-1916)* 7.25, pp. 87–103.

Diebels, S. and S. Rjasanow (2019). *Multi-scale Simulation of Composite Materials: Results from the Project MuSiKo*. Springer.

Dobrovolskij, D. and K. Schladitz (2022). "Simulation of Ultrasonic Backscattering in Polycrystalline Microstructures". In: *MDPI Acoustics* 4, pp. 139–167.

Fan, Z., Y. Wu, X. Zhao, and Y. Lu (2004). "Simulation of polycrystalline structure with Voronoi diagram in Laguerre geometry based on random closed packing of spheres". In: *Computational materials science* 29.3, pp. 301–308.

Frangi, A. F., W. J. Niessen, K. L. Vincken, and M. A. Viergever (1998). "Multiscale vessel enhancement filtering". In: *Medical Image Computing and Computer-Assisted Intervention—MICCAI'98: First International Conference Cambridge, MA, USA, October 11–13, 1998 Proceedings 1*. Springer, pp. 130–137.

Fraunhofer ITWM, BV (2021). *MAVI Handbook*. `https://www.itwm.fraunhofer.de/content/dam/itwm/de/documents/BV_Infomaterial/BV_mavi-handbook-main.pdf`. Online; accessed 20 September 2021.

Hadwiger, H. (1959). "Vorlesungen über Inhalt, Oberfläche und Isoperimetrie". In: *Bull. Amer. Math. Soc* 65, p. 20.

Hawking, S. and L. Mlodinow (2010). *The Grand Design*. New York, NY: Random House.

Hirsekorn, S. (2014). "Theoretical description of ultrasonic propagation and scattering phenomena in polycrystalline structures aiming for simulations on nondestructive materials characterization and defect detection". In: *Proceedings of the 11th ECNDT Conference*.

Hoffman, E. J., S.-C. Huang, and M. E. Phelps (1979). "Quantitation in positron emission computed tomography: 1. Effect of object size." In: *Journal of computer assisted tomography* 3.3, pp. 299–308.

Horstemeyer, M. F. (2010). "Multiscale modeling: a review". In: *Practical aspects of computational chemistry: methods, concepts and applications*, pp. 87–135.

Huber, N., S. Kalidindi, S. Blügel, and W. Wenzel (2022). *Virtual Materials Design*. Frontiers Research Topics. Frontiers Media SA.

Jeulin, D. (2021). *Morphological models of random structures*. Springer.

Lee, J. G. (2016). *Computational materials science: an introduction*. CRC press.

Lu, Z., B. C. Khoo, H.-S. Dou, N. Phan-Thien, and K. S. Yeo (2006). "Numerical simulation of fibre suspension flow through an axisymmetric contraction and expansion passages by Brownian configuration field method". In: *Chemical engineering science* 61.15, pp. 4998–5009.

Ludwig, W., P. Reischig, A. King, M. Herbig, E. Lauridsen, G. Johnson, T. Marrow, and J.-Y. Buffiere (2009). "Three-dimensional grain mapping by x-ray diffraction contrast tomography and the use of Friedel pairs in diffraction data analysis". In: *Review of scientific instruments* 80.3.

Mason, W. P. and H. McSkimin (1947). "Attenuation and scattering of high frequency sound waves in metals and glasses". In: *The Journal of the Acoustical Society of America* 19.3, pp. 464–473.

Ohser, J. and F. Mücklich (2000). *Statistical analysis of microstructures in materials science*. John Wiley & Sons.

Ohser, J. and K. Schladitz (2009). *3D images of materials structures: processing and analysis*. John Wiley & Sons.

Pinter, P., B. Bertram, and K. A. Weidenmann (2016). "A novel method for the determination of fibre length distributions from μCT-data". In: *Conference on Industrial Computed Tomography (iCT)*.

Redenbach, C. (2009). "Microstructure models for cellular materials". In: *Computational Materials Science* 44.4, pp. 1397–1407.

Schneider, R. and W. Weil (2008). *Stochastic and integral geometry*. Vol. 1. Springer.

Šedivỳ, O., D. Westhoff, J. Kopeček, C. E. Krill III, and V. Schmidt (2018). "Data-driven selection of tessellation models describing polycrystalline microstructures". In: *Journal of Statistical Physics* 172.5, pp. 1223–1246.

Stanke, F. E. and G. Kino (1984). "A unified theory for elastic wave propagation in polycrystalline materials". In: *The Journal of the Acoustical Society of America* 75.3, pp. 665–681.

Torquato, S. (2013). *Random Heterogeneous Materials: Microstructure and Macroscopic Properties*. Vol. 16. Springer Science & Business Media.

Tromans, D. (2011). "Elastic anisotropy of HCP metal crystals and polycrystals". In: *Int. J. Res. Rev. Appl. Sci* 6.4, pp. 462–483.

Truell, R., C. Elbaum, and B. B. Chick (1969). *Ultrasonic methods in solid state physics*. New York NY: Acad. Press.

Vander Voort, G. F., S. R. Lampman, B. R. Sanders, G. J. Anton, C. Polakowski, J. Kinson, K. Muldoon, S. D. Henry, and W. W. Scott Jr (2004). "ASM handbook". In: *Metallography and microstructures* 9, pp. 44073–0002.

Walte, F., T. Schwender, S. Hirsekorn, F. Schubert, and M. Spies (2015). *Reaktorsicherheitsforschung - Vorhaben-Nr.: 1501442 Berechnung der Ultraschallstreuung für einen verbesserten Nachweis von rissartigen Fehlern in austenitischen Schweissnähten. Phase 1: Berechnung der Ultraschallstreuung für 2D Schweissnahtmodelle*. Tech. rep. Fraunhofer-Institut für Zerstörungsfreie Prüfverfahren IZFP, Saarbrücken.

Walz, G. (2004). *Lexikon der Mathematik*. Spektrum Akademischer Verlag.

Wirjadi, O., K. Schladitz, P. Easwaran, and J. Ohser (2016). "Estimating fibre direction distributions of reinforced composites from tomographic images". In: *Image Analysis & Stereology* 35.3, pp. 167–179.

Yasuda, K., S. Henmi, and N. Mori (2005). "Effects of abrupt expansion geometries on flow-induced fiber orientation and concentration distributions in slit channel flows of fiber suspensions". In: *Polymer composites* 26.5, pp. 660–670.

Part II

Publications

acoustics

MDPI

Article

Simulation of Ultrasonic Backscattering in Polycrystalline Microstructures

Dascha Dobrovolskij [1,*] and Katja Schladitz [2]

[1] Faculty of Engineering, University of Applied Sciences, Würzburger Straße 45, D-63743 Aschaffenburg, Germany
[2] Fraunhofer-Institut für Techno- und Wirtschaftsmathematik, Fraunhofer-Platz 1, D-67663 Kaiserslautern, Germany; katja.schladitz@itwm.fraunhofer.de
* Correspondence: dascha.dobrovolskij@th-ab.de

Abstract: Ultrasonic testing of polycrystalline media relies heavily on simulation of the expected signals in order to detect and correctly interpret deviations due to defects. Many effects disturb ultrasonic waves propagating in polycrystalline media. One of them is scattering due to the granular microstructure of the polycrystal. The thus arising so-called microstructural noise changes with grain size distribution and testing frequency. Here, a method for simulating this noise is introduced. We geometrically model the granular microstructure to determine its influence on the backscattered ultrasonic signal. To this end, we utilize Laguerre tessellations generated by random sphere packings dividing space into convex polytopes—the cells. The cells represent grains in a real polycrystal. Cells are characterized by their volume and act as single scatterers. We compute scattering coefficients cellwise by the Born approximation. We then combine the Generalized Point Source Superposition technique with the backscattered contributions resulting from the cell structure to compute the backscattered ultrasonic signal. Applying this new methodology, we compute the backscattered signals in a pulse-echo experiment for a coarse grain cubic crystallized Inconel-617 and a fine grain hexagonal crystallized titanium. Fitting random Laguerre tessellations to the observed grain structure allows for simulating within multiple realizations of the proposed model and thus to study the variation of the backscattered signal due to microstructural variation.

Keywords: microstructural noise; grain size distribution; model fitting; Laguerre tessellation

Citation: Dobrovolskij, D.; Schladitz, K. Simulation of Ultrasonic Backscattering in Polycrystalline Microstructures . *Acoustics* **2022**, *4*, 139–167. https://doi.org/10.3390/acoustics4010010

Academic Editors: Gaofeng Sha and Theodore E. Matikas

Received: 29 November 2021
Accepted: 8 February 2022
Published: 18 February 2022

1. Introduction

Metallic alloys tailor-made for extremely demanding applications like in turbine blades are particularly expensive, as corrosion resistance and mechanical strength are achieved using noble metals and applying sophisticated manufacturing methods. Hence, it is essential to keep the manufacturing process stable and to ensure the construction elements to be defect-free and long-lasting.

Ultrasonic testing is a non-destructive testing technique particularly popular due to its high penetration depth compared to other non-destructive methods like Eddy current, magnetic particle inspection or X-ray based ones [1]. Moreover, ultrasonic testing can be conducted using mobile devices. These two properties enable for instance inspection of thick and very large metallic components like ship propellers in place [2]. However, ultrasonic testing relies heavily on correct interpretation of the measured signals. This work contributes to improving this interpretation by quantifying the so-called microstructural noise due to scattering of ultrasonic signals by the granular microstructure of metal alloys.

Metal alloys and many ceramics feature so-called polycrystalline microstructures consisting of grains defined by their local crystallographic orientation [3] and size [4,5]. Ultrasonic waves are scattered at grain interfaces [6]. As a consequence, ultrasonic signals measured in a polycrystal comprise all echos caused by the microstructure. This hampers the detection of defects due to overlap of many echos.

A wave is attenuated in the medium in which it propagates [7]. The scattering at grain boundaries introduces a flux of energy from the propagating wave and thus contributes to attenuation [8]. Truell et al. [7] describe the relations between scattering and attenuation in complex media formally:

> "The term "attenuation" is used throughout to mean energy losses (as measured by amplitude decay) arising from all causes when ultrasonic waves are propagated through a solid medium. These "total" losses can be classed broadly as scattering and absorption arising from the intrinsic physical character of the solid under study, as well as diffraction, geometrical, and coupling losses."

There have been a variety of attempts to quantify the scattering caused by microstructure, starting with very simple microstructural models. Truell et al. [7] and Ishimaru [9] define the scattering cross-section of a volume element as observed scattered power flux density along a spatial direction. According to this definition, Truell et al. [7] calculate normalized cross-sections for a variety of examples where a homogeneous isotropic sphere is embedded in a homogeneous isotropic matrix, as for example a magnesium sphere embedded in stainless steel.

Rose [10] captures microstructural noise in the context of scattering in polycrystals by placing point-shaped scatterers with random scattering coefficients at random spatial positions. This strategy is further pursued in [11,12]. Microscopic inhomogeneities in a polycrystal are thus captured using prior knowledge about the number of scatterers, while their relative positions are ignored. Hirsekorn [13] describes scattering in a system of closely packed scatterers as a function depending on scatterers' volume and stresses the need for ultrasonic scattering simulation methods using an explicitly given system of closely packed scatterers as theoretically anticipated.

More recently, the granular microstructure of polycrystalline materials is modeled by spatial tessellations [14–21]. Ultrasonic wave propagation is simulated in extruded 2D [22] or just 2D [23] tessellations only, even in rather recent publications. Ryzy et al. [24] and Van Pamel et al. [25–27] simulate ultrasonic wave propagation in truly 3D structures. Both groups apply NEPER [28] to first generate 3D Poisson Voronoi tessellations and then regularize them by shifting the cell generators. In [27], even an exponentially decaying two-point correlation function as assumed in analytical models is derived that way. Subsequently, displacement fields are computed in finite element mesh (FEM) representations of the regularized cell systems. To this end, Van Pamel et al. [25–27] use the GPU based FE software POGO [29], while Ryzy et al. [24] rely on the commercial software package PZFLEX (Weidlinger Associates Inc., Washington, DC, USA). Despite the computational load, in [27], the displacements are calculated for a system of more than 10,000 cells. However, the tessellation models are not fitted to an observed real polycrystalline microstructure. Thus, material specific behavior is restricted to the mean cell or grain size and usage of the respective elastic material constants.

We describe a complete simulation workflow for simulating the microstructural noise caused by the grain structure of the investigated material. More precisely, our simulation accounts for the spatial and size distribution of the grains. We model the microstructure including the scatterer volumes, simulate backscattering from the entire microstructure, and compute time domain signals. We make heavy use of the Born approximation of the scattering field when it is small compared to the incident field. This assumption holds in our case of microstructural noise, as long as the wavelength of the propagating wave stays larger than the scatterers' dimensions.

Stanke and Kino [8] developed a unified theory for elastic wave propagation in polycrystalline materials accounting accurately for microscopic inhomogeneities in the case of time-harmonic elastic waves, in particular phase velocity variations and attenuation due to scattering. The polycrystal is represented by the geometric correlation function.

We combine the scattering theory from [8] with an explicit spatial microstructure model as used in [5] to simulate the backscattered transient ultrasonic signal. To this

end, we use microstructural information from light-microscopy and diffraction computed tomography. Both techniques are destructive in the sense that samples need to be cut and further prepared to obtain as detailed microstructural information as needed here. Based on the quantitative geometric information thus derived, we fit microstructure models specifically to the considered materials. More precisely, we derive a virtual representation of a polycrystalline single-phase alloy as a realization of a random tessellation model. The cells of the tessellation represent the grains and cell volumes follow the grain volume distribution observed in the real material. In enlarged volumes, generated from the fitted tessellation model, we compute the backscattering contributions of all cells, superpose them in Fourier space, and transform the power spectrum back into time domain.

We apply the model based spectral simulation approach to a cubically crystallized Inconel-617 observed in light-microscopic images of planar sections through the microstructure and a hexagonally crystallized titanium given as fully three-dimensional X-ray diffraction computed tomography data set. We model both alloys as a single-phase polycrystal. The titanium features fine grains, while the Inconel's microstructure is coarse. We expect our study to contribute to a deeper understanding of the relation between material dependent 3D microstructure and the ultrasonic wave propagation. This contributes to better interpretation of measured ultrasonic signals.

This paper is organized as follows: In Section 2 we describe the general virtual experiment. We summarize the needed scattering theory (in Section 2.1) including the geometric correlation function (in Section 2.1.1) and scattering coefficients (in Section 2.1.2). Section 2.2 is dedicated to modeling the single-phase polycrystalline microstructures using random Laguerre tessellations (in Section 2.2.1) with log-normally distributed grain volume (in Section 2.2.2) and fitting the model to real microstructures (in Section 2.2.3). In Section 2.3, we close the gap between the fitted microstructure model and computing of ultrasonic signals in its realizations. In Section 3, we model the microstructures of the Inconel-617 (in Section 3.2) and the titanium (in Section 3.3). Section 4 summarizes our findings including microstructure model parameters and ultrasonic signals for the Inconel-617 (in Section 4.1) and for the titanium (in Section 4.2). Results and future topics are finally discussed in Section 5, followed by the conclusion in Section 6.

2. Methods

We perform a virtual ultrasonic pulse-echo-test in an explicitly given 3D microstructure generated by a stochastic microstructure model as sketched in Figure 1. The microstructure model's parameters are determined by fitting to the grain size distribution observed in images. Using the found model parameters, we generate representative realizations of the model. In these 3D microstructures, we finally simulate numerically the ultrasonic testing by the pulse-echo-technique as sketched in Figure 1. We do not simulate the back wall response. Instead, we compute the backscattered contribution from the entire microstructure for each realization of the model. We superpose the response signals in frequency domain yielding a spectrum. Finally, we apply the Fourier transform resulting in a time-domain signal. Altogether, a set of 3D microstructures leads to a corresponding set of time-domain signals.

This paper devises a method for computing ultrasonic microstructural noise based on a geometric model of the investigated polycrystalline material. More precisely, we simulate scattering due to individual grains. Note that this is not the same as the so-called grain noise well-known from ultrasonic experiments. The difference is due to the virtual experiment being still much simpler than the real one as it does not capture at all multiple scattering—a non-negligible source of microstructural noise in real ultrasonic experiments.

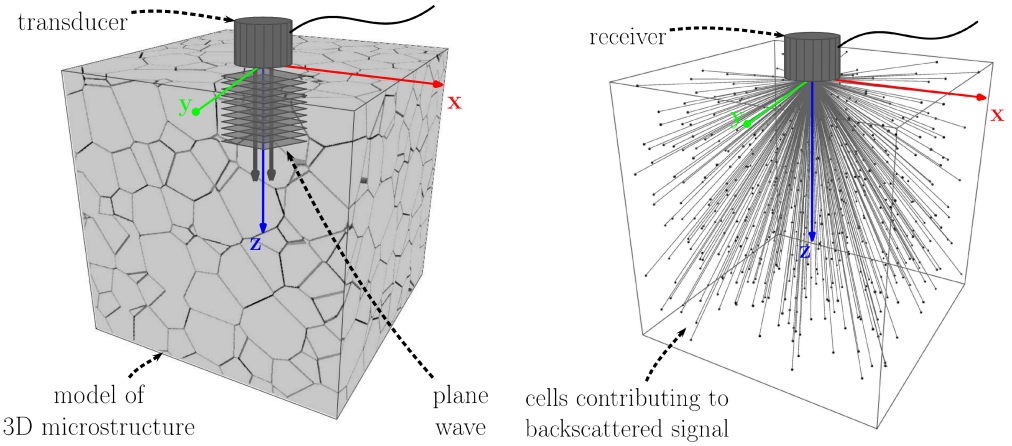

(**a**) general setup (**b**) backscattering

Figure 1. (**a**) Experimental setup assumed throughout including the particular choice of the global Cartesian coordinate system with top-down z-axis. The transducer is both transmitter and receiver for longitudinally polarized waves. In (**b**), dots mark the centers of the cells visualized in (**a**). The entire microstructure contributes to the received backscattered signal.

We compute the wave propagation for two microstructures, i.e., Inconel-617 and titanium, with strongly varying properties, see Table 1. ASTM classifies microstructures by average grain diameters observed in 2D micrographs [30]. According to this classification, Inconel-617 is class no. 2 (0.185 mm) and titanium class no. 8 (0.022 mm). Scattering coefficients are computed for nickel, too, to compare with [13,31]. Due to lack of microstructure data, we do not fit a model but calculate the spatial scattering function based on the effective diameter from [13,31], only.

We model the propagating wave as a planar one, as indicated in Figure 1. That is, the wave is constant in a plane perpendicular to the propagation direction.

Table 1. Elastic constants of the three considered alloys. Nickel [13] and Inconel-617 [32] feature face centered cubic (fcc) single crystal structures and titanium [33] a hexagonally closely packed (hcp) one. The material specific density ϱ represents the material in both conditions.

	Single Crystal					**Polycrystal**		**Density**	
	C_{11} [GPa]	C_{12} [GPa]	C_{13} [GPa]	C_{33} [GPa]	C_{44} [GPa]	$\lambda_{\text{Lamé}}$ [GPa]	$\mu_{\text{Lamé}}$ [GPa]	ϱ $[\frac{\text{g}}{\text{cm}^3}]$	**Featured in Section**
nickel	250	-	-	160	118.5	-	-	8.905	Section 2.1.2
Inconel-617	243.3	-	-	163.05	134.3	134.5	82.9	8.36	Sections 3.2 and 4.1
titanium	160	66	181	90	46.5	76.17	43.39	4.51	Sections 3.3 and 4.2

Our workflow is sketched in Figure 2. There are three steps to be taken: First, the transducer as well as the transducer's bandwidth are discretized according to the sampling theorem [34]. The required parameters are listed in the upper left box of Figure 2. Also in the first step, the microstructure model is fitted and representative realizations are generated, see the right upper boxes. In the second step, the displacement field at scatterers' positions due to wave propagation in momentum space is computed. Finally, in the third step, we transform the signal into the time domain using the Fast Fourier Transformation. Note that the scheme in Figure 2 is already specialized to modelling the microstructure by Laguerre tessellations generated by random packings of hard spheres.

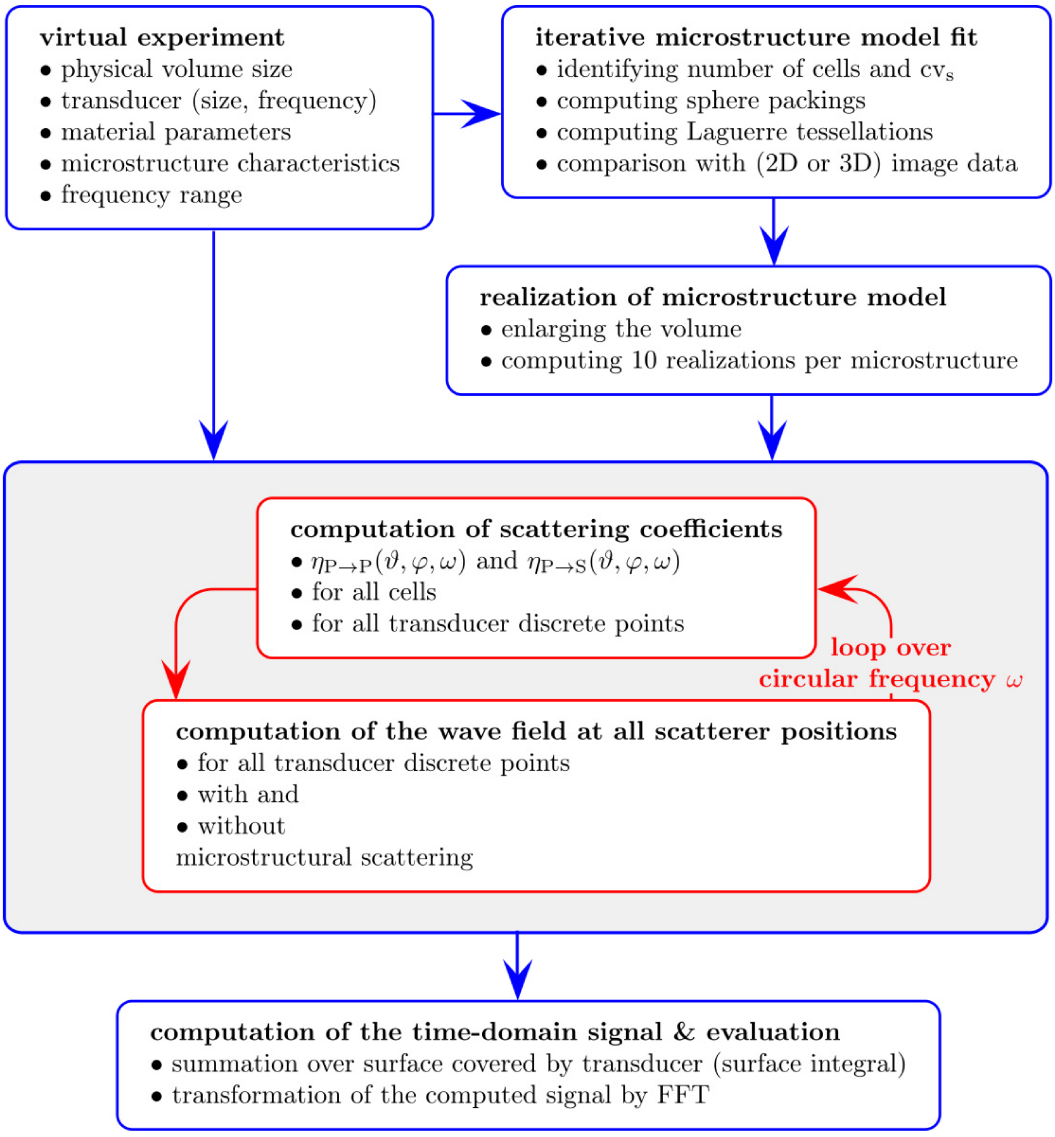

Figure 2. Proposed workflow.

2.1. Scattering Theory

The ensemble average of a physical quantity is the mean of this quantity over a state of the considered system [35,36] with the region or time interval of averaging being comparable to the slot when or where the observed system changes its state. Scattering effects due to local microstructural inhomogeneities vary with grain size and orientation, and thus have to be captured at the scale of the grains. The scattered energy densities for a certain volume of a particular medium can be derived from the microscopic position dependent material characteristics like single crystal elastic constants and density and the ensemble average.

Ensemble averaging for ultrasonic propagation in polycrystalline materials has been used for a long time, see e.g., [37–39]. Here, we follow the idea of Hirsekorn [13,40] and investigate the effects of closely packed scatterers. In [13], the elastodynamic equation of motion is solved assuming small deviations due to microstructural variation. This variation is captured by modelling the microstructure as a system of closely packed scatterers exposed to the propagating ultrasonic wave. The scattered energy flux relates the frequency dependent time harmonic displacement field for one vibrating cycle and the material specific stress tensor, see [7] for more details.

The Born series [41] for the propagating wave yields an approximation of the resulting displacement field. Material dependent parameters like size and orientation distribution of

the grains are accounted for by the geometric correlation function. Ensemble averaging is applied to the Born series terms. Finally, the energy flux is derived as an infinite sum, time averaged over one vibration cycle. The n-th order Born approximation of energy flux is the corresponding n-th partial sum, $n = 0, 1, \ldots$. It represents the incident and scattered waves' interaction with the microscopic inhomogeneity of the material. Hirsekorn uses the lowest non-zero order Born approximation to derive an analytical expression of the ensemble averaged total energy flux due to scattering waves for both, incoming and outgoing waves [13]. Thus, using this approach, only first-order scattering events are taken into account, no multiple scattering. The sum of outgoing and incoming waves equals zero due to the conservation of energy [13]. Here, we consider the outgoing waves, only, as we aim at revealing the backscattered wave contributions.

2.1.1. Geometric Correlation Function

Ensemble averaging in polycrystals incorporates microstructural features by multiple-point correlation functions of the local crystal orientations. In order to be feasible, approximations use a variety of simplifications, e.g., only 2-point or pair-correlations. If the orientations of grains are assumed to be independently distributed, then the 2-point orientation correlation boils down to the orientation distribution function multiplied by the geometric 2-point correlation—the probability of two points falling into the same grain [42,43]. The latter depends exclusively on the distance of the considered points if the structure is macroscopically homogeneous and isotropic.

Stanke and Kino [8] incorporate the 2-point correlation function $W(r)$ into their unified theory of elastic wave propagation assuming it to decline exponentially: $W(r) = \exp\left(-r/\bar{\ell}\right)$, where r is the distance of a point pair and $\bar{\ell}$ is the mean chord length of the grains, also called mean free path length or correlation distance. This simple shape of the orientation correlation is convenient yet not realistic, see [44,45] and references therein. Following [8], Hirsekorn [13,40] derives from $\bar{\ell}$ the effective volume V_{eff} of a scatterer as

$$V_{\text{eff}} = \int_{\psi=0}^{\pi} \int_{\theta=0}^{2\pi} \int_{r=0}^{\infty} \exp\left(-\frac{r}{\bar{\ell}}\right) dr\, d\theta\, d\psi = 8\pi\bar{\ell}^3.$$

Roughly speaking, V_{eff} can be interpreted as the volume that scatters if the correlation length is $\bar{\ell}$. Plugging in V_{eff} into the Born approximation yields the scattering coefficients reported in [13].

We aim at emphasizing the contribution of individual grains to microstructural noise. Thus, we follow [13,40] in treating the grains as homogeneous and completely independent scatterers. However, we observe the effective scatterers' volumes V_{eff} directly as the cell volumes in our tessellation model realizations. The effective diameter d_{eff} of a cell or grain is derived as the diameter of the sphere of volume V_{eff}

$$d_{\text{eff}} = \left(6/\pi V_{\text{eff}}\right)^{1/3}. \tag{1}$$

2.1.2. Spatial Scattering Function

Evaluating the second order term of the Born approximation and utilizing Equation (1) yields analytical representation of scattering coefficients $\eta(\vartheta, \varphi, \omega)$ with $\omega = 2\pi f$ being the corresponding circular frequency and f a fixed frequency. $(\vartheta, \varphi) \in [0, \pi] \times [-\pi, \pi]$ are the spherical polar coordinates of the local coordinate system, whereat $\eta(\vartheta, \varphi, \omega)$ maps the scattering coefficients along spatial directions around a scattering volume V_{eff}. Thus, we call this analytical representation of scattering behavior spatial scattering function.

The following notation is used throughout: Denote by k_P, k_S the wave numbers for the pressure (P) and shear (S) waves, respectively. The subscript is made of incoming→outgoing wave, which is either pressure or shear, respectively. The spatial scattering functions are:

$$\begin{aligned}\eta_{\mathrm{P}\to\mathrm{P}}(\vartheta,\varphi,\omega) =& \frac{k_\mathrm{P}^8 d_\mathrm{eff}^3 \pi}{\sqrt[3]{6}(4\pi\varrho\omega^2)^2} \frac{1}{\left(1+k_\mathrm{P}^2(1+\cos\vartheta)\frac{d_\mathrm{eff}^2}{2\sqrt[3]{6}}\right)^2} \\ & \left(A_2\cos^4\vartheta + A_1\sin^4\vartheta + 2(A_5+2A_6)\sin^2\vartheta\cos^2\vartheta\right)\end{aligned} \tag{2}$$

$$\begin{aligned}\eta_{\mathrm{P}\to\mathrm{S}}(\vartheta,\varphi,\omega) =& \frac{k_\mathrm{P}^3 k_\mathrm{S}^5 d_\mathrm{eff}^3 \pi}{\sqrt[3]{6}(4\pi\varrho\omega^2)^2} \frac{1}{\left(1+(k_\mathrm{P}^2+k_\mathrm{S}^2+2k_\mathrm{P}k_\mathrm{S}\cos\vartheta)\frac{d_\mathrm{eff}^2}{4\sqrt[3]{6}}\right)^2} \\ & \left(A_6(2-\sin^2\vartheta) + A_4\sin^2\vartheta + (A_2+A_1-2A_5-4A_6)\sin^2\vartheta\cos^2\vartheta\right)\end{aligned} \tag{3}$$

$$\begin{aligned}\eta_{\mathrm{S}\to\mathrm{P}}(\vartheta,\varphi,\omega) =& \frac{k_\mathrm{P}^5 k_\mathrm{S}^3 d_\mathrm{eff}^3 \pi}{\sqrt[3]{6}(4\pi\varrho\omega^2)^2} \frac{1}{\left(1+(k_\mathrm{P}^2+k_\mathrm{S}^2+2k_\mathrm{P}k_\mathrm{S}\cos\vartheta)\frac{d_\mathrm{eff}^2}{4\sqrt[3]{6}}\right)^2} \\ & \Big(A_4\sin^4\vartheta\sin^4\varphi + A_6(\sin^4\vartheta\cos^4\varphi+\cos^4\vartheta) \\ & +2(A_9+2A_{10})\sin^2\vartheta\cos^2\vartheta\cos^2\varphi \\ & +2(A_7+2A_8)\sin^2\vartheta\sin^2\varphi(\sin^2\vartheta\cos^2\varphi+\cos^2\vartheta)\Big)\end{aligned} \tag{4}$$

$$\begin{aligned}\eta_{\mathrm{S}\to\mathrm{S}}(\vartheta,\varphi,\omega) =& \frac{k_\mathrm{S}^8 d_\mathrm{eff}^3 \pi}{\sqrt[3]{6}(4\pi\varrho\omega^2)^2} \frac{1}{\left(1+k_\mathrm{S}^2(1+\cos\vartheta)\frac{d_\mathrm{eff}^2}{2\sqrt[3]{6}}\right)^2} \\ & \Big(A_8+A_{10}+(A_8-A_{10})\sin^2\vartheta\sin^2\varphi \\ & +(A_6+A_4-2A_7-4A_8)\sin^2\vartheta\sin^2\varphi(\sin^2\vartheta\cos^2\varphi+\cos^2\vartheta) \\ & +2(A_6-A_9-2A_{10})\sin^2\vartheta\cos^2\vartheta\cos^2\varphi\Big)\end{aligned} \tag{5}$$

with ϱ being the materials' density. Equations (2)–(5) presume a specific incoming pressure or shear wave given by wave vector $(0,0,1)^T$ in both cases, and either the pressure polarization vector $(0,0,1)^T$ or shear polarization vector $(1,0,0)^T$. This presumption sets up the relation between single scatterers and the transducer, which is the source of the incoming wave. As in [13,46], this models how single scatterers and the transducer interact. Here, $A_1,\ldots,A_{10}$ denote the ensemble averaged elastic constants from [40] listed in Table 2 below.

The spatial scattering functions are defined in intrinsic coordinates, with the origin of the local coordinate system in the center of scattering volume V_eff. In terms of Cartesian coordinates $(x_1,x_2,x_3)^T = r(\sin\vartheta\cos\varphi,\ \sin\vartheta\sin\varphi,\ \cos\vartheta)^T$, the positive x_3-axis of the local coordinate system is aligned with the positive z-axis of the global coordinate system. Figure 3 shows the spatial scattering function for a single scatterer in nickel (see also Table 1). In the following, we use Cartesian coordinates and the base unit mm^{-1} in all graphical representations of the spatial scattering functions.

In [13], the normalized scattered wave coming from a point in the material is plotted in two dimensions, in [31] the same is done for the normalized scattered wave coming into a scatterer. These quantities depend however on all three spatial directions. We

therefore visualize the normalized scattered wave coming from a scatterer from [13] in three dimensions.

Table 2. Ensemble averaged elastic constants (in GPa^2) as used for the calculation of backscattering coefficients [40].

Abbreviation	Ensemble Averaged Elastic Constants	Nickel	Inconel-617	Titanium
A_1	$\langle (C'_{1133})^2 \rangle$	370.44	608.15	39.86
A_2	$\langle (C'_{3333})^2 \rangle$	658.55	1 081.12	30.96
A_4	$\langle (C'_{1233})^2 \rangle$	205.80	337.86	29.56
A_5	$\langle C'_{1133} C'_{3333} \rangle$	−329.27	−540.58	−17.84
A_6	$\langle (C'_{1333})^2 \rangle$	411.59	675.72	7.14
A_7	$\langle C'_{1113} C'_{2213} \rangle$	−102.90	−168.93	−12.71
A_8	$\langle (C'_{1213})^2 \rangle$	205.80	337.86	15.53
A_9	$\langle C'_{1113} C'_{1333} \rangle$	−308.69	−506.79	3.79
A_{10}	$\langle (C'_{1313})^2 \rangle$	370.44	608.15	21.16

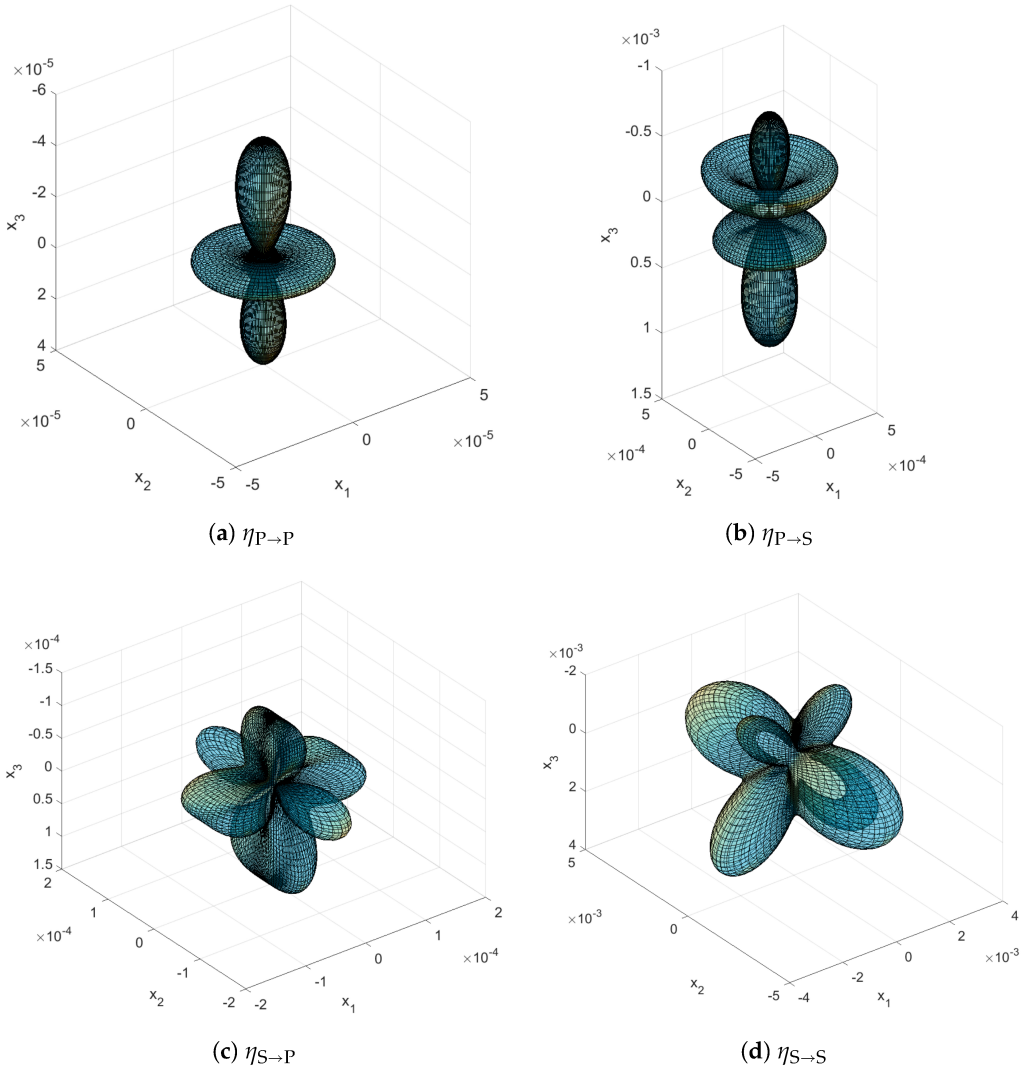

(**a**) $\eta_{P\to P}$ (**b**) $\eta_{P\to S}$

(**c**) $\eta_{S\to P}$ (**d**) $\eta_{S\to S}$

Figure 3. Spatial scattering functions $\eta(\vartheta, \varphi, 2\pi\,10\,\mathrm{MHz})$ for a single scatterer of size $d_{\mathrm{eff}} = 54.5\,\mu\mathrm{m}$ in nickel. For every unit vector $(x_1, x_2, x_3) = (\sin\vartheta\cos\varphi, \sin\vartheta\sin\varphi, \cos\vartheta)$, the function value $\eta(\vartheta, \varphi, 2\pi\,10\,\mathrm{MHz})$ is represented here as the length of the vector in the corresponding direction.

To summarize, we model each grain as a cell contributing by its volume V_{eff} to the backscattered ultrasonic signal. The cell's orientation is accounted for by the ensemble averaging. The Born approximation relies on a macroscopic isotropy of the microstructure. That means, in all further steps, cells do not have a specific orientation anymore. Note however, that our workflow in principle carries over to modelling the orientation and its scattering effect, too.

2.2. Geometric Modelling of Polycrystalline Microstructures

There is a wide variety of geometric characteristics describing spatial size and shape of grain systems. A basic and in some sense complete system of characteristics for the grains are the intrinsic volumes or Minkowski functionals [47]. Ohser's algorithm allows to estimate them efficiently based on 3D image data [48]. For the titanium, we use the volume V, and the isoperimetric shape factor

$$s \quad = \quad 6\sqrt{\pi}V/S^{3/2} \tag{6}$$

derived from volume and surface area S. This dimensionless index, often called sphericity, is normalized such that it attains the value 1 for a perfect sphere. Moreover, $0 \leq s \leq 1$ with 1 being reached by the sphere, only.

For the Inconel-617, we use the maximal Feret or caliper diameter of the 2D grain cross sections—basically the longest Euclidean distance of two points in that grain.

2.2.1. Laguerre Tessellations

Random tessellation models are used to model the grain structure of polycrystalline materials in many contexts [20,21,49,50]. Most common are Voronoi tessellations, dividing space by assigning each point to the nearest generator. In Laguerre tessellations, this well-known rule is generalized such that generator's attraction is steered by an additional weight [51]. The thus achieved higher flexibility allows for better control over cell sizes, see Figure 4. Laguerre tessellations generated by random closed packings of spheres are a standard model for rigid foams [52–55] and popular models for polycrystals [5]. Methods for fitting in the statistical sense [52], reconstruction from 2D images [56] or cell centroids and volumes in 3D [21], as well as approximation based on 3D image data [20] are available.

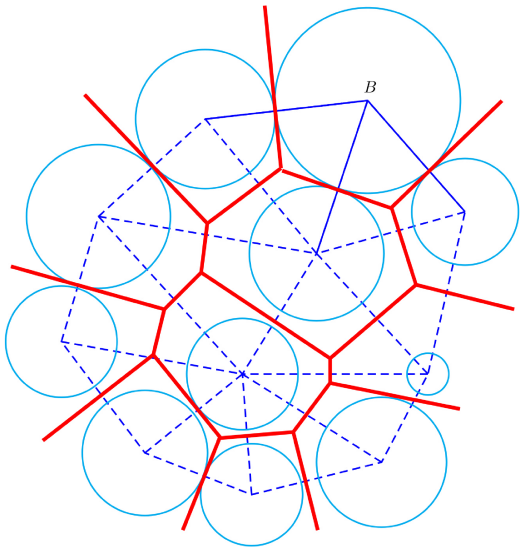

Figure 4. 2D illustration for the construction of a Laguerre tessellation. The cyan circles are the generators with their weights, the red solid lines are the resulting faces of the Laguerre tessellation.

Here, we use Laguerre tessellations generated by random packings of spheres. We use the force biased collective rearrangement algorithm [57], an effective modification of [58] in the way described by [59,60]. This choice is motivated by the good control over

the cell volume distribution this model allows. Note that Fan [5] builds on a collective rearrangement packing, too [61,62].

For the sake of independence, we sketch the mechanism of the force biased packing algorithm: At the beginning of the packing, spheres with an outer soft shell and an inner hard core are placed in the container. The shells are allowed to overlap. Spheres push each other away with forces depending on the overlap. In a collective rearrangement step, they move according to the cumulative forces of repulsion. Then, the outer shells of the spheres decrease while the cores grow up to the size that just prevents overlap of the cores. These steps are iterated. The packing ends if the desired packing density—proportion of the volumes of the sphere system and the container—is reached or the shells have disappeared or the number of iterations has reached a predefined limit. See Figure 5 for the volume rendering of a thus derived sphere system.

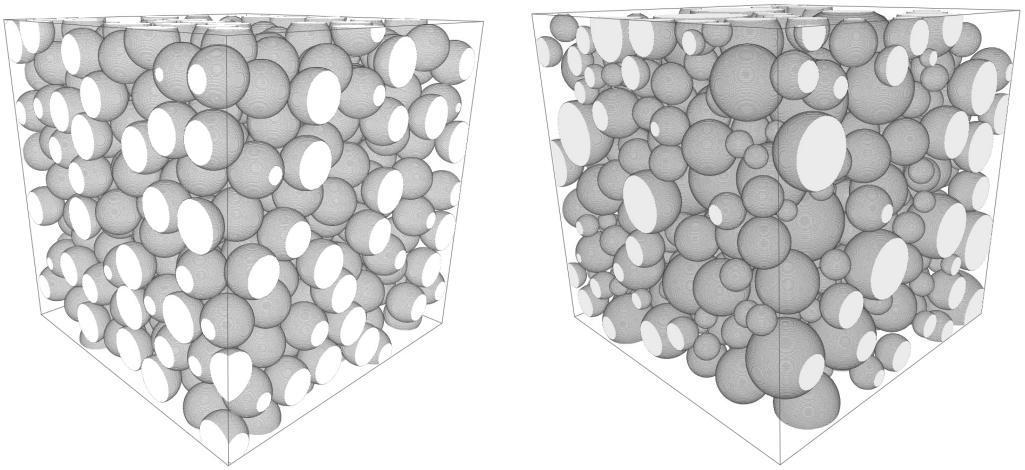

Figure 5. Volume renderings of force biased packings of 500 spheres in the unit window $[0,1]^3$. Both with volume fraction $V_V = 52.1\%$. **Left**: with constant sphere volume $V = 0.011$. **Right**: with log-normally distributed sphere volumes ($\mu_{v_s} = -7.67$ and $\sigma_{v_s} = 1.26$).

The cell structure modeling the polycrystal is then derived from the sphere packing by the Laguerre mechanism: We denote by $x_i \in \mathbb{R}^3$ the center and by $r_i \in \mathbb{R}$ the radius of sphere i for $i = 1 \dots N_C$. Then $(x_i, r_i)_{i=1}^{N_C}$ is a set of generators with non-negative weights. A point $y \in \mathbb{R}^3$ is assigned to the cell $C(x_i, r_i)$ generated by x_i if its weighted distance to x_i is smaller than to any other generator. The point y is assigned to the i-th cell if $\|x_i - y\|^2 - r_i^2$ is less than $\|x_j - y\|^2 - r_j^2$ for all $j \neq i$. The wall between two neighboring generators is the perpendicular bisector between their respective spheres, see Figure 4 for an illustration of the mechanism.

That way, our random system of non-overlapping spheres divides the space into convex cells $C(x_i, r_i)$ with diameters $d_{\text{eff},i}$ of volume equivalent sphere as given by (1). Additionally, we equip each cell with its center of mass m_i.

2.2.2. Grain Size Distribution

Grain sizes in polycrystalline materials are usually assumed to be log-normally distributed [4,63]. In Laguerre tessellations generated by dense sphere packings, the cell size distribution is dominated by the size distribution of the generating spheres [5,52]. We therefore model the sphere volumes v_s according to a log-normal distribution. The probability density function h of the log-normal distribution with parameters (μ, σ) is:

$$h(v_s|\mu,\sigma) = \frac{1}{v_s\sigma\sqrt{2\pi}} \exp\left(-\frac{(\ln v_s - \mu)^2}{2\sigma^2}\right).$$

Expected sphere volume $\overline{v}_s = V_V / N_V$ and the sphere volume standard deviation σ_{v_s} are then [52]

$$\overline{v}_s = \exp(\mu + \sigma^2/2)\,, \tag{7}$$

$$\sigma_{v_s} = (\exp(\sigma^2) - 1)\exp(2\mu + \sigma^2)\,. \tag{8}$$

On the other hand

$$\mu = \frac{1}{2}\log\left(\overline{V}^2/(\mathrm{cv}_s^2 + 1)\right)\,, \tag{9}$$

$$\sigma = \sqrt{\log(\mathrm{cv}_s^2 + 1)} \tag{10}$$

with $\mathrm{cv}_s = \sigma_{v_s}/\overline{V}$ denoting the coefficient of variation of the sphere volume.

Note that the coefficients of variation of the resulting grain volumes cv_g and the generating spheres cv_s surely differ with $\mathrm{cv}_g > \mathrm{cv}_s$. For very dense sphere packings as in [5], the difference is small as the cells do not differ strongly from their generating sphere. If the sphere packing density V_V is lower, the difference grows. We use the cubic polynomial in cv_s fit to cv_g for the densely packed case from [5]. See [52] for a more general discussion.

2.2.3. Fitting the Geometric Model Based on 2D Image Data

Model fitting solely based on 2D image data is an ill-posed problem. In [56] an optimization based on a goodness-of-fit criterion for 2D slices is devised to avoid costly simulations of the full 3D Laguerre tessellations. However, [56] aims at exact reproduction of the observed 2D cell structure. Here, we can use a simpler approach, closer to [50]: We simulate 3D tessellations, compare 2D slices cut from them with our 2D observations, and alter the parameters to reduce the differences. This is repeated till the fit is sufficiently good.

First, we estimate the expected number of grains per volume N_V. There is no straight forward method to do so based on the observed grain number in planar sections N_A in case of Laguerre tessellations generated by sphere packings. However, for the special case of a spatial Voronoi tessellation generated by a Poisson point process [47] (10.74) yields:

$$N_A = 1.46\, N_V^{2/3}. \tag{11}$$

Following the recommendation from [47] to use this approximation for the non-Poisson case, too, we set the initial number of cells to the value which is expected for the Poisson Voronoi tessellation case. The initial guess for the coefficient of variation of the sphere volume distribution is set to 1.5 as this is about the center of the range $\mathrm{cv}_g \in [1.09, 2.13]$ for the grain volumes reported by [5].

We generate a force biased sphere packing using mean sphere volume V_V / N_V and $\mathrm{cv}_s = 1.5$, derive the Laguerre tessellation, extract planar sections, and compare them with the 2D micrographs based on the Feret diameters of the cells. We adjust the number of spheres in the random packing based on comparison of the maximal Feret diameters and iterate till the mean maximal Feret diameter (or the cell density) is met.

In the second step, the coefficient of variation of the sphere volumes cv_s is fit by a simple grid search. Again, we compute sphere packings and derive the corresponding Laguerre tessellations. We take five section planes in each of the three coordinate directions, measure the maximal Feret diameters, and compare the mean maximal Feret diameter and the standard deviation of the maximal Feret diameters in these 2D sections with the corresponding characteristics measured in the 2D micrographs. We finally choose the value for cv_s yielding the best agreement.

2.3. Simulation of Wave Propagation

We simulate the wave propagation in momentum space by calculating displacement at scatterers' positions, as drafted in Figure 1. First, we compute the displacement induced

by a propagating wave. We discretize the surface covered by the transducer by N_t source points $y_k \in \mathbb{R}^3,\ k = 1, \ldots, N_\mathrm{t}$. After all, we evaluate the energy contribution along these particular spatial directions, i.e., $m - y$. Here, $u^\mathrm{I} \in \mathbb{R}^3$ is the incoming polarization vector and $c^\mathrm{I} \in \mathbb{R}$ the group velocity, both determined by vectors y and m. The displacement $u_\alpha \in \mathbb{R}^3$ due to propagation of an elastic plane wave can be modelled at scatterers' positions as a superposition of all source points by

$$u_\alpha(m, \omega) = \frac{U^\mathrm{I}}{4\pi} \sum_{k=1}^{N_t} \frac{u^\mathrm{I} \exp\left((-j\omega\|m - y_k\|)/c^\mathrm{I}\right)}{\|m - y_k\|} \tag{12}$$

with α indicating incoming pressure (P) or shear (S) waves, j the complex unity and U^I denoting the amplitude of the propagating wave.

The second contribution is the displacement due to scattering at scatterers' position. We define the latter following Equation (8) in [64], namely:

$$u_{\alpha,\mathrm{sc}}(m, \omega) = \frac{U^\mathrm{I}}{4\pi} \frac{\exp\left((-j\omega\|m - y\|)/c^\mathrm{I}\right)}{\|m - y\|} \left(u^\mathrm{I} + \mathcal{R}_\mathrm{S} u_\mathrm{S}^\mathrm{R} + \mathcal{R}_\mathrm{P} u_\mathrm{P}^\mathrm{R}\right) \tag{13}$$

with $\mathcal{R}_\mathrm{S}$ and $\mathcal{R}_\mathrm{P}$ being the reflection coefficients. Thereby, all polarization vectors contribute to the result—those of the incoming (I) as well as those of the reflected (R) waves. We adapt Equation (13) by replacing the reflection coefficients by the scattering coefficients given analytically in Section 2.1.2. This yields

$$u_{\alpha,\mathrm{sc}}(m, \omega) = \frac{U^\mathrm{I}}{4\pi} \sum_{k=1}^{N_t} \frac{\exp\left((-j\omega\|m - y_k\|)/c^\mathrm{I}\right)}{\|m - y_k\|} \left(u^\mathrm{I} + \eta_{\alpha\to\mathrm{S}}(\vartheta_k, \varphi_k, \omega)\, u_\mathrm{S}^\mathrm{R} + \eta_{\alpha\to\mathrm{P}}(\vartheta_k, \varphi_k, \omega)\, u_\mathrm{P}^\mathrm{R}\right). \tag{14}$$

The polarization vectors $u_\alpha^R \in \mathbb{R}^3$ of the reflected contributions are evaluated in direction of the corresponding slowness vectors. Červený [65] defines the reflected slowness vector as a function of incoming slowness vector and thus the reflected contributions are governed by the corresponding slowness vectors i.e., $s_\alpha^\mathrm{R}(m - y)$. Also, the direction of reflected slowness vectors governs the scattering coefficients. The scattering coefficients in Equations (2)–(5) are derived as

$$\vartheta_k = \arctan\left(\frac{s_y(m - y_k)}{s_x(m - y_k)}\right)$$
$$\varphi_k = \arctan\left(\frac{s_z(m - y_k)}{\sqrt{s_x^2(m - y_k) + s_y^2(m - y_k)}}\right)$$

where the subscripts x, y, z represent the components of s_α^R. In Equation (14), the angle and frequency specific scattering coefficients depend on the single crystal parameters, but the group velocity c^I on the polycrystal's material parameters.

2.3.1. Reciprocity Relations

We follow [66] in applying the reciprocity relations for computing the displacement at the receiver's surface. In [66], a formalism for scattering of ultrasonic waves at scatterers is derived, in particular for the Born approximation. There, the received signal is defined as the integral over the scatterer's entire surface. Here, the displacement at the receiver is expressed by the superposition of displacement velocity $j\omega\, u$ and stress tensor $\underline{\underline{\sigma}}$ at all scatterers' positions m_i:

$$u(\omega) = \frac{j\omega}{4} \sum_{i=1}^{N_\mathrm{C}} \left(u_{\alpha,\mathrm{sc}}(m_i, \omega)\, \underline{\underline{\sigma}} - u_\alpha(m_i, \omega)\, \underline{\underline{\sigma}}_{\alpha,\mathrm{sc}}\right) \cdot \hat{n}\,, \tag{15}$$

where $\hat{n} \in \mathbb{R}^3$ is the normal to the scatterer' surface. Note that, although we account for one discrete point per scatterer, only, this scatterer is nevertheless assumed to be spherical. Thus, the point first reached by the wave is the one with surface normal pointing towards the transducer. Usually, transmitter and receiver are differentiated [66,67]. In our setting of a pulse-echo experiment, the transmitter however equals the receiver.

2.3.2. Modelling of the Bandwidth

In general, wave propagation is a time-dependent phenomenon. In [68], transient signals are computed based on the static continuous wave displacement method. We model the bandwidth f_m by

$$f_\mathrm{m} = \begin{cases} \sin^2\left(\pi \frac{f-f_\mathrm{l}}{f_\mathrm{r}-f_\mathrm{l}}\right) & , \quad f_\mathrm{l} < f < f_\mathrm{r} \\ 0 & , \quad \text{else.} \end{cases}$$

Basically, we assume a transducer with a mid-band frequency $f = 2\pi\omega$ and model f_m. This yields the transducer specific harmonic displacement field in Equation (15) for a bandwidth $f_\mathrm{l} < f < f_\mathrm{r}$. Figure 6 shows the variety of frequencies we use in the following virtual experiments.

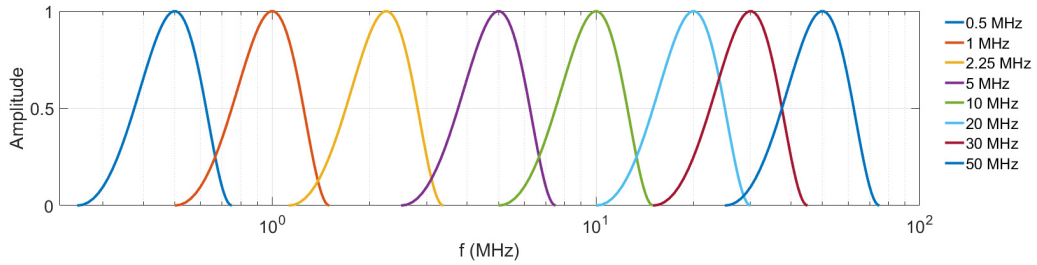

Figure 6. Simulated frequency bandwidth with left bound $f_\mathrm{l} = 0.5f$ and right bound $f_\mathrm{r} = 1.5f$.

In the virtual experiments, we assume the ultrasonic transducer in pulse-echo technique emitting and receiving pressure wave, which mimics varying mid-band frequencies. Finally, we transform the result into the time domain by MATLAB's inverse Fast Fourier Transform (FFT) [69,70].

2.3.3. Evaluation Tools

A microstructure model fit yields a predefined number of microstructure realizations (cell systems) [5,52]. We aim at simulating ultrasonic specifics in these cell systems, as scattering. In ultrasonic testing, scattering regimes are roughly characterized in terms of the testing frequency f, the material dependent wave propagation velocity v_α, and the effective scatterer diameter d_eff, as follows [8]:

- *the low-frequency Rayleigh regime* $\frac{\pi f}{v_\alpha} d_\mathrm{eff} \ll 1$,
- *the stochastic regime* $\frac{\pi f}{v_\alpha} d_\mathrm{eff} \leq 1$ and
- *the high-frequency geometric limit* $\frac{\pi f}{v_\alpha} d_\mathrm{eff} > 1$.

We use the Born approximation to compute backscattered wave contributions, valid in the low-frequency Rayleigh regime [13]. Accordingly, we set an upper fixed boundary for the Rayleigh regime at 0.3, which yields

$$d_\mathrm{eff} = 0.3 \frac{v_\alpha}{\pi f}. \tag{16}$$

By this, we assume that scatterers' size remains within the Rayleigh regime and the modeled scattering contributions are reasonable. Equation (16) corresponds to the hypothetical boundary below which the cell's diameter stays in the Rayleigh scattering regime. We

denote this boundary by b_R and check whether the microstructure realizations observe this boundary.

3. Materials

We calculate the microstructural scattering for two metals—Inconel-617 and titanium. The first is represented by 2D micrographs, only, whereas for the latter three-dimensional diffraction computed tomography (DCT) data is available. The Inconel-617 alloy features coarse grains with average 2D diameter 185 µm whereas the titanium's microstructure is much finer with just 33 µm. We extract random 2D slices along all three spatial directions from the DCT data and compute the average of observed grain 2D diameters for this particular comparison.

3.1. Computation Environment

First, we describe the environment used for the computations. According to the workflow sketched in Figure 2, we choose the number of realizations of the stochastic microstructure model. These can be generated in parallel. The tessellations are generated on a machine with eight CPUs and 16 GB RAM.

The computation of the wave fields with and without microstructural scattering, is the most time consuming step due to the high testing frequencies. These induce very fine discretizations of the transducer surface and of the frequency bandwidth of the transducer. Small grains increase the number of cells per considered volume and thus increase the computation time, too.

The loop has to be traversed three times in order to cover all dependencies: The backscattering contributions for each frequency step (bandwidth), each of the spatially arranged scatterers, and all discretization points of the transducer. For these steps, in particular the ω-loop (red box in Figure 2), a C++ parallelization using openmp [71,72] is executed on nodes with 16 CPUs and 60 GB RAM of Fraunhofer ITWM's linux cluster [73].

3.2. Inconel-617

Inconel is the trade name for a group of nickel-chromium alloys with exceptional strength, metallurgical stability, and oxidation resistance at high temperatures [74]. Inconel alloys are therefore used e. g. in aerospace solutions, in gas turbines for combustion cans, as well as for petrochemical processing and heat-treatment equipment. Here, we analyze a macroscopically homogeneous sample of this alloy and treat its microstructure as a single phase. Microstructural information is provided by a stack of micrographs featuring bright grains separated by dark grain boundaries, see Figure 7.

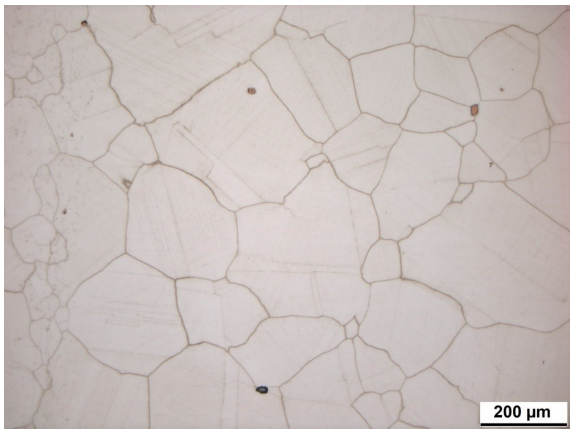

Figure 7. Micrograph of the Inconel-617 under investigation, cell boundaries are emphasized by etching. Micrographs from [32] courtesy of Thomas Schwender (Fraunhofer IZFP).

Based on these micrographs, the maximal Feret diameters of the cells were determined, only, due to the notorious cell boundary reconstruction problem. In [32], isotropy of the

microstructure is deduced from the analysis of micrographs from three pairwise orthogonal cutting planes. We observe altogether 666 cells in 64.5 mm^2 yielding a 2D cell density of $N_A = 10.3\ mm^{-2}$ for the Inconel-617 alloy. The mean maximal Feret diameter of the 2D grain sections is $d_{\text{Feret}} = 185\ \mu m$. About a third of the observed 2D grain sections are larger than 200 µm, with the maximum even exceeding 700 µm. This emphasizes the coarse grain structure of the Inconel-617.

3.3. Titanium

The second material we consider is a titanium. Microstructural information is acquired by DCT [75] at Beamline ID11 of the European Synchrotron Radiation Facility (ESRF), courtesy of Wolfgang Ludwig. DCT is a full-field X-ray microscopy technique deploying synchrotron radiation and imaging spatially the grains and their crystallographic orientation. More precisely, the reconstruction provides labeled 3D image data where each voxel's gray value is the number of the grain it is contained in as well as the full 3D orientation of each of these grains. For details see [75,76]. The imaged cylindrical sample has a diameter of 518 µm, is 400 µm high, and contains 1397 grains. See Figure 8 for renderings of the complete data set and a small cluster of grains.

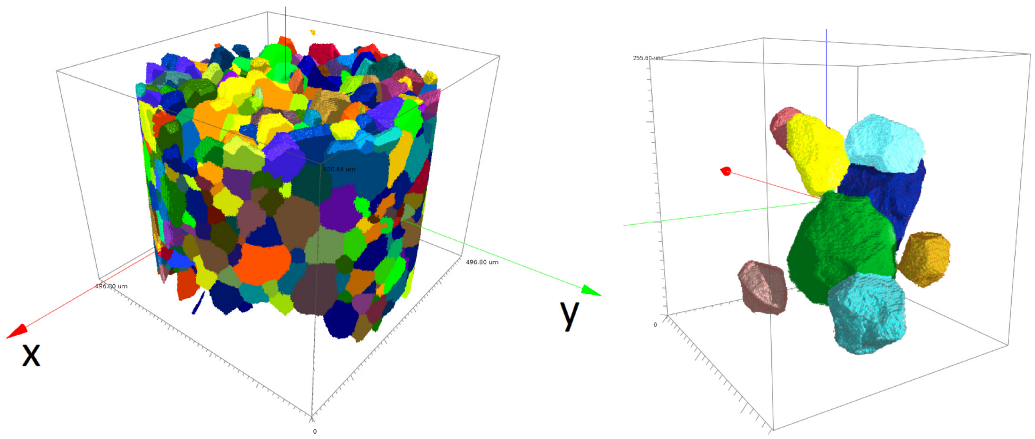

(**a**) Complete data set (**b**) Cluster of grains

Figure 8. Rendering of the DCT image data of the titanium sample. The imaged cylinder has a diameter of 518 µm and a height of 400 µm. In (**a**), boundary grains on top and bottom are removed to emphasize the shape and packing of grains. Subfigure (**b**) shows a cluster of grains from this data set. The grain colors are randomly chosen in order to visually separate neighboring grains and their shapes.

As grains are separated in the 3D image already, no further image processing is required, and grain shape and volume can be analyzed directly. Mean and standard deviation of the grain volumes are $4.96 \cdot 10^{-5}\ mm^3$ and $9.27 \cdot 10^{-5}\ mm^3$, respectively.

4. Results

The following subsections yield simulation results for the two alloys and corresponding microstructure model realizations.

4.1. Inconel-617

We first fit the microstructure model by determining the cell density and the cell volume coefficient of variation based on the 2D micrographs by the method described in Section 2.2.3. Subsequently, we generate an enlarged volume for computing the ultrasonic scattering.

4.1.1. Microstructure Model

Grain volumes are assumed to be log-normally distributed. As reported in Section 3.2 above, we observe a grain density of $N_A = 10.3\ \mathrm{mm}^{-2}$ in the 2D micrographs of the Inconel. Equation (11) then yields the spatial grain density $N_V = 18.80\ \mathrm{mm}^{-3}$, which in turn yields 1128 cells in a volume of 60 mm^3. We therefore start with a first guess of 1200 cells.

We set the variation coefficient of the sphere volumes to an initial value of $\mathrm{cv_s} = 1.5$, draw a sample of 1200 spheres from the log normal distribution according to Equation (10), and pack them densely to obtain a volume fraction of 60 %. The corresponding 3D Laguerre tessellation is computed and scaled to the sample volume. Planar slices are extracted and analyzed, see Figure 9. To save computing time, we increase the number of cells by the rather high number of 200 per step.

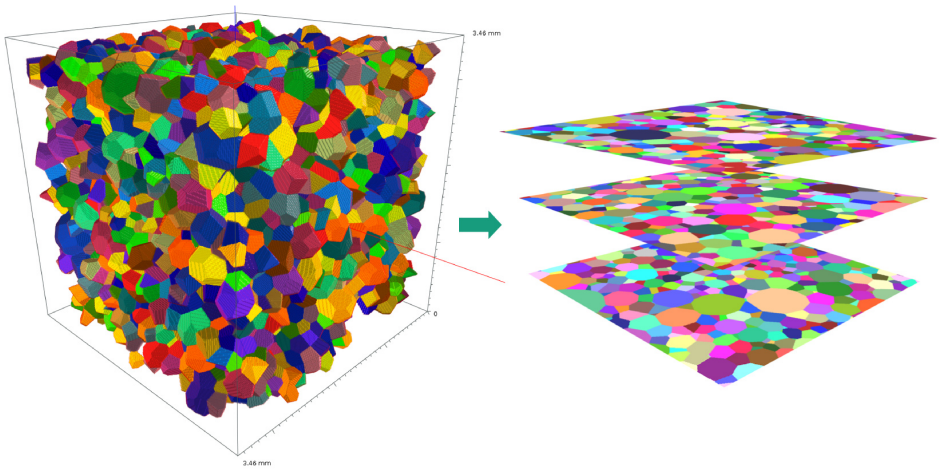

Figure 9. Visualization of the model fit for the Inconel-617. **Left**: Rendering of a realization of the random Laguerre tessellation with overall 2000 cells in a cube of edge length 3.91 mm, and volume 60 mm^3. **Right**: 2D sections compared with the micrographs. The cells are visualized by false color mapping.

The realization of the fitted Laguerre tessellation comprises 2000 cells. The mean maximal Feret diameter in the 2D slices is 185 µm. For fitting now also the grain volume coefficient of variation $\mathrm{cv_g}$ (see Section 2.2.2), we first choose the sphere volume coefficient of variation $\mathrm{cv_s}$ (see Section 2.2.3) by a grid search. More precisely, we choose $\mathrm{cv_s}$ in the interval $[1.0, 3.6]$ and vary it with step size 0.1.

The best fit of the derived Laguerre tessellation is reached for the rather high value of $\mathrm{cv_s} = 3.5$. The corresponding Laguerre tessellation has mean 3D cell diameter $\bar{d}_{\mathrm{cell}} = 329$ µm and $\mathrm{cv_g} = 2.15$. One of the original micrographs and a rendering of the Laguerre model realization are shown in Figure 10. Figure 11 depicts the corresponding histogram of cells' maximal Ferret diameter.

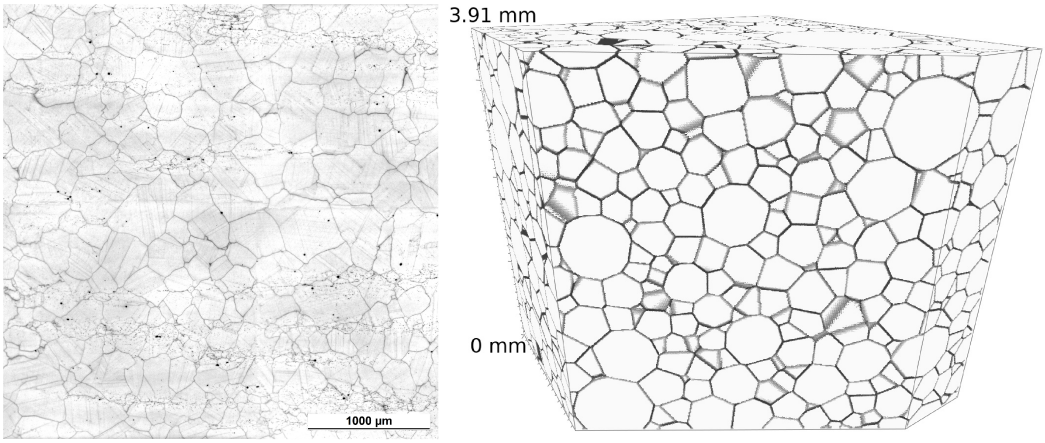

Figure 10. One of the original micrographs of the Inconel-617 and a rendering of a realization of the fitted Laguerre tessellation model with $\mathrm{cv_s} = 3.5$ and 2000 cells.

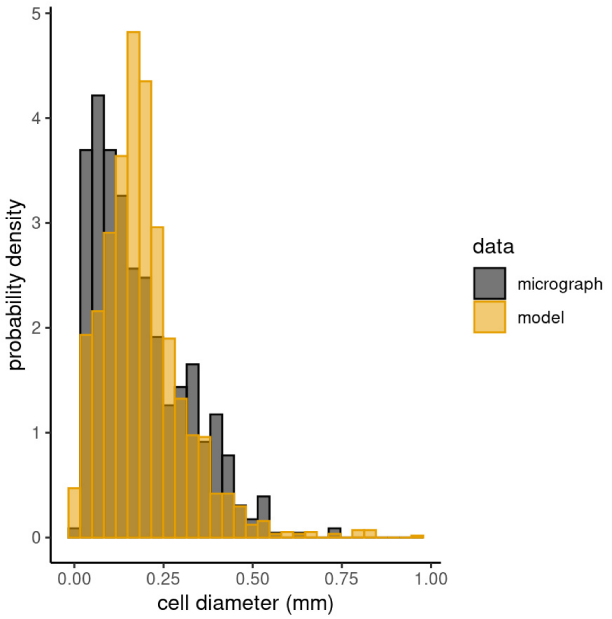

Figure 11. Histograms of maximal Feret diameters measured in the micrographs of the Inconel-617 and in 2D sections of realizations of the fitted Laguerre tessellation model with ($\mathrm{cv_s} = 3.5$ and 2000 cells) slices.

4.1.2. Model Based Scattering Investigation in Inconel-617

We generate now 10 realizations of the fitted model in a significantly enlarged volume of $V = (7.83\,\mathrm{mm})^3 = 480\,\mathrm{mm}^3$ instead of the 60 mm^3 considered so far. We double the dimension along each spatial directions to get $N = 16\,000$ expected cells. Table 3 summarizes modeled microstructure. The effective diameters $d_{\mathrm{eff}}(C_i)$ of cells $i = 1, \ldots, N$ as defined in Section 2.1.1 vary with the realization of the fitted model, as do the numbers of cells, see Table 3.

Table 3. Summary of the Inconel-617 microstructure model ($cv_s = 3.5$ and 16,000 cells) realizations.

Realization Nr.	$\underset{i}{\mathbf{std}}(V_{\mathbf{eff}}(C_i))$ $(\mathbf{mm^3})$	$\underset{i}{\mathbf{min}}(d_{\mathbf{eff}}(C_i))$ $(\boldsymbol{\mu}\mathbf{m})$	$\underset{i}{\mathbf{max}}(d_{\mathbf{eff}}(C_i))$ $(\boldsymbol{\mu}\mathbf{m})$
1	0.0715	62	1039
2	0.0739	64	1131
3	0.0693	45	967
4	0.0693	57	1002
5	0.0723	60	1032
6	0.0701	62	896
7	0.0684	59	956
8	0.0729	59	1137
9	0.0669	61	860
10	0.0656	56	1099
mean	0.0700	58.5	1011

Figure 12 also emphasizes the variation of the realizations. The boxplots are to be read as follows: The box includes 50% of cell's diameters, lower and upper boundaries represent the 25th and 75th percentiles, respectively, the central horizontal line the mean value, and whiskers capture the remaining cells. More important, Figure 12 shows where the cell sizes exceed the Rayleigh boundary b_R. In particular, Figure 12 reveals that e.g., testing frequency 5 MHz, is not an appropriate choice for the analyzed Inconel-617.

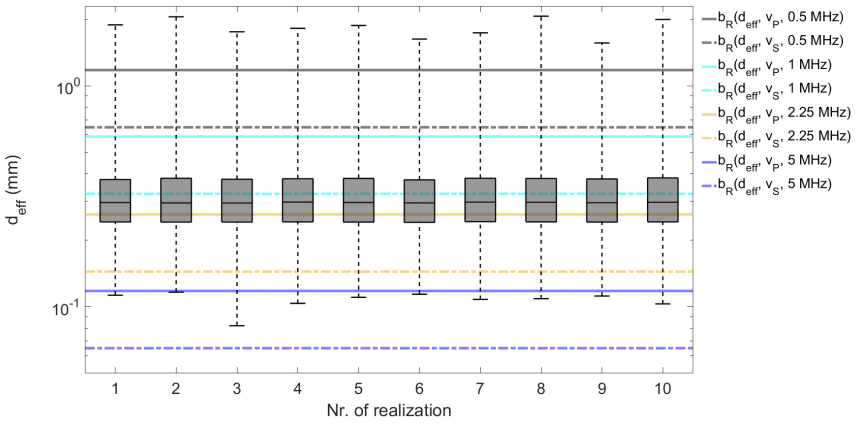

Figure 12. Effective cell diameters in ten realizations of the Inconel-617 microstructure model. The solid and dashed horizontal lines correspond to the upper boundaries of the Rayleigh regime for the pressure and shear waves, respectively. Colors code the frequency, see legend. Clearly, the Rayleigh regime is violated in the 5 MHz case.

Figure 13 shows the spatial scattering function for a single scatterer with mean diameter $d_{\text{eff}} = 329$ µm and the crystallographic structure of Inconel-617. We assume an elastic wave propagating from top to bottom, which corresponds to the direction of the local coordinate system's positive z-axis. The general shape of the spatial scattering functions remains similar, the local minima and maxima of the backscattering coefficient do not change. The ratio however changes from forward to backward scattered contribution. The frequency of the incoming longitudinal waves is set to 0.5 and 2.25 MHz, below and above the Rayleigh boundary according to Equation (16). Note the scale difference of three magnitudes for the spatial scattering functions w.r.t. testing frequency in Figure 13a,b.

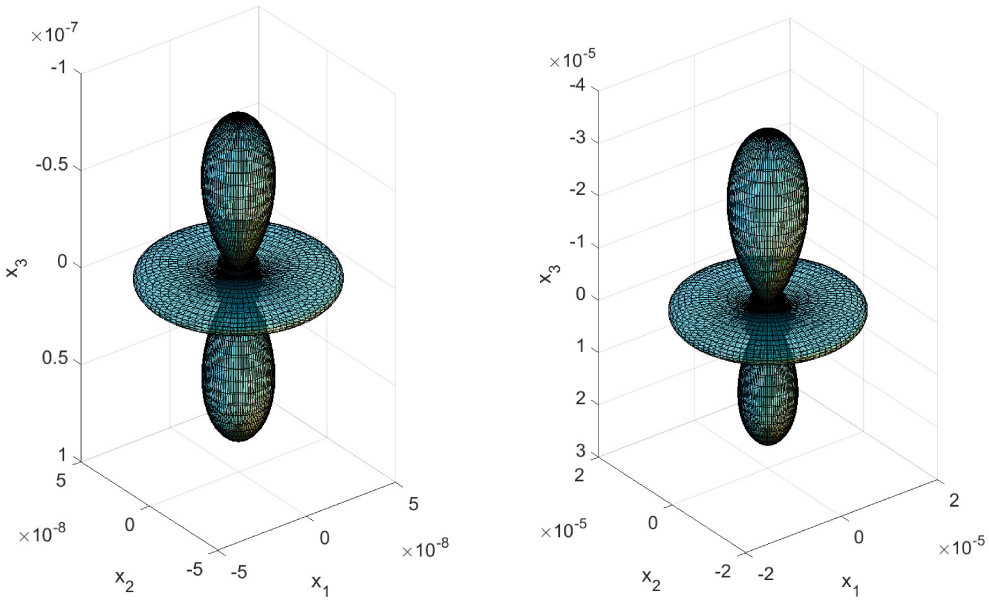

(**a**) $\eta_{\mathrm{P}\to\mathrm{P}}(\vartheta, \varphi, 2\pi\, 0.5\,\mathrm{MHz})$ (**b**) $\eta_{\mathrm{P}\to\mathrm{P}}(\vartheta, \varphi, 2\pi\, 2.25\,\mathrm{MHz})$

Figure 13. Spatial scattering function $\eta_{\mathrm{P}\to\mathrm{P}}(\vartheta, \varphi, 2\pi f)$ (in mm^{-3}) for a single scatterer of size $d_{\mathrm{eff}} = 329$ µm, testing frequency (**a**) $f = 0.5$ MHz, $d_{\mathrm{eff}}\pi f/v_{\alpha} = 0.15$ and (**b**) $f = 2.25$ MHz, $d_{\mathrm{eff}}\pi f/v_{\alpha} = 0.68$, respectively. Thus, according to Equation (16), for $f = 2.25$, we are in the stochastic regime.

We compute the time-domain signals by simulating a frequency bandwidth as described in Section 2.3.2, in particular Figure 6. Figure 14 shows the backscattered time-domain signals for the 10 microstructure realizations of the Inconel-617 and assuming this alloy's characteristics. Contributions of every discrete transducer point being the source points are collected, see Equation (12). The modeled transducer mimics a longitudinal transceiver probe with a diameter of 6 mm for all frequencies. The signal is normalized, which means it is divided by the number of source points. In Figure 14, the covered distance corresponds to 25 times the double depth of the considered volume, i.e., 391.4 mm. These figures emphasize the amplitude variation introduced by microstructural variation. The backscattered signal has a significantly larger amplitude at 5 MHz with a difference of 10^{-13} to 10^{-16}. Each microstructure realization leads to a time-domain signal as shown in Figure 14.

4.2. Titanium

Here, we present the results for the titanium. The modelling approach is simpler here as 3D microstructure data are available.

4.2.1. Model Fit

The mean and standard deviation of the grain volumes are used to fit the Laguerre tessellation model. The mean and standard deviation reported in Section 3.3 yield the coefficient of variation $\mathrm{cv_g} = 1.86$ for the volume of grains. We use the quadratic polynomial from [5] to estimate the coefficient of variation for the sphere packing $\mathrm{cv_s} = 2.34$. The grain number density is 20,146 mm^{-3}. Figure 15a shows the empirical grain volume distributions observed in the DCT image data and in realizations of the fitted model.

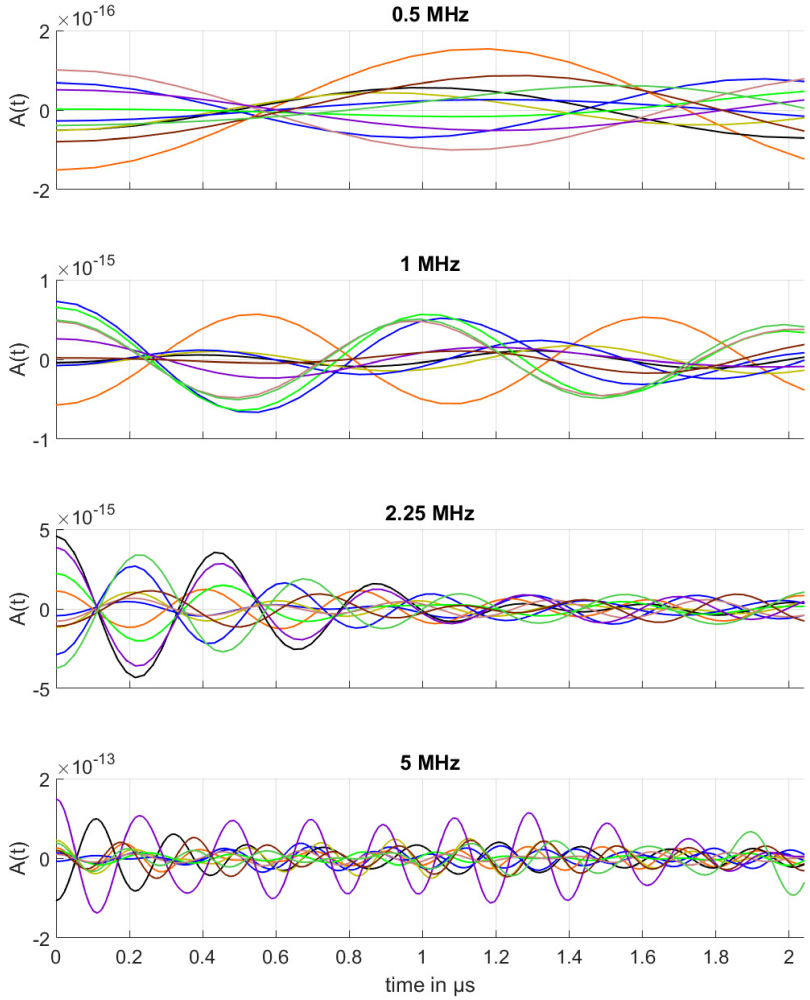

Figure 14. Backscattered signals (indicated by ten arbitrary colors) for a sequence of testing frequencies $f = 0.5$, 1, 2.25, and 5 MHz. The corresponding transducer is modeled by a circle with radius 3 mm, which emits and receives longitudinal waves.

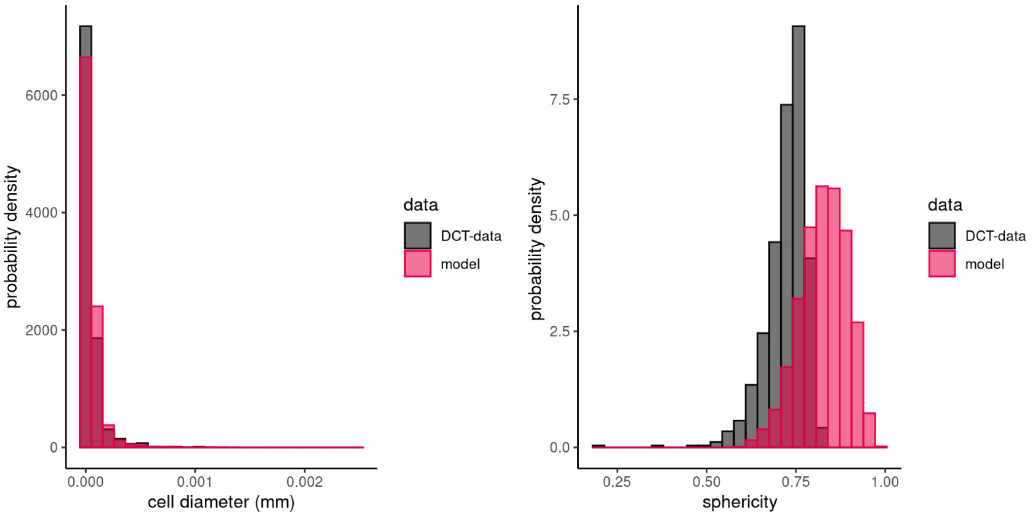

(**a**) grains and cells volume distribution (**b**) grain and cell sphericity distribution

Figure 15. Histograms of the grain volumes of the titanium sample and realizations of the model fitted to it ($cv_s = 2.34$).

We enlarge the volume eightfold, doubling the edge length in each of the three spatial directions. This yields the expected number of cells $N = 0.860\,\mathrm{mm}^3\, 20{,}146\,\mathrm{mm}^{-3} = 17{,}344$ in a cube of edge length 0.95 mm. Next, we determine the parameters of the log-normal distribution of sphere volumes—$\mu = -11.2$ and $\sigma = 1.3$. We generate again ten realizations of the stochastic model, see Table 4. The mean effective diameter of the cells in the derived tessellations is 36.4 µm.

To validate the model, we compare the distributions of the sphericity (6) of the observed titanium grains and the simulated cells, see Figure 15b. The Laguerre tesellation cells tend to be more spherical than the real grains. This is not surprising. On the one hand, cells from Laguerre tessellations generated by densely packed spheres are convex and with high coefficient of variation tend to be regular, meaning more spherical [52]. On the other hand, in the DCT data, we find also non-convex grains featuring rough surfaces, see Figure 16 for an example. Non-convex cell shapes can be captured e.g., by generalized balanced power diagrams [15,19]. However, this is beyond the scope of this contribution.

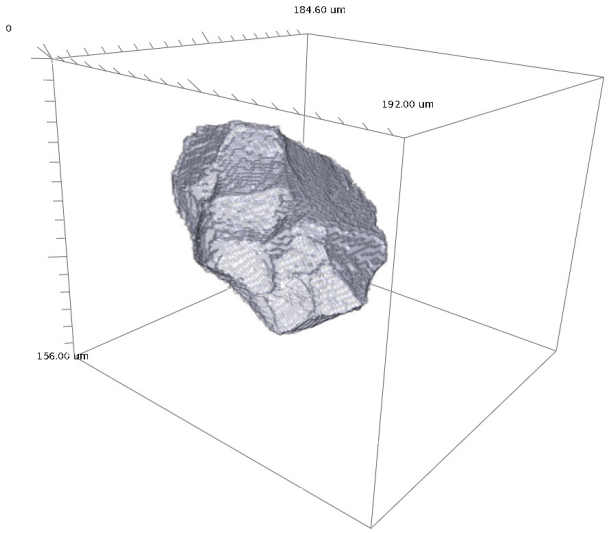

Figure 16. Rendering of a non-convex grain observed in the DCT data of the titanium sample.

Table 4. Results for the titanium model realizations ($cv_s = 2.34$ and 17,344 cells).

Nr.	$\underset{i}{\mathbf{std}}(C_i)$ in $10^4(\mu m^3)$	$\min_i(d_{\mathrm{eff}}(C_i))$ (µm)	$\max_i(d_{\mathrm{eff}}(C_i))$ (µm)
1	5.540	5	79
2	5.607	7	81
3	5.888	7	83
4	6.426	7	108
5	5.908	7	88
6	5.615	6	81
7	6.509	7	112
8	6.496	7	104
9	5.922	7	91
10	5.897	7	81
mean	5.980	6.7	90.8

4.2.2. Model Based Scattering Investigation in Titanium

Figure 17 illustrates, how much the realizations vary. The distribution's overall shape is very similar in the ten realizations, but the minimum and maximum values are less representative for the distribution. Figure 17 shows also, where cell sizes exceeding the Rayleigh boundary occur. For example b_R, in particular for testing frequency 50 MHz, shows that this frequency is a bad choice for this titanium alloy.

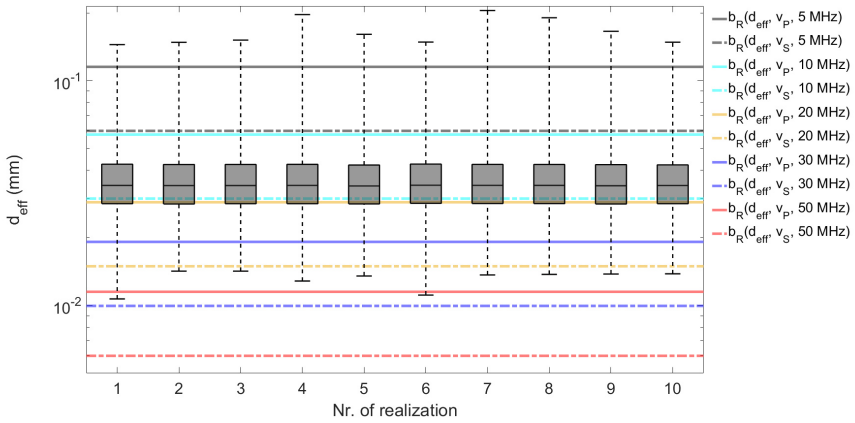

Figure 17. Effective cell diameters in ten realizations of the microstructure model for the titanium. Clearly, the Rayleigh regime is violated in the 50 MHz case.

Figure 18 shows this difference as spatial scattering function for the mean effective grain diameter (d_{eff} = 36.4 µm) for two frequencies. The scattering coefficients increase significantly for frequency 30 MHz, by at least two orders of magnitude. Note, that the chosen two frequencies (5 MHz in Figure 18a and 30 MHz in Figure 18b) represent different scattering regimes assuming the same effective grain diameter. Figure 18a represents scattering clearly in the Rayleigh regime with characteristic value kr_{eff} = 0.09, generated by the frequency of 5 MHz, corresponding to wavelength 1.2 mm. In Figure 18b, for the frequency of 30 MHz corresponding to wavelength 0.2 mm, the characteristic value is kr_{eff} = 0.57, indicating scattering beyond the Rayleigh boundary.

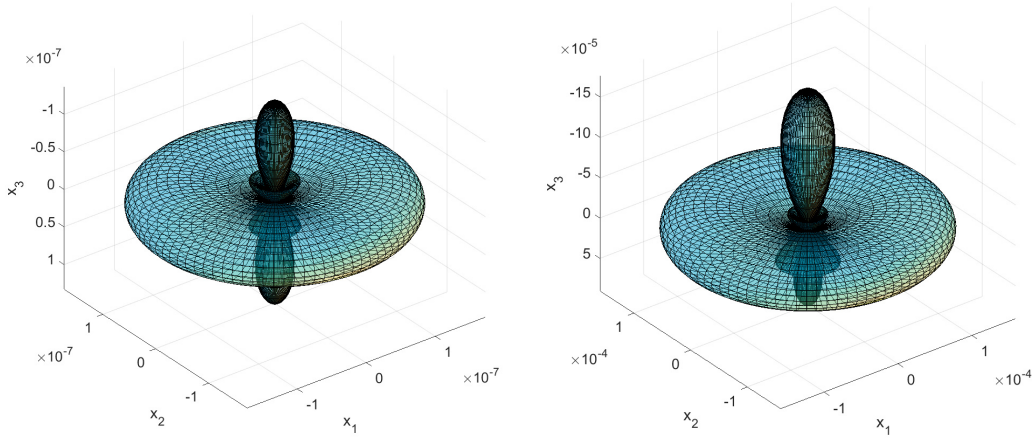

(**a**) $\eta_{\mathrm{P}\to\mathrm{P}}(\varphi, \vartheta, 2\pi\,5\,\mathrm{MHz})$ (**b**) $\eta_{\mathrm{P}\to\mathrm{P}}(\varphi, \vartheta, 2\pi\,30\,\mathrm{MHz})$

Figure 18. Spatial scattering function $\eta_{\mathrm{P}\to\mathrm{P}}(\varphi, \vartheta, 2\pi f)$ (in mm^{-3}) for a single scatterer size $d_{\mathrm{eff}} = 36.4\,\mu\mathrm{m}$, testing frequency (**a**) $f = 5$ MHz, $d_{\mathrm{eff}}\pi f / v_\alpha = 0.09$ and (**b**) $f = 30$ MHz, $d_{\mathrm{eff}}\pi f / v_\alpha = 0.57$, respectively. Thus, according to Equation (16), for $f = 30$ we are in the stochastic regime.

Next, we compute the time-domain signals as described in Section 2.3. The corresponding bandwidths are depicted in Figure 6. The transducer mimics a longitudinal probe with a diameter of 6 mm for frequencies 5, 10, 20, and 30 MHz. The circular transducer emitting the wave at 50 MHz frequency is modeled with a diameter of 3 mm. Figure 19 shows the simulated backscattered time-domain signals. As expected, the amplitude grows with increasing frequency. The computed signals cover 25 times double depth of the considered volume, that is 43 mm.

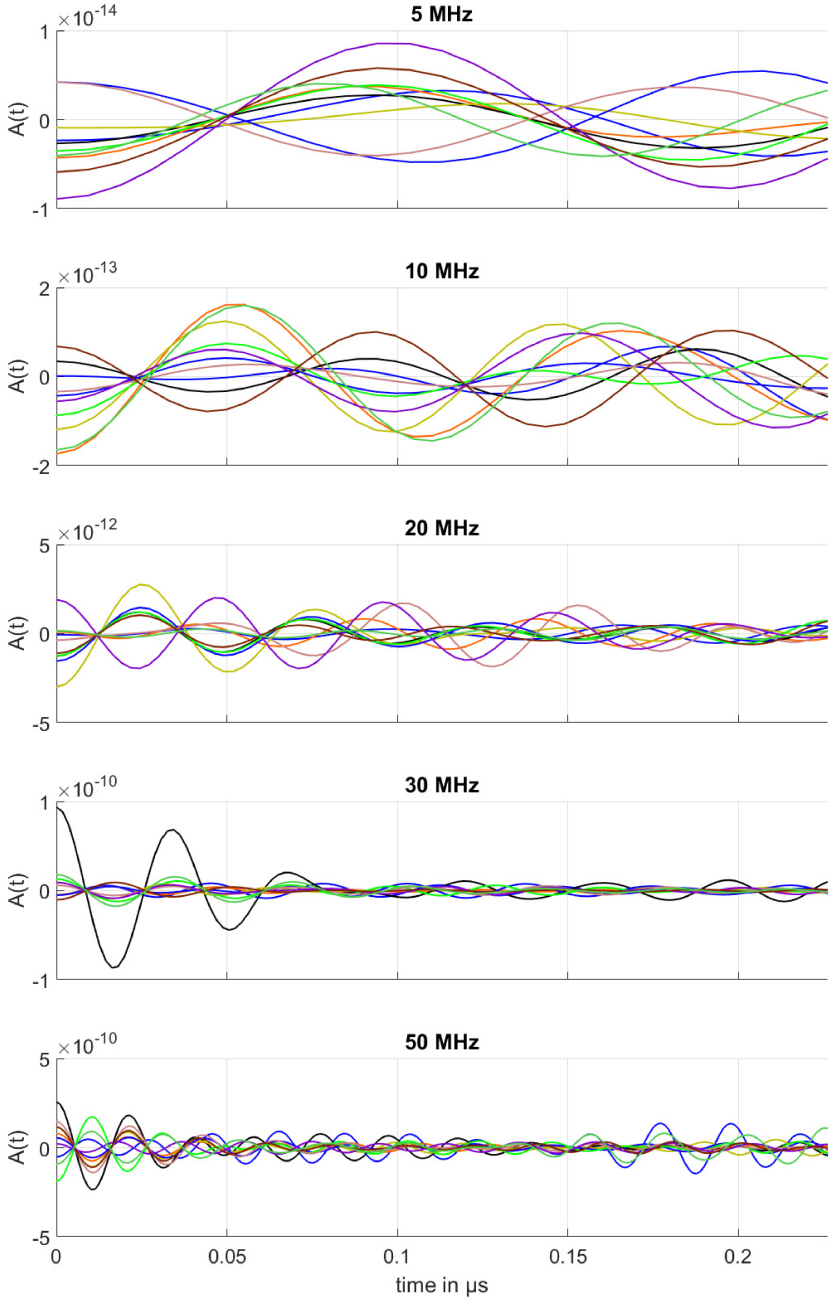

Figure 19. Received backscattered signals in titanium for a sequence of testing frequencies $f = 5$, 10, 20, 30 and 50 MHz. The corresponding transducer is modeled as a circle with diameters 3 mm for frequency 50 MHz and 6 mm for all other frequencies, which emits and receives longitudinal waves.

4.3. Summary

We summarize here the achieved results. In both applications—Inconel-617 and titanium—model fitting based on 2D and 3D image data, generating the dense sphere packings consumes most computation time.

The spatial scattering function varies with testing frequency, incoming and scattered wave modes with their respective propagation characteristics, and additionally the material dependent parameters as effective grain diameter, elastic constants, and material density. The range of the backscattering coefficients varies, too, and is largest for $\eta_{S\to S}$. The general shape of spatial scattering function stays similar for the cubic and hexagonal crystal systems considered here (see Table 1 and Figures 3, 13 and 18), respectively. Distinctive points are aligned for cubic and hexagonal crystallographic structures along the x_1, x_2, x_3 axes or the spatial diagonals in the local coordinate system, respectively. The scattering coefficient graphs are symmetric w.r.t. the propagation direction of the incoming longitudinal wave and both scattered waves, i.e., $\eta_{P\to P}$ and $\eta_{S\to P}$, for cubic crystallized systems.

Regarding the scattering theory, an insight is that the scattering coefficients form a closed shape which we call a spatial scattering function. That fact might be interesting for other applications where the goal is the reconstruction of 3D ultrasonic signals. Also, the spatial scattering function might play a role in development of multiple scattering approaches, in the future. The direction dependent scattering contributions can be incorporated in signal analysis in order to reduce the present noise level introduced by local microstructure. Of course, this approach requires the knowledge about the alloy's structure, i.e., the phases with their microstructural features. Anyhow, the scattering contributions of incident and scattered waves are more pronounced in certain spatial directions [7], which our analytical results confirm. The spatial scattering function might be exploited in order to analyze the directivity's maxima/minima. This insight allows for prediction of spatial directions which are more prone or robust w.r.t. microstructural scattering in average.

The simulated backscattered time-domain signals are consistent if we compare the change of frequency's magnitude and the backscattered signal's one. A change by one magnitude of frequency—0.5 to 5 MHz for Inconel-617, and 5 to 50 MHz for titanium—increases backscattering by three to four magnitudes. Figures 14 and 19 reveal strong variation of the backscattered signals in both, phase shift and amplitude, for the same testing frequency. Moreover, some microstructure realizations lead to a prominent backscattering contribution for distinct frequencies. For the Inconel-617 (Figure 14), the violet and black marked time-domain signals yield significantly stronger backscattering for 2.25 and 5 MHz compared to 1 MHz. For the titanium (Figure 19), the black time-domain signal behaves similarly for 30 and 50 MHz compared to the lower frequencies.

5. Discussion

We describe here a method for simulating backscattered wave contributions caused by the microstructure of the polycrystal in which the wave propagates. In contrast to previous studies, we fit a microstructure model to image data of real polycrystals. We study two polycrystals—Inconel-617 and titanium—differing significantly in grain size and crystallographic structure. The microstructures of both, the coarse-grained cubic Inconel-617 and the fine-grained hexagonal titanium, are modeled by Laguerre tessellations generated by sphere packings.

Model fitting consists of choosing mean and coefficient of variation of the sphere volumes to meet the observed structures. This is comparably easy in the case where full 3D information from X-ray DCT or 3D EBSD is available. However, the use of these imaging techniques is still rather an exception while 2D micrographs are well-established and accessible in quality assurance labs. For fitting models based on 2D images, parameters have to be determined by systematically testing candidate values within a reasonable search interval as described in Section 2.2.3. This is costly as many realizations of 3D models have to be generated.

Our spatial scattering function yields grainwise backscattered contributions. This is the main difference to the analytical scattering theory from [13] predicting backscattering as function of mean grain diameter. Instead, we reveal how a cell system with a certain diameter distribution interacts with waves of varying frequencies. To this end, we simulate a set of time-domain signals.

Our simulations rely on the Born approximation assuming an isotropic grain structure. Inconel and titanium often feature a strongly anisotropic one. Thus, the Born approximation can cause a potentially large error. However, the samples considered here are only mildly anisotropic. Incorporating the anisotropy due to grain shape as well as anisotropy due to crystallographic orientation properly is nevertheless subject of further research.

This work is motivated by the need for simulation techniques for ultrasonic wave propagation including grain noise. Our method is theoretically well described, has however not been validated by real experiments. To enable exactly this comparison, further work is needed. To compare our simulation results to the experimental ones of [77,78] for titanium, a modelling of microstructure with elongated grains is needed. For Inconel [32] , the virtual experiment has to be extended by a reflection at a back wall of the sample. The major obstacle is however the need for a microstructure model realization covering at least three centimeters in each coordinate direction. This demands a tessellation with about one million cells, 64 times larger than the current model realization with 16,000 cells. Thus, the computations would take days if not even weeks. Finally, to allow for proper estimation of detection probabilities, defect echos have to be simulated and compared to measured ultrasonic signals.

Another point deserving further investigation is, how representative the simulated ultrasonic signals are. The microstructures are modeled by random tessellations. Thus, the realizations have to include enough cells to satisfy the law of large numbers for cell statistics. This condition is well satisfied with altogether more than 100,000 cells in each of the two model fits. However, we simulate just ten time-domain signals for each material. This might not be sufficient to capture the variability of the ultrasonic signal.

We build on [13], where the grains are approximated as closely packed spherical scatterers accounting for just single backscattered contributions. The scatterer's shapes and orientations are thus ignored for the moment. The effect of the shapes might however be non-negligible, in particular for coarse granular microstructures. We assume the grains to be Laguerre tessellation cells, thus convex polytopes. The 3D DCT data of the titanium nevertheless reveals non-convex grains. More elaborate models for polycrystalline microstructures allowing for non-convex cells and curved grain boundaries have been developed [14–21]. These could be used for ultrasonic simulation, too. The DCT data also yields the crystallographic grain orientations. In order to exploit this structural information in the ultrasonic simulations, the spatial scattering functions need to be reformulated. In particular, the correlation function would have to account for eventually observed grain orientation correlations.

This paper is one step forward towards simulation of realistic grain noise in ultrasonic testing. Many more—most prominent considerable enlargement of the microstructure model realizations, incorporation of grain orientations, simulation of multiple scattering—wait to be conquered before simulated and experimental results can be compared quantitatively.

6. Conclusions

Ultrasonic testing is a popular, indispensable non-destructive testing technique. Its proper use relies heavily on simulations in order to interpret the received signals correctly. Simulation of ultrasonic wave propagation is therefore a vivid field of research.

This work focuses on polycrystalline materials and a method to account for the so-called grain noise caused by scattering of the propagating wave by the grain boundaries. Building on [13], we simulate backscattered wave contributions of the individual grains forming the polycrystal. To this end, the grain structure is modeled by a Laguerre tessellation model. Compared to the Voronoi tessellation used in previous attempts, using

this more versatile type of model increases the effort for microstructure modelling considerably, enables however to capture the real grain size distribution much better. This is demonstrated here for two real metal alloy samples.

As discussed in Section 5 above, the method presented here needs generalizations in many ways before yielding simulated ultrasound signals that can be quantitatively compared to measured ones. We see it rather as a door opener towards realistic microstructure modeling in ultrasound simulation. We nevertheless achieved practically valuable results, too. In particular, the explicit relation of testing frequency, cell sizes, and Rayleigh boundary derived in Sections 4.1.2 and 4.2.2. The spatial scattering functions and their shapes as shown in Figures 13 and 18 shed a new light on the structure signal interaction and thus are of value on their own, too.

To summarize, we combined Hirsekorn's [13] single scattering theory with explicit microstructure modeling using Laguerre tessellations to make considerable progress on the way to realistic grain noise simulation in ultrasonic testing.

Author Contributions: Conceptualization, D.D. and K.S.; methodology, D.D. and K.S.; software, D.D.; validation, D.D., K.S.; formal analysis, K.S.; investigation, D.D.; resources, D.D and K.S..; data curation, D.D.; writing–original draft preparation, D.D. and K.S.; writing–review and editing, D.D. and K.S.; visualization, D.D.; supervision, K.S.; project administration, D.D.; funding acquisition, D.D. All authors have read and agreed to the published version of the manuscript.

Funding: This project has been partially supported by the German Federal Ministry of Education and Research (BMBF) under grant 05M2013 (AniS) and 05M13RCA (AMSCHA). Also, Fraunhofer Society and DGZfP e.V. supported D.D. by scholarships.

Institutional Review Board Statement: Not applicable.

Informed Consent Statement: Not applicable.

Data Availability Statement: The data can be accessed on demand from the author.

Acknowledgments: The authors thank kindly Thomas Schwender at Fraunhofer Institute for Nondestructive Testing IZFP and Wolfgang Ludwig at European Synchrotron Radiation Facility ESRF for sharing the real microstructure data and making this investigation possible. We thank Claudia Redenbach and Joachim Ohser for helpful discussions and comments and Michael Godehardt for software solutions.

Conflicts of Interest: The authors declare no conflict of interest. The funders had no role in the design of the study; in the collection, analyses, or interpretation of data; in the writing of the manuscript, or in the decision to publish the results.

Abbreviations

The following abbreviations are used in this manuscript:

FFT	Fast Fourier Transformation
DCT	Diffraction Contrast Tomography
ESRF	European Synchrotron Radiation Facility

References

1. Gros, X. *NDT Data Fusion*; Knovel Library: London, UK, 1997.
2. Spies, M.; Rieder, H.; Rauhut, M.; Kreier, P.; Innotest, A. Surface, Near-Surface and Volume Inspection of Cast Components Using Complementary NDT Approaches. In Proceedings of the 19th World Conference on Non-Destructive Testing 2016, Munich, Germany, 13–17 June 2016 .
3. Ashcroft, N.W.; Mermin, N.D. *Festkörperphysik*; De Gruyter: Berlin, Germany, 2001.
4. Okazaki, K.; Conrad, H. Grain size distribution in recrystallized alpha-titanium. *Trans. Jpn. Inst. Met.* **1972**, *13*, 198–204. [CrossRef]
5. Fan, Z.; Wu, Y.; Zhao, X.; Lu, Y. Simulation of polycrystalline structure with Voronoi diagram in Laguerre geometry based on random closed packing of spheres. *Comput. Mater. Sci.* **2004**, *29*, 301–308. [CrossRef]
6. Mason, W.P.; McSkimin, H. Attenuation and scattering of high frequency sound waves in metals and glasses. *J. Acoust. Soc. Am.* **1947**, *19*, 464–473. [CrossRef]

7. Truell, R.; Elbaum, C.; Chick, B.B. *Ultrasonic Methods in Solid State Physics*; Academic Press: New York, NY, USA, 1969.
8. Stanke, F.E.; Kino, G. A unified theory for elastic wave propagation in polycrystalline materials. *J. Acoust. Soc. Am.* **1984**, *75*, 665–681. [CrossRef]
9. Ishimaru, A. *Wave Propagation and Scattering in Random Media*; Academic Press: New York, NY, USA, 1978; Volume 1–2.
10. Rose, J.H. Ultrasonic backscatter from microstructure. *Rev. Prog. Quant. Nondestruct. Eval. Vol. 11B* **1992**, *11*, 1677–1684.
11. Dorval, V.; Jenson, F.; Corneloup, G.; Moysan, J. Accounting for structural noise and attenuation in the modeling of the ultrasonic testing of polycrystalline materials. In Proceedings of the AIP Conference Proceedings, Penang, Malaysia, 21–23 December 2010; Volume 1211, pp. 1309–1316.
12. Ganjehi, L.; Dorval, V.; Jenson, F. Modelling of the ultrasonic propagation in polycrystalline materials. *Acoustics* **2012**, *2012*, 2621–2626.
13. Hirsekorn, S. Theoretical description of ultrasonic propagation and scattering phenomena in polycrystalline structures aiming for simulations on nondestructive materials characterization and defect detection. In Proceedings of the 11th ECNDT Conference, Prague, Czech Republic, 6–11 October 2014.
14. Bachmann, F.; Hielscher, R.; Schaeben, H. Grain detection from 2d and 3d EBSD data—Specification of the MTEX algorithm. *Ultramicroscopy* **2011**, *111*, 1720–1733. [CrossRef]
15. Alpers, A.; Brieden, A.; Gritzmann, P.; Lyckegaard, A.; Poulsen, H.F. Generalized balanced power diagrams for 3D representations of polycrystals. *Philos. Mag.* **2015**, *95*, 1016–1028. [CrossRef]
16. Šedivỳ, O.; Brereton, T.; Westhoff, D.; Polívka, L.; Beneš, V.; Schmidt, V.; Jäger, A. 3D reconstruction of grains in polycrystalline materials using a tessellation model with curved grain boundaries. *Philos. Mag.* **2016**, *96*, 1926–1949. [CrossRef]
17. Šedivỳ, O.; Dake, J.M.; Krill III, C.E.; Schmidt, V.; Jäger, A. Description of the 3D morphology of grain boundaries in aluminum alloys using tessellation models generated by ellipsoids. *Image Anal. Stereol.* **2017**, *36*, 5–13. [CrossRef]
18. Šedivỳ, O.; Westhoff, D.; Kopeček, J.; Krill III, C.E.; Schmidt, V. Data-driven selection of tessellation models describing polycrystalline microstructures. *J. Stat. Phys.* **2018**, *172*, 1223–1246. [CrossRef]
19. Teferra, K.; Rowenhorst, D.J. Direct parameter estimation for generalised balanced power diagrams. *Philos. Mag. Lett.* **2018**, *98*, 79–87. [CrossRef]
20. Petrich, L.; Staněk, J.; Wang, M.; Westhoff, D.; Heller, L.; Šittner, P.; Krill, C.E.; Beneš, V.; Schmidt, V. Reconstruction of Grains in Polycrystalline Materials From Incomplete Data Using Laguerre Tessellations. *Microsc. Microanal.* **2019**, *25*, 743–752. [CrossRef] [PubMed]
21. Lyckegaard, A.; Lauridsen, E.M.; Ludwig, W.; Fonda, R.W.; Poulsen, H.F. On the Use of Laguerre Tessellations for Representations of 3D Grain Structures. *Adv. Eng. Mater.* **2011**, *13*, 165–170. [CrossRef]
22. Ghoshal, G.; Turner, J.A. Numerical model of longitudinal wave scattering in polycrystals. *IEEE Trans. Ultrason. Ferroelectr. Freq. Control* **2009**, *56*, 1419–1428. [CrossRef] [PubMed]
23. Shivaprasad, S.; Krishnamurthy, C.; Balasubramaniam, K. Modeling and simulation of ultrasonic beam skewing in polycrystalline materials. *Int. J. Adv. Eng. Sci. Appl. Math.* **2018**, *10*, 70–78. [CrossRef]
24. Ryzy, M.; Grabec, T.; Sedlák, P.; Veres, I.A. Influence of grain morphology on ultrasonic wave attenuation in polycrystalline media with statistically equiaxed grains. *J. Acoust. Soc. Am.* **2018**, *143*, 219–229. [CrossRef]
25. Van Pamel, A.; Brett, C.R.; Huthwaite, P.; Lowe, M.J. Finite element modelling of elastic wave scattering within a polycrystalline material in two and three dimensions. *J. Acoust. Soc. Am.* **2015**, *138*, 2326–2336. [CrossRef]
26. Van Pamel, A.; Sha, G.; Rokhlin, S.I.; Lowe, M.J. Finite-element modelling of elastic wave propagation and scattering within heterogeneous media. *Proc. R. Soc. A: Math. Phys. Eng. Sci.* **2017**, *473*, 20160738. [CrossRef]
27. Van Pamel, A.; Sha, G.; Lowe, M.J.; Rokhlin, S.I. Numerical and analytic modelling of elastodynamic scattering within polycrystalline materials. *J. Acoust. Soc. Am.* **2018**, *143*, 2394–2408. [CrossRef]
28. Quey, R.; Dawson, P.; Barbe, F. Large-scale 3D random polycrystals for the finite element method: Generation, meshing and remeshing. *Comput. Methods Appl. Mech. Eng.* **2011**, *200*, 1729–1745. [CrossRef]
29. Huthwaite, P. Accelerated finite element elastodynamic simulations using the GPU. *J. Comput. Phys.* **2014**, *257*, 687–707. [CrossRef]
30. *Standard ASTM E112*; Standard Test Methods for Determining Average Grain Size. ASTM International: West Conshohocken, PA, USA, 2003.
31. Margetan, F.J.; Nieters, E.; Haldipur, P.; Brasche, L.; Chiou, T.; Keller, M.; Degtyar, A.; Umbach, J.; Hassan, W.; Patton, T.; et al. *Fundamental Studies of Nickel Billet Materials-Engine Titanium Consortium Phase II*; National Technical Information Service (NTIS): Springfield, MA, USA, 2005.
32. Walte, F.; Schwender, T.; Hirsekorn, S.; Schubert, F.; Spies, M. *Reaktorsicherheitsforschung—Vorhaben-Nr.: 1501442 "Berechnung der Ultraschallstreuung für einen Verbesserten Nachweis von Rissartigen Fehlern in Austenitischen Schweissnähten. Phase 1: Berechnung der Ultraschallstreuung für 2DSchweissnahtmodelle"*; Technical Report; Fraunhofer-Institut für Zerstörungsfreie Prüfverfahren IZFP: Saarbrücken, Germany, 2015.
33. Tromans, D. Elastic anisotropy of HCP metal crystals and polycrystals. *Int. J. Res. Rev. Appl. Sci* **2011**, *6*, 462–483.
34. Shannon, C.E. Communication in the presence of noise. *Proc. IRE* **1949**, *37*, 10–21. [CrossRef]
35. Fließbach, T. *Statistische Physik*; Springer: Berlin/Heidelberg, Germany, 1993.
36. Gaspard, P. *Chaos, Scattering and Statistical Mechanics*; Cambridge University Press: Cambridge, UK, 2005; Volume 9.

37. Gubernatis, J.; Krumhansl, J. Macroscopic engineering properties of polycrystalline materials: Elastic properties. *J. Appl. Phys.* **1975**, *46*, 1875–1883. [CrossRef]
38. Weaver, R.L. Diffusivity of ultrasound in polycrystals. *J. Mech. Phys. Solids* **1990**, *38*, 55–86. [CrossRef]
39. Hirsekorn, S. Elastic properties of polycrystals: A review. *Texture, Stress. Microstruct.* **1990**, *12*, 1–14. [CrossRef]
40. Hirsekorn, S. The scattering of ultrasonic waves by multiphase polycrystals. *J. Acoust. Soc. Am.* **1988**, *83*, 1231–1242. [CrossRef]
41. Born, M. Quantenmechanik der stoßvorgänge. *Z. Phys.* **1926**, *38*, 803–827. [CrossRef]
42. Torquato, S. *Random Heterogeneous Materials: Microstructure and Macroscopic Properties*; Springer Science & Business Media: Berlin/Heidelberg, Germany, 2013; Volume 16.
43. Illian, J.; Penttinen, A.; Stoyan, H.; Stoyan, D. *Statistical Analysis and Modelling of Spatial Point Patterns*; John Wiley & Sons: Hoboken, NJ, USA, 2008; Volume 70.
44. Man, C.S.; Paroni, R.; Xiang, Y.; Kenik, E.A. On the geometric autocorrelation function of polycrystalline materials. *J. Comput. Appl. Math.* **2006**, *190*, 200–210. [CrossRef]
45. Arguelles, A.P.; Turner, J.A. Ultrasonic attenuation of polycrystalline materials with a distribution of grain sizes. *J. Acoust. Soc. Am.* **2017**, *141*, 4347–4353. [CrossRef] [PubMed]
46. Dobrovolskij, D.; Hirsekorn, S.; Spies, M. Simulation of Ultrasonic Materials Evaluation Experiments Including Scattering Phenomena due to Polycrystalline Microstructure. *Phys. Procedia* **2015**, *70*, 644–647. [CrossRef]
47. Chiu, S.N.; Stoyan, D.; Kendall, W.S.; Mecke, J. *Stochastic Geometry and Its Applications*; John Wiley & Sons: Hoboken, NJ, USA, 2013.
48. Ohser, J.; Schladitz, K. *3D Images of Materials Structures: Processing and Analysis*; John Wiley & Sons: Hoboken, NJ, USA, 2009.
49. Xue, X.; Righetti, F.; Telley, H.; Liebling, T.M.; Mocellin, A. The laguerre model for grain growth in three dimensions. *Philos. Mag. B* **1997**, *75*, 567–585. [CrossRef]
50. Kühn, M.; Steinhauser, M.O. Modeling and simulation of microstructures using power diagrams: Proof of the concept. *Appl. Phys. Lett.* **2008**, *93*, 034102. [CrossRef]
51. Okabe, A.; Boots, B.; Sugihara, K.; Chiu, S.N. *Spatial Tessellations: Concepts and Applications of Voronoi Diagrams*; John Wiley & Sons: Hoboken, NJ, USA, 2009; Volume 501.
52. Redenbach, C. Microstructure models for cellular materials. *Comput. Mater. Sci.* **2009**, *44*, 1397–1407. [CrossRef]
53. Geißendörfer, M.; Liebscher, A.; Proppe, C.; Redenbach, C.; Schwarzer, D. Stochastic multiscale modeling of metal foams. *Probabilistic Eng. Mech.* **2014**, *37*, 132–137. [CrossRef]
54. Kampf, J.; Schlachter, A.L.; Redenbach, C.; Liebscher, A. Segmentation, statistical analysis, and modelling of the wall system in ceramic foams. *Mater. Charact.* **2015**, *99*, 38–46. [CrossRef]
55. Abdullahi, H.; Liang, Y.; Gao, S. Predicting the elastic properties of closed-cell aluminum foams: A mesoscopic geometric modeling approach. *SN Appl. Sci.* **2019**, *1*, 380. [CrossRef]
56. Liebscher, A. Laguerre approximation of random foams. *Philos. Mag.* **2015**, *95*, 2777–2792. [CrossRef]
57. Mościński, J.; Bargieł, M.; Rycerz, Z.; Jacobs, P. The force-biased algorithm for the irregular close packing of equal hard spheres. *Mol. Simul.* **1989**, *3*, 201–212. [CrossRef]
58. Jodrey, W.S.; Tory, E.M. Simulation of random packing of spheres. *Simulation* **1979**, *32*, 1–12. [CrossRef]
59. Bezrukov, A.; Stoyan, D.; Bargieł, M. Spatial statistics for simulated packings of spheres. *Image Anal. Stereol.* **2001**, *20*, 203–206. [CrossRef]
60. Bezrukov, A.; Bargieł, M.; Stoyan, D. Statistical analysis of simulated random packings of spheres. *Part. Part. Syst. Charact. Meas. Descr. Part. Prop. Behav. Powders Other Disperse Syst.* **2002**, *19*, 111–118. [CrossRef]
61. He, D.; Ekere, N. Computer Simulation of Powder Compaction of Spherical Particles. *J. Mater. Sci. Lett.* **1998**, *17*, 1723–1725. [CrossRef]
62. Wu, Y.; Fan, Z.; Lu, Y. Bulk and interior packing densities of random close packing of hard spheres. *J. Mater. Sci.* **2003**, *38*, 2019–2025. [CrossRef]
63. Rhines, F.; Patterson, B. Effect of the degree of prior cold work on the grain volume distribution and the rate of grain growth of recrystallized aluminum. *Metall. Trans. A* **1982**, *13*, 985–993. [CrossRef]
64. Spies, M. Kirchhoff evaluation of scattered elastic wavefields in anisotropic media. *J. Acoust. Soc. Am.* **2000**, *107*, 2755–2759. [CrossRef]
65. Červený, V. Reflection/transmission laws for slowness vectors in viscoelastic anisotropic media. *Stud. Geophys. Geod.* **2007**, *51*, 391–410. [CrossRef]
66. Auld, B. General electromechanical reciprocity relations applied to the calculation of elastic wave scattering coefficients. *Wave Motion* **1979**, *1*, 3–10. [CrossRef]
67. Scheben, R.; Rieder, H.; Spies, M.; Götz, S. *Kopplung von EFIT und GPSS zur Schnellen Ultraschallsimulation*; NDT.net. German Society of NDT: Berlin, Germany, 2010; Volume 2.
68. Spies, M. Prediction of Ultrasonic Flaw Signals and Model-to-Experiment Comparison. In Proceedings of the AIP Conference Proceedings, Salt Lake, UT, USA, 10–11 August 2005; Volume 760, pp. 1851–1858.
69. Frigo, M.; Johnson, S.G. FFTW: An adaptive software architecture for the FFT. In Proceedings of the 1998 IEEE International Conference on Acoustics, Speech and Signal Processing, ICASSP'98 (Cat. No. 98CH36181), Seattle, WA, USA, 12–15 May 1998; Volume 3, pp. 1381–1384.

70. Frigo, M.; Johnson, S.G. *FFTW: Fastest Fourier Transform in the West;* Astrophysics Source Code Library **2012**. Available online: https://ui.adsabs.harvard.edu/abs/2012ascl.soft01015F/abstract (accessed on 21 July 2021).
71. Dagum, L.; Menon, R. OpenMP: An industry standard API for shared-memory programming. *IEEE Comput. Sci. Eng.* **1998**, *5*, 46–55. [CrossRef]
72. Chandra, R.; Dagum, L.; Kohr, D.; Menon, R.; Maydan, D.; McDonald, J. *Parallel Programming in OpenMP*; Morgan Kaufmann: Burlington, MA, USA, 2001.
73. Fraunhofer Institute for Industrial Mathematics ITWM.. Cluster Homepage. 2021. Available online: https://www.itwm.fraunhofer.de/en/about-itwm/profile/central-it-infrastructure.html (accessed on 21 July 2021).
74. Guo, Y.; Wang, B.; Hou, S. Aging precipitation behavior and mechanical properties of Inconel 617 superalloy. *Acta Metall. Sin. (English Lett.* **2013**, *26*, 307–312. [CrossRef]
75. Poulsen, H.F. An introduction to three-dimensional X-ray diffraction microscopy. *J. Appl. Crystallogr.* **2012**, *45*, 1084–1097. [CrossRef]
76. Ludwig, W.; Reischig, P.; King, A.; Herbig, M.; Lauridsen, E.; Johnson, G.; Marrow, T.; Buffiere, J.Y. Three-dimensional grain mapping by x-ray diffraction contrast tomography and the use of Friedel pairs in diffraction data analysis. *Rev. Sci. Instruments* **2009**, *80*, 033905. [CrossRef] [PubMed]
77. Ducousso-Ganjehi, L.; Châtillon, S.; Dorval, V.; Gilles-Pascaud, C.; Jenson, F. Modelling of the Ultrasonic Propagation in Titanium Alloy Materials. In Proceedings of the AeroNDT 2012 4th International Symposium on NDT in Aerospace, Augsburg, Germany, 13–14 November 2012; NDT.net. German Society of NDT: Berlin, Germany, 2012.
78. Pilchak, A.L.; Li, J.; Rokhlin, S.I. Quantitative comparison of microtexture in near-alpha titanium measured by ultrasonic scattering and electron backscatter diffraction. *Metall. Mater. Trans. A* **2014**, *45*, 4679–4697. [CrossRef]

Chapter 3
Modelling of Geometrical Microstructures and Mechanical Behaviour of Constituents

Heiko Andrä, Dascha Dobrovolskij, Katja Schladitz, Sarah Staub and Ralf Müller

3.1 Analysis of Fibre Orientation for Glass Fibre Reinforced Polymers Based on µCT Scans

3.1.1 Sample Preparation and Analysis of Fibre Direction

Throughout this chapter, a 2 mm thick polybutylene terephthalate (PBT) plate reinforced with 20 weight percent glass fibres is considered. First, the material is spatially imaged by micro-computed X-ray tomography (µCT), in order to determine analytically essential micro-structure features. Measuring the fibre orientation requires µCT with nominal resolutions in the range well below 10 µm. To achieve this with a standard laboratory CT setup, samples of a few millimetre diameter have to be extracted from the plate. These samples are extracted from the plate according to the scheme shown in Fig. 3.1. To choose five samples is a compromise between the effort for imaging and analysing on the one hand and capturing the systematic microstructural

H. Andrä (✉) · D. Dobrovolskij · K. Schladitz · S. Staub
Fraunhofer Institute for Industrial Mathematics, 67663 Kaiserslautern, Germany
e-mail: heiko.andrae@itwm.fraunhofer.de

D. Dobrovolskij
e-mail: dascha.dobrovolskij@itwm.fraunhofer.de

K. Schladitz
e-mail: katja.schladitz@itwm.fraunhofer.de

S. Staub
e-mail: sarah.staub@itwm.fraunhofer.de

D. Dobrovolskij
University of Applied Sciences, 64295 Darmstadt, Germany

R. Müller
University of Kaiserslautern, 67653 Kaiserslautern, Germany
e-mail: ram@rhrk.uni-kl.de

S. Diebels and S. Rjasanow (eds.), *Multi-scale Simulation of Composite Materials*, Mathematical Engineering, https://doi.org/10.1007/978-3-662-57957-2_3

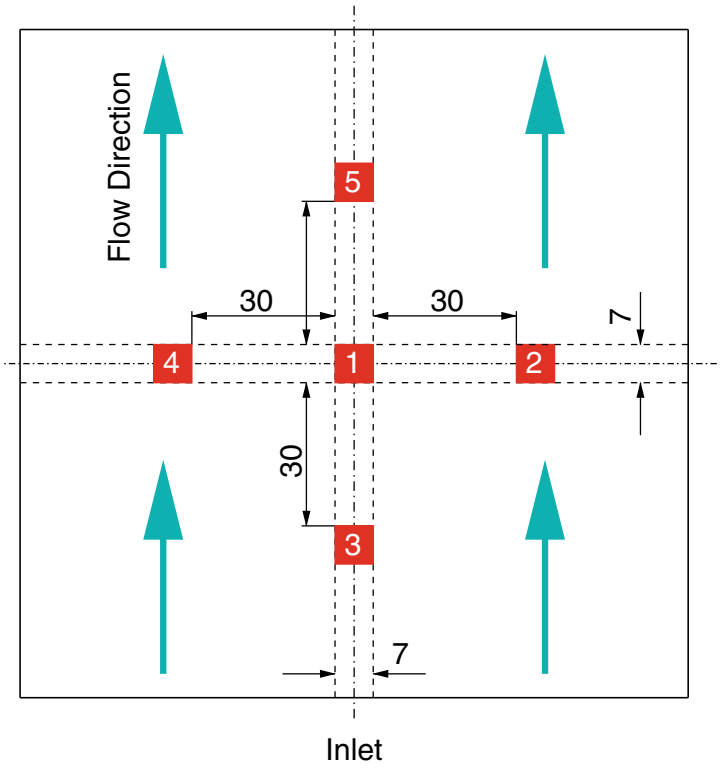

Fig. 3.1 Moulded glass fibre reinforced PBT plate with marked specimen positions

differences expected at different positions w.r.t. the inlet or the flow front, respectively. The positions are thus chosen according to the expected behaviour of the latter. The five taken cuboidal samples of base edge length 2 mm are imaged using ITWM's CT device at a tube voltage of 160 kV and using a flat bed PerkinElmer and a Thales detector, respectively. A voxel edge length of 1.2–1.3 µm is chosen, such that the fibre diameter is resolved by approximately ten voxels. The resulting 2D projection images are reconstructed using weighted filtered back projection, and the microstructures are analysed based on the obtained three dimensional image data.

The analysis focuses on the fibre orientation, in particular in order to determine the thickness of the different layers, which are typical for injection moulded GFRP plates, and the main fibre orientation in each layer. In the following, the theoretical background of the applied fibre orientation analysis method is summarised. Subsequently, the pre- and post-processing is described. The analysis results for the five samples are finally presented in Sect. 3.1.2.

The fibre directions in the µCT images are analysed by means of the "SubField-FiberDirection" function of ITWM's software tool MAVI [4]. This function computes, based on the local grey values, for each voxel the local fibre orientation. From these local orientations, restricted to the fibre component, local orientation tensors are derived. The following two paragraphs summarise very shortly the mathematical basis of the local orientation measurement. The fibre component is interpreted mathematically as a random closed set Φ in the three-dimensional Euclidean space, see e.g. [15, 18, 20]. The fibre direction distribution in a typical point of this set corresponds to a measure in the space of non-oriented directions

$$R(A) = \frac{1}{2\pi V(W)} \mathbb{E} \int_{W \cap \Phi} I_A(\nu(x))\, \mathrm{d}x, \tag{3.1}$$

where $A \subseteq \mathbb{S}^2_+$ denotes a measurable set of non-oriented directions, $\nu(x)$ the direction of the fibre system at location $x \in W$, and $W \subseteq \mathbb{R}^3$ the considered region. The expectation $\mathbb{E}$ is computed with respect to the distribution law of the random set Φ. The function I_A is an indicator for the set A, i.e. $I_A(\nu) = 1$ if $\nu \in A$ and otherwise 0.

The local fibre direction in each voxel is derived from the Hessian matrix—the matrix of second order grey value partial derivatives. In order to compute it, the original image $f : W \cap \mathbb{L} \mapsto \{0, \ldots, 255\}$ is first smoothed by a Gaussian filter g_σ of size σ. Here $\mathbb{L} = s\mathbb{Z}^3$, $s \in \mathbb{R}$ denotes a 3D orthogonal isotropic lattice. Then the Hessian matrix $H(x)$ is approximated by finite difference quotients:

$$H_{ij}(\mathbf{x}) = \left(\frac{\partial^2}{\partial x_i \partial x_j} \right) (f * g_\sigma)(\mathbf{x}), \quad i, j = 1, 2, 3, \ \mathbf{x} \in \mathbb{L}. \tag{3.2}$$

Let $|\lambda_1| \leq |\lambda_2| \leq |\lambda_3|$ be the eigenvalues of the Hessian H, ordered with respect to magnitude. Then the local direction of the fibre system Φ in x is given as the direction corresponding to the smallest (in magnitude) eigenvalue $|\lambda_1|$ as glass fibres appear bright compared to the polymer matrix surrounding them, see [3, 22]. Roughly, the idea behind this approach is a local approximation of the fibre by a cylinder of thickness 2σ in each voxel. The local fibre direction is then associated with the minimal curvature of the grey value formation, the spatial direction in which the least change is observed.

Initially, the method yields a local orientation in each voxel. In a second step, the result is masked with a segmentation of the fibre system. Note that this means just, that the fibre system has to be separated from the polymer matrix. The segmentation of individual fibres in the 3D image is however not needed.

Given the distribution R of the fibre orientation in the typical point of the fibre system, the second order orientation tensor a is derived as the outer product of the components ν_1, ν_2, ν_3 of the orientation vector averaged with respect to R

$$a_{ij} = \int \nu_i \nu_j R(\mathrm{d}\nu), \quad i, j = 1, 2, 3. \tag{3.3}$$

Thus, based on the image data, the orientation tensor is computed by averaging the voxel-wise product over defined sub-volumes $W_0 \subseteq W$

$$\hat{a}_{ij} = \sum_{\mathbf{x} \in W_0 \cap \mathbb{L} \cap \Phi} \nu_i(\mathbf{x}) \nu_j(\mathbf{x}), \tag{3.4}$$

see [21]. The main fibre direction $\bar{\nu}$ in sub-volume W is obtained as the eigenvector associated to the largest eigenvalue of the tensor a. Of course, this main fibre direction is meaningful only if the distribution R has a cluster-like shape [2].

Usually, the fibre system is segmented from the 3D image by a simple global thresholding. This requires to remove global grey value fluctuations within the image—a task easily achieved by so-called shading correction: The image is smoothed extensively and subsequently subtracted from the original. Afterwards, a global grey value threshold suffices to separate the bright fibres from the dark matrix. MAVI's "SubFieldFiberDirection" suggests to apply the threshold according to Otsu [17] multiplied by 1.25 to avoid erroneous orientation information at the fibre edges.

In this study, this usual procedure turned out to distort the strongly anisotropic fibre orientation distributions within the layers towards isotropy. Therefore, to ensure that exclusively voxels from the fibre cores contribute, the fibre system is segmented based on Frangi's vesselness index [3]. Again, the eigenvalues of the Hessian matrix are exploited, this time to gain local structure shape information. The structure is locally fibrous if and only if there are one small and two large eigenvalues (in magnitude). Frangi's index is designed for detecting bright fibres on dark background. Thus it is non-zero only if $\lambda_2, \lambda_3 < 0$. In this case it is computed as

$$\Big(1 - \exp\big(-2\lambda_2^2/\lambda_3^2\big)\Big) \exp\big(-2\lambda_1^2/|\lambda_2\lambda_3|\big)\Big(1 - \exp\big(-2(\lambda_1^2+\lambda_2^2+\lambda_3^2)/c^2\big)\Big)$$

with $c^2 = (\max_{\mathbf{x}\in W\cap\mathbb{L}} ||H(\mathbf{x})||_F)^2 = \max_{\mathbf{x}\in W\cap\mathbb{L}}(\lambda_1(\mathbf{x})^2 + \lambda_2(\mathbf{x})^2 + \lambda_3(\mathbf{x})^2)$. This index is now computed and used to derive a more precise segmentation of the fibre system. That is, the global grey value threshold is applied on the image holding in each voxel the local Frangi's index.

3.1.2 Results

As a preliminary step, the three-dimensional images are rotated such that the imaged cuboidal sample is oriented parallel to the coordinate axes. More precisely, the x-direction corresponds to the injection direction, y to the cross-flow direction and z to the direction in thickness of the plate.

Second, the layers are approximated. To this end, the images are first denoised by a $5 \times 5 \times 5$ pixel median filter. Then, the grey values are averaged along rays in y-direction. This results in distinct bright spots the x–z-plane in the central region, where high grey values are summed along fibres, see Fig. 3.2, right. The layers are finally deduced from the curves of the row-wise grey value maxima: The global maximum of the B-spline smoothed graph indicates the centre. The lower and the upper bounds are derived from the two local minima closest to the global maximum. More precisely, we chose the argument of the higher of these two minima to define the half-width of the symmetric interval, see Fig. 3.2, left.

This yields the thickness values as reported in Table 3.1. The orientation tensor for each layer is derived by averaging over the complete layer. A volume rendering of

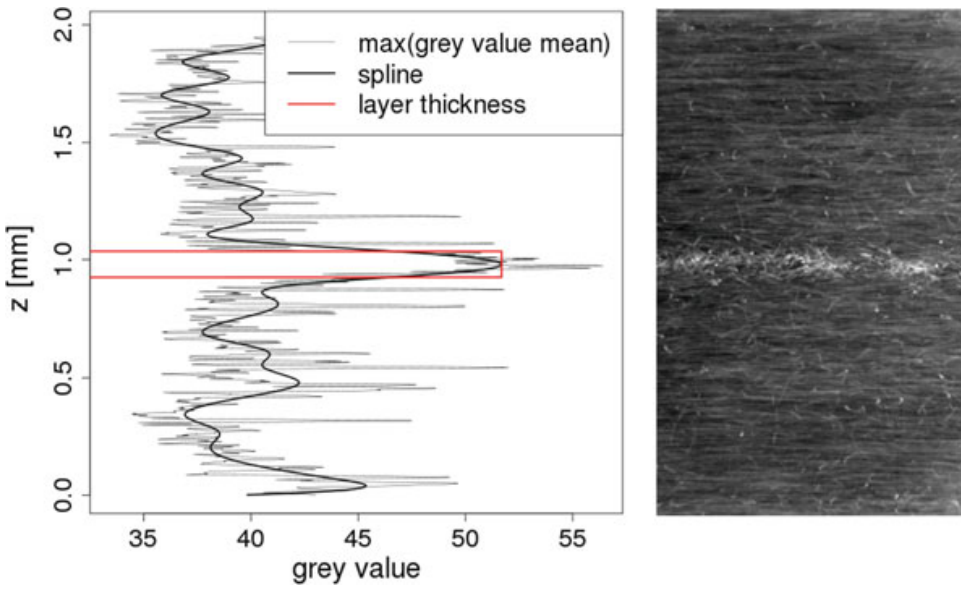

Fig. 3.2 Grey value means for determining the misoriented central layer, illustrated for sample 5. Left: row-wise maxima of averaged grey values. Right: grey value means along stripes in y-direction

the fibre system contributing to the orientation results is shown in Fig. 3.3 illustrating the orientation tensor results for the total thickness of the plate.

Subsequently, the local fibre orientation is analysed as described in Sect. 3.1.1 above. This yields the second order orientation tensors in the three layers, see Table 3.1. As expected, the fibres are mainly oriented along the x-axis (flow direction) in the outer layers, whereas the fibres are oriented orthogonal to the flow direction in the central layer.

The fibre orientation in the misoriented layers differs with respect to proportions of fibres oriented in x- and y-directions (see Table 3.1 columns a_{xx} and a_{yy}). Figures 3.4 and 3.5 contain slices through the upper and the misoriented central layers of all five samples. Both these views as well as the quantitative results from Table 3.1 confirm the expected curved flow front [14]. The main fibre orientation in the central layers in the outer plate regions are tilted towards the plate edges in x-direction. This observation is in perfect accordance with the expected faster fibre transport at the outer regions compared to the inner plate part.

To summarise, in all three layers the fibres are almost oriented in-plane, i.e. the thickness component z of the orientation tensor is small compared to the entries in x- and y-direction. For all samples the flow direction is the governing direction in the outer layers and the fibres are re-oriented in the central layer. Thus, virtually generated volume elements should take into account the observed multi-layer composition in order to represent the microstructure appropriately.

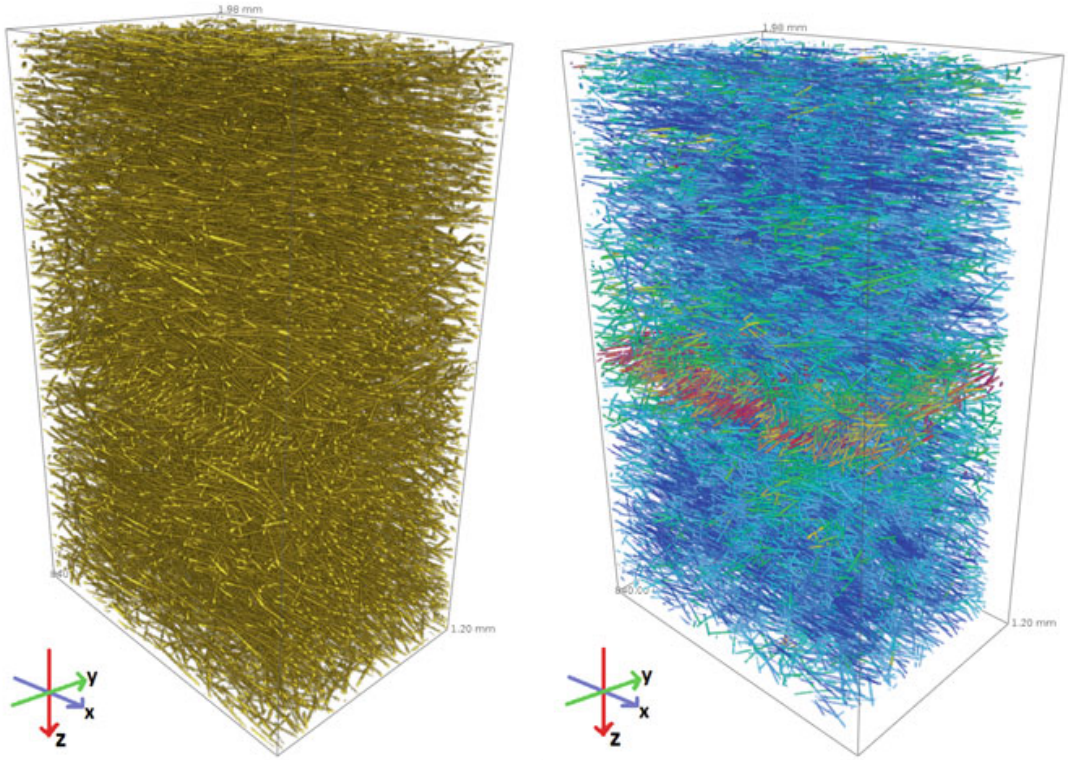

(a) Fibre system (b) Orientation tensor component a_{yy}

Fig. 3.3 Volume renderings of sample 5. Visualised are approximately 1.2 mm × 0.9 mm × 2.0 mm out of the totally analysed approximately 1.8 mm × 1.1 mm × 2.0 mm. Fibre system as obtained by thresholding the image holding the local Frangi's index as voxel grey value. The local fibre orientation analysis results are represented by the 2nd order orientation tensor component a_{yy}. That is, in plane, orthogonal to the injection direction x. The tensor component is colour coded using a blue-to-red colour table with blue indicating values close to 0 and red close to 1. The misoriented central layer is clearly visible due to the high (red) values for a_{yy} there

3.2 Microstructure Generation

In the following the generation of virtual microstructures which have the same properties as the structures considered in Sect. 3.1.2 is described.

Stochastic volume elements with a fibre content of 20% are considered. The morphology of the glass fibres is described by the fibre length of 250 µm and the fibre diameter of 10 µm. The complete thickness of the 2 mm thick plate is resolved in order to capture the layered structure of the moulded specimens. The samples are described by 1024 voxels in each direction, i.e. the size of a voxel in each direction is obtained as 1.9313 µm. Thus each single fibre is resolved by five voxels over the thickness. The fibre orientation in each layer as well as the thickness of the misoriented layer are prescribed according to Table 3.1.

The realisation of sample 1 is depicted in Fig. 3.6. The size of the sample is 2 mm (1024 voxels) in each direction. Fibres belonging to the misoriented middle layer are

Table 3.1 Analysis results for the 3D images of samples 1–5, extracted at the positions shown in Fig. 3.1. The thickness of the central layers varies not only due to the varying strength of the misorientation but also due to the misoriented layers not being oriented perfectly parallel to the plate. Note that values of 1.00 or 0.00 for orientation vector components are due to rounding

Sample-layer	Volume (mm^3)	Voxel size (μm)	# voxels	Orientation tensor diagonal elements			Main fibre orientation		
				a_{xx}	a_{yy}	a_{zz}	$\bar{\nu}_x$	$\bar{\nu}_y$	$\bar{\nu}_z$
1-1	1.82 × 2.21 × 0.99	1.3	1 400 × 1 700 × 760	0.68	0.27	0.04	−0.99	0.07	−0.00
1-2	1.88 × 2.47 × 0.09	1.3	1 450 × 1 900× 67	0.22	0.73	0.06	0.17	−0.99	−0.01
1-3	1.82 × 2.34 × 0.84	1.3	1 400 × 1 800 × 650	0.66	0.28	0.06	1.00	−0.08	−0.01
2-1	1.56 × 0.86 × 0.90	1.2	1 300× 720 × 750	0.69	0.26	0.05	1.00	0.10	−0.00
2-2	1.68 × 1.92 × 0.08	1.2	1 400 × 1 600× 65	0.35	0.60	0.05	−0.47	0.88	−0.01
2-3	1.68 × 1.65 × 0.87	1.2	1 400 × 1 375 × 725	0.69	0.26	0.05	1.00	0.05	−0.00
3-1	2.47 × 2.08 × 0.78	1.3	1 900 × 1 600 × 600	0.60	0.35	0.04	−0.91	−0.41	−0.05
3-2	2.60 × 2.47 × 0.07	1.3	2 000 × 1 900× 55	0.16	0.81	0.03	0.16	−0.99	−0.00
3-3	2.47 × 2.21 × 0.78	1.3	1 900 × 1 700 × 600	0.65	0.25	0.10	−0.99	−0.14	−0.03
4-1	1.56 × 1.62 × 0.90	1.2	1 300 × 1 350 × 750	0.66	0.28	0.05	−0.99	0.16	−0.00
4-2	1.56 × 1.62 × 0.06	1.2	1 300 × 1 350× 51	0.40	0.58	0.02	−0.60	−0.81	−0.02
4-3	1.56 × 0.99 × 0.90	1.2	1 300× 825 × 750	0.67	0.27	0.06	−0.98	0.18	0.00
5-1	1.80 × 1.46 × 0.90	1.2	1 500 × 1 215 × 750	0.68	0.26	0.06	−1.00	−0.02	0.00
5-2	1.80 × 1.98 × 0.11	1.2	1 500 × 1 650× 93	0.20	0.77	0.03	0.16	−0.99	−0.00
5-3	1.77 × 1.14 × 0.90	1.2	1 475× 950 × 750	0.69	0.24	0.06	1.00	−0.02	−0.01

highlighted in green. The fibres are distributed in such a way that the oriented and the misoriented layer are not separated in a strict manner. Fibres may overlap into the neighbouring layer.

In a next step the generated structures are compared to the corresponding samples of the µCT images from Sect. 3.1.1. Figures 3.7 and 3.8 display 2D slices for each sample from the upper and the middle layer. A comparison to the corresponding CT slices shows good agreement between the structures. It is noted that the virtual structures display a larger part of the microstructure (2 mm vs. 1.2 mm edge length) and therefore the fibres appear smaller than in the CT images.

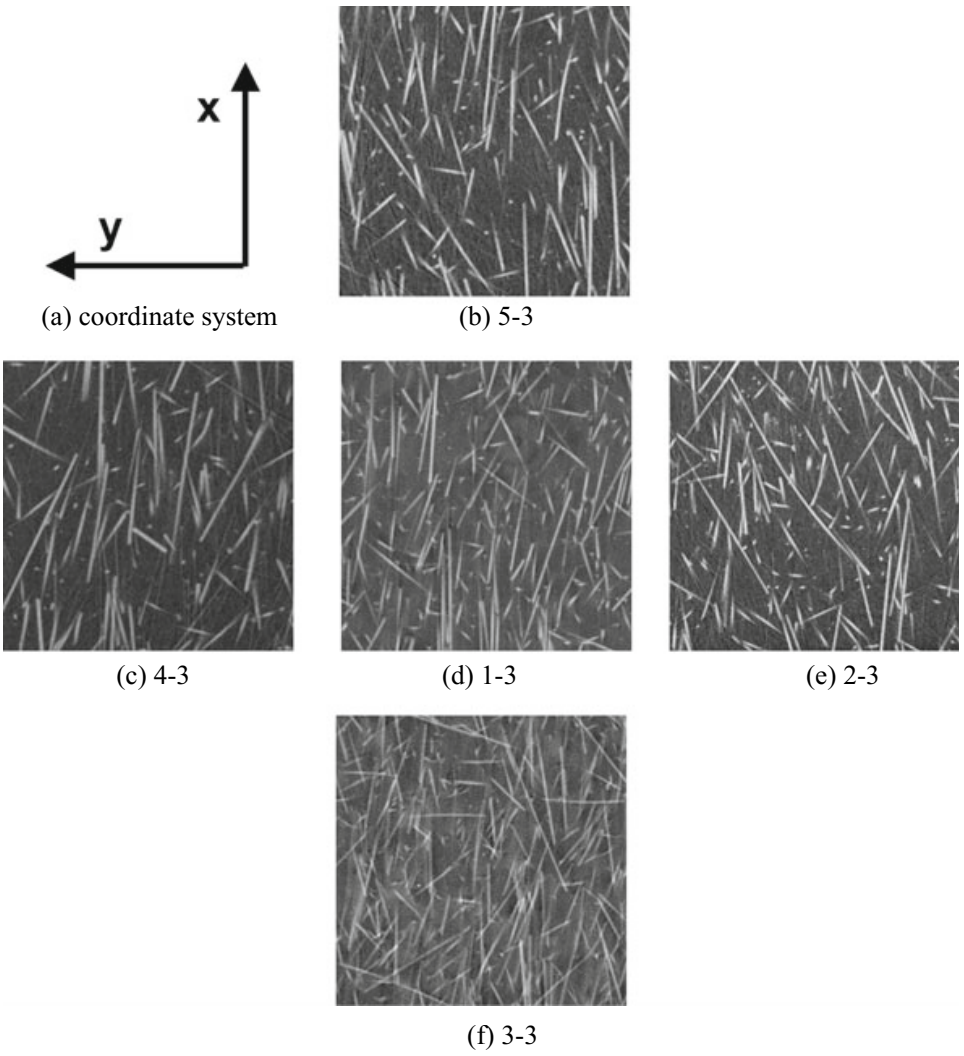

Fig. 3.4 1 000 × 1 000 pixel slices from the upper layers of samples 1–3 and 800 × 1 000 pixel slices from the upper layers of samples 4 and 5. Images are arranged as the sample extraction positions shown in Fig. 3.1

3.3 Identification of Material Parameters for the Matrix Material

Many methods for the characterisation of fibre reinforced composites are based on measurements of composite specimens, which have certain special fibre orientations, e.g. highly oriented or parallel fibres. In contrast, only measurements of the pure constituents are necessary in the presented method. This is an advantage especially in the case, if the constituents are isotropic or transversely anisotropic instead of fully anisotropic. In this section the method for the determination of material parameters and functions is described which are necessary to describe the rate-independent nonlinear material behaviour of the polymer matrix.

Polybutylene terephthalate (PBT), which is considered as matrix material in this book, is a thermoplastic semi-crystalline polymer and a type of polyester [1]. This

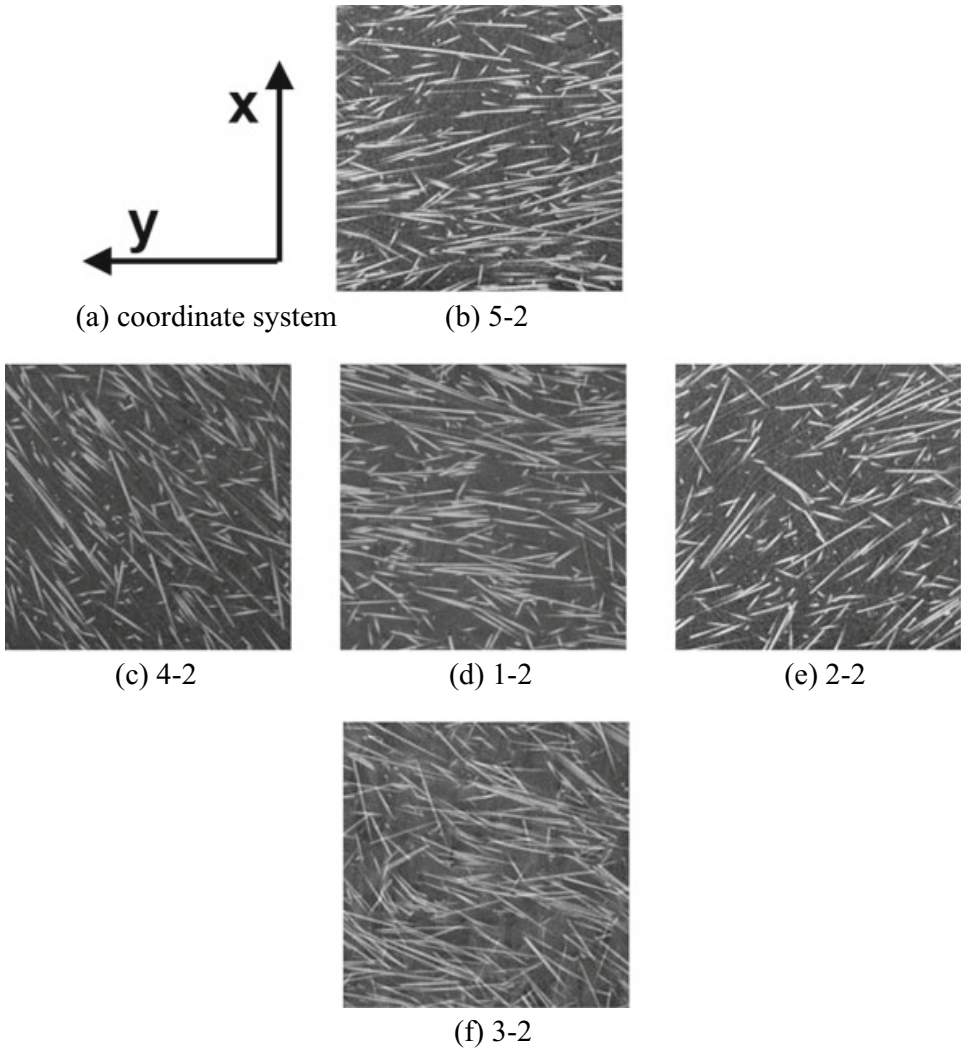

(a) coordinate system (b) 5-2

(c) 4-2 (d) 1-2 (e) 2-2

(f) 3-2

Fig. 3.5 1 000 × 1 000 pixel slices from the misoriented central layers in samples 1–5. Images are arranged as the sample extraction positions shown in Fig. 3.1

polymer material shows a complex temperature-dependent viscoplastic behaviour with damage. However, this complex behaviour can be simplified to a time- and temperature-independent model for many applications. For the sake of simplicity, a standard time-independent elastoplasticity model with isotropic hardening and with a single additional internal variable

$$d = \frac{A_d}{A_0} \in [0, 1]$$

for isotropic damage is considered during the further procedure [6, 16, 19]. The damage variable d is defined as the share of the damaged surface area A_d on the total representative cross-section A_0. The damage variable d can be measured by several methods. The simplest method is to measure the degradation of the elastic modulus

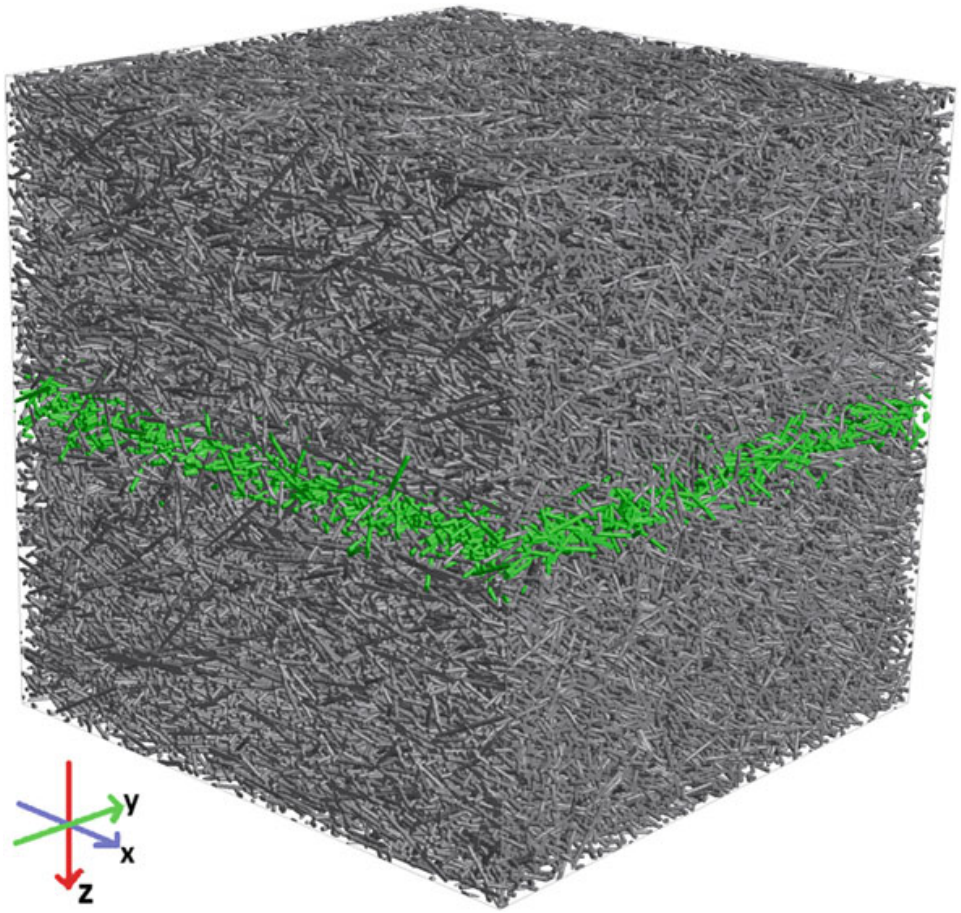

Fig. 3.6 Visualisation with GeoDict [5] of sample 1, size of realisation 2 mm in each direction

$$d = 1 - \frac{E_{\mathrm{d}}}{E_{\mathrm{e}}}.$$

The degraded modulus can be determined in the unloading regime of cyclic tests (see Fig. 3.10).

The corresponding rate-independent material law with memory is introduced in Chap. 4

Remark 3.1 The viscoelastic damping, which is related to the area of the hysteresis loops is not taken into account and the different material parameters are determined for each testing speed. However, the model can be extended to capture viscoelastic or viscoplastic effects.

Now the elastoplastic material model with damage from Chap. 4 is repeated shortly. The free energy is decomposed into an elastic part $(1-d)W_{\mathrm{elastic}}$, a plastic part $(1-d)W_{\mathrm{plastic}}$, and a regularisation part W_{damage} resulting in

$$W(\varepsilon, d, \varepsilon_{\mathrm{p}}, r) = (1-d)(W_{\mathrm{elastic}}(\varepsilon - \varepsilon_{\mathrm{p}}) + W_{\mathrm{plastic}}(\varepsilon_{\mathrm{p}}, r)) + W_{\mathrm{damage}}(d)$$

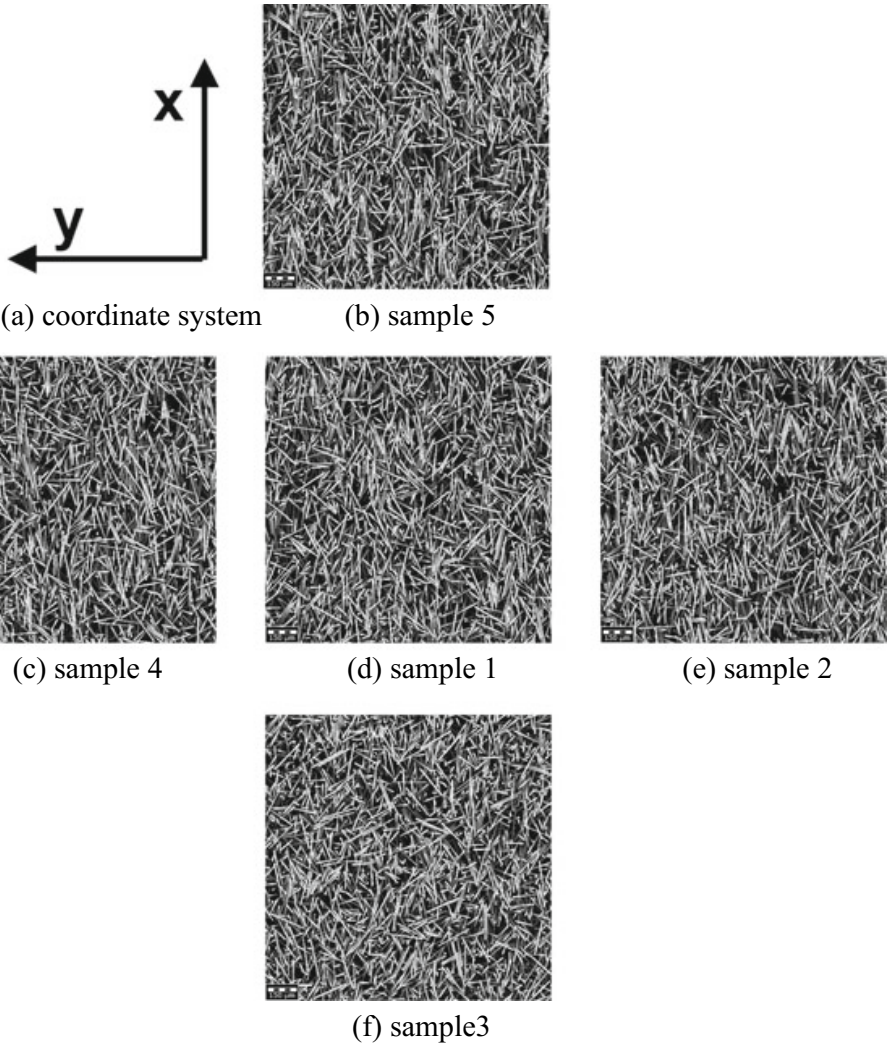

(a) coordinate system (b) sample 5

(c) sample 4 (d) sample 1 (e) sample 2

(f) sample3

Fig. 3.7 1 024 × 1 024 pixel (2 mm × 2 mm) slices from the upper layers of virtual realisations of samples 1–5. Images are arranged as the sample extraction positions shown in Fig. 3.1

Both the elastic and plastic part are multiplied by the factor $(1 - d)$ for including the damage [6, 16]. The additional term W_{damage} guarantees $d < 1$. In the case of isotropic hardening the plastic part is written as a sum of both the linear hardening term and the Voce hardening term

$$W_{\text{plastic}}(\varepsilon_{\text{p}}, r) = W_{\text{iso}}(r) = \frac{1}{2} H_0 r^2 + (K_\infty - K_0)\left(r + \frac{e^{-\delta r}}{\delta}\right).$$

The plastic part W_{iso} depends on three positive material parameters

$$H_0 \geq 0, \qquad a_1 := K_\infty - K_0 \geq 0, \qquad \delta \geq 0 \tag{3.5}$$

which have to be fitted for the plastic behaviour. The expansion of the yield surface is then obtained as

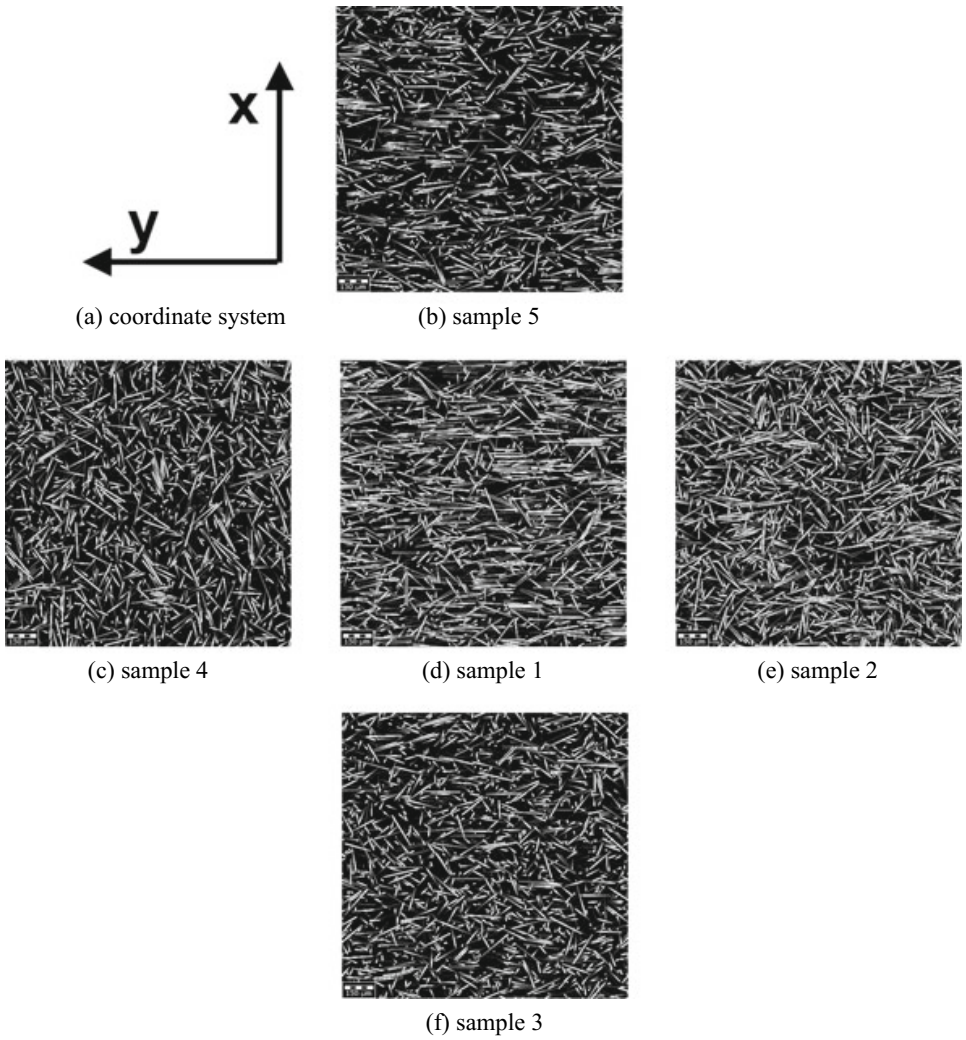

(a) coordinate system (b) sample 5

(c) sample 4 (d) sample 1 (e) sample 2

(f) sample 3

Fig. 3.8 1 024 × 1 024 pixel (2 mm × 2 mm) slices from the misoriented central layers of virtual realisations of samples 1–5. Images are arranged as the sample extraction positions shown in Fig. 3.1

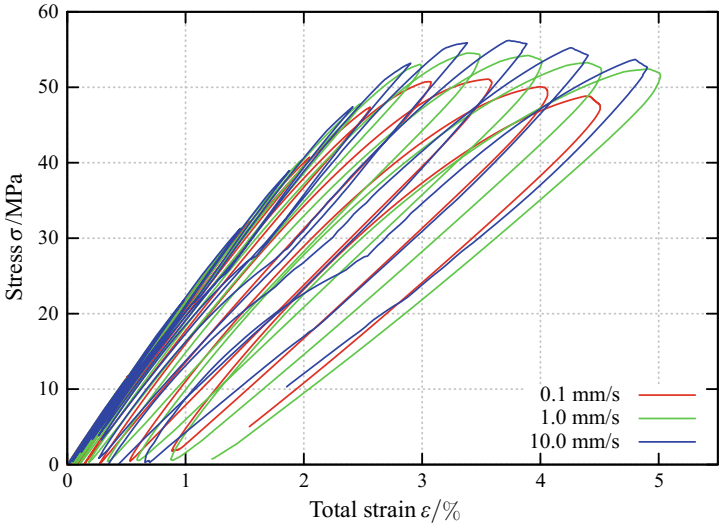

Fig. 3.9 Measured stress-strain curves for PBT at testing speeds of 0.1, 1.0 and 10.0 mm/s

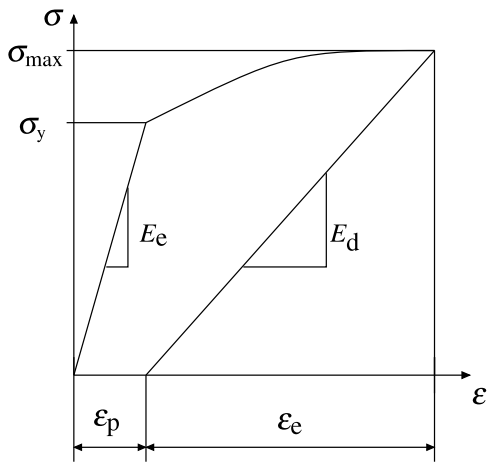

Fig. 3.10 Schematic stress-strain diagram of the first load cycle

$$\psi(r) = \tilde{\psi}(r; \sigma_y, H_0, a_1, \delta) = \sigma_y + \frac{\partial W_{\text{iso}}}{\partial r} = \sigma_y + H_0 r + a_1 \left(1 - e^{-\delta r}\right),$$

where σ_y denotes the initial yield stress. The damage conjugated force is defined by

$$\begin{aligned} Y &= -\frac{\partial W}{\partial d} = W_{\text{elastic}} + W_{\text{iso}}(r) + \frac{\partial W_{\text{damage}}}{\partial d} \\ &= \frac{1}{2}\varepsilon_e : \mathbb{C} : \varepsilon_e + W_{\text{iso}}(r) + \frac{\partial W_{\text{damage}}}{\partial d}. \end{aligned}$$

The last term can be neglected for small values of the damage variable d. Then the conjugated force Y is equal to the strain energy of the undamaged material. The damage accumulation is formulated as an explicit function

$$d = \tilde{d}(Y; Y_0, b1, b_2) = \frac{Y - Y_0}{Y} + b_1 \left(\frac{Y_0}{Y} - e^{-b_2(Y - Y_0)}\right) \tag{3.6}$$

of the damage conjugated force Y which contains three non-negative material parameters

$$Y_0 \geq 0, \qquad b_1 > 0, \qquad b_2 \geq 0. \tag{3.7}$$

The basis for the identification of the PBT material parameters are cyclic loading tests on pure PBT specimens which are explained in Chap. 6, see Fig. 3.9. Solely uniaxial tensile tests are considered in this section. Therefore, the isotropic hardening parameter r is identical with measured plastic strain ε_{p}, and the von Mises equivalent stress is given by $\sigma^{\text{eq}} \equiv \sigma$ in the spatial one-dimensional case, i.e. for the uniaxial tensile test. Each tensile test consists of several power-controlled loading-unloading cycles with increasing amplitudes. For cycle $k \in \{1, 2, \ldots, K\}$, the stress $\sigma^k = \sigma^k(t),\ t \in (T^{k-1}, T^k]$ is prescribed and $\varepsilon^k = \varepsilon^k(t),\ t \in (T^{k-1}, T^k]$ is measured (where $T^0 = 0$). Then (i) the maximum measured stress, (ii) the maximum measured total strain, (iii) the plastic strain, and (iv) the damage variable (see Fig. 3.10) are computed for each cycle $k \in \{1, 2, \ldots, K\}$:

$$\sigma^k_{\max} = \max_{t\in(T^{k-1},T^K]} \sigma^k(t), \qquad \varepsilon^k_{\max} = \max_{t\in(T^{k-1},T^K]} \varepsilon^k(t),$$

$$\varepsilon^k_p = \varepsilon^k(t = T^k), \qquad d^k = 1 - \frac{E^k_d}{E_e}.$$

The maximum elastic strain is taken as $\varepsilon^k_e := \varepsilon^k_{\max} - \varepsilon^k_p$. The corresponding data $(\sigma^k_{\max}, \varepsilon^k_e, \varepsilon^k_p, d^k)$ are listed in Table 3.2 for three testing speeds. The six unknown material parameters from (3.5), (3.7) and the unknown yield stress σ_y are computed by using the following fitting algorithm.

Algorithm 1: Parameter identification algorithm

Input : Young's modulus E_e, initial plastic strain ε^0_p

for $k \leftarrow 1$ **to** K **do**

  Compute effective stress $\bar{\sigma}^k = \frac{\sigma^k}{1-d^k}$

end

NLLS: fitting $\bar{\sigma} = \psi(r) = \tilde{\psi}(\varepsilon_p; \sigma_y, H_0, a_1, \delta)$ using data points $(\varepsilon^k_p, \bar{\sigma}^k)$

  Result: Plastic material parameter σ_y, H_0, a_1, δ

for $k \leftarrow 1$ **to** K **do**

  Compute the damage conjugated force $Y^k = W_{\text{elastic}}(\varepsilon^k_e) + W_{\text{iso}}(\varepsilon^k_p) = \frac{1}{2}E_e(\varepsilon^k_e)^2 + \tilde{W}_{\text{iso}}(\varepsilon^k_p; \sigma_y, H_0, a_1, \delta)$

end

NLLS: fitting $d = \tilde{d}(Y; Y_0, b1, b_2)$ using data points (Y^k, d^k)

  Result: Damage material parameters Y_0, b_1, b_2

Table 3.2 Measured material parameters

Testing speed v/(mm/s)	Young's modulus E/MPa	Cycle number k	Maximum stress $\sigma_{\max}$/MPa	Elastic strain ε_e/%	Plastic strain ε_p/%	Damage $d \in [0.1]$
0.1	2336	1	11.7	0.51	0.01	0.0
		2	22.4	1.02	0.03	0.03
		3	32.2	1.54	0.06	0.07
		4	40.7	2.05	0.09	0.11
		5	47.3	2.56	0.15	0.16
		6	50.7	3.07	0.28	0.22
		7	51.1	3.55	0.53	0.28
1.0	2385	1	11.2	0.49	0.02	0.0
		2	21.6	0.98	0.04	0.03
		3	31.4	1.48	0.05	0.08
		4	40.4	1.98	0.07	0.11
		5	47.8	2.48	0.11	0.16
		6	53.0	2.98	0.18	0.21
		7	54.5	3.38	0.34	0.25
10.0	2343	1	11.1	0.49	0.01	0.0
		2	21.7	0.99	0.05	0.01
		3	55.9	3.38	0.27	0.23
		4	56.2	3.74	0.46	0.27

3.3.1 Results

The determination of the Young's modulus and the Poisson's ratio for describing the the isotropic linear elastic behaviour of PBT is described in Chap. 6. The unknown parameters of the plastic yield $\psi = \tilde{\psi}(r; \sigma_y, H_0, a_1, \delta)$ function and the damage function $d = \tilde{d}(Y; Y_0, b1, b_2)$ are fitted by using a nonlinear least-squares (NLLS) Levenberg-Marquardt algorithm, see Algorithm 1. The initial plastic strain is zero at the testing speeds of 0.1 and 10.0 mm/s, whereas an initial plastic strain of 0.016% is estimated from the measurements at the testing speed of 1.0 mm/s. Furthermore, the parameter H_0 is set to zero for all testing speeds, because this parameter could not improve the fit of the hardening curve. The results of the parameter identification for three testing speeds are presented in Table 3.3. The good quality of the fits can be seen on Figs. 3.11, 3.12, 3.13, 3.14, 3.15 and 3.16. The Voce hardening parameter a_1

Table 3.3 Material parameter for the pure PBT polymer

Testing speed	v/(mm/s)	0.1	1.0	10.0
Elastic behaviour				
Young's modulus	E/MPa	2336	2385	2343
Poisson's ratio	ν	0.4	0.4	0.4
von Mises J_2-plasticity with isotropic hardening				
Initial yield stress	σ_Y/MPa	3.32	3.24	1.00
Linear hardening	H_0/MPa	0.0	0.0	0.0
Voce hardening	a_1/MPa	66.31	69.34	79.34
	δ	1123.6	1592.4	785.7
Isotropic damage				
Threshold	Y_0/MPa	0.063	0.072	0.038
Parameter 1	b_1	1.007	0.965	1.010
Parameter 2	b_2/MPa^{-1}	0.295	0.225	0.255

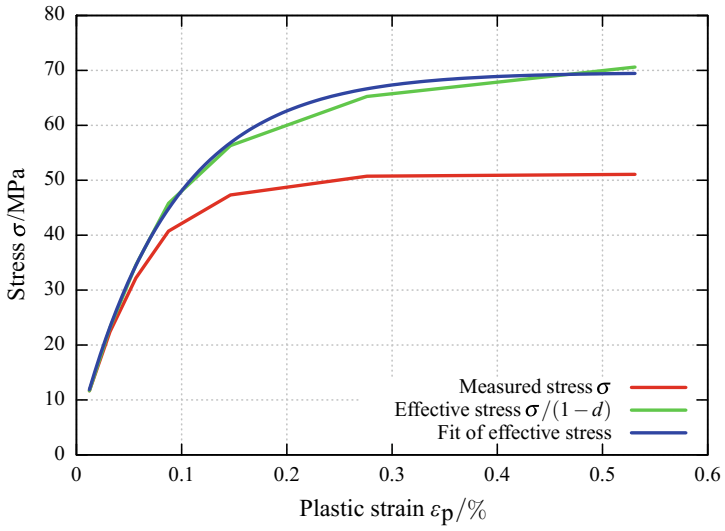

Fig. 3.11 Stress and effective stress as function of the plastic strain at a testing speed of 0.1 mm/s (first fit)

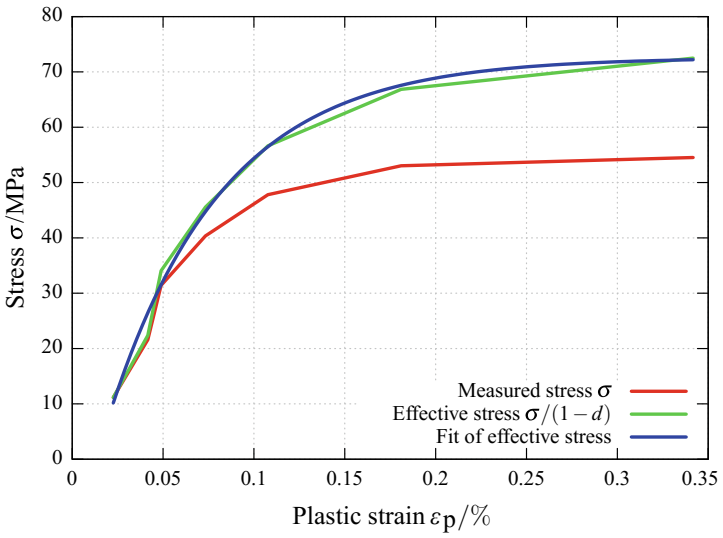

Fig. 3.12 Stress and effective stress as function of the plastic strain at a testing speed of 1.0 mm/s (first fit)

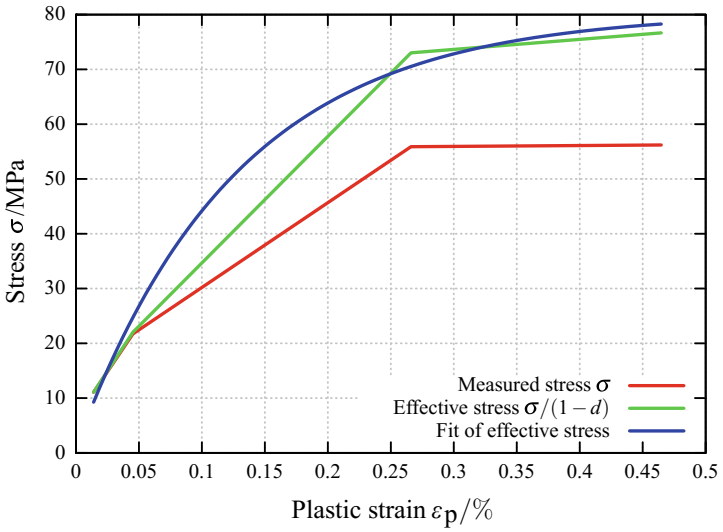

Fig. 3.13 Stress and effective stress as function of the plastic strain at a testing speed of 10.0 mm/s (first fit)

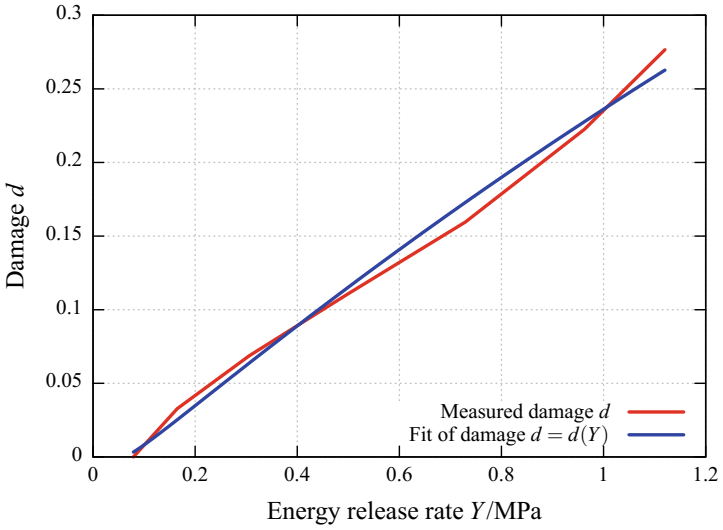

Fig. 3.14 Damage d as function of the energy release rate Y at a testing speed of 0.1 mm/s (first fit)

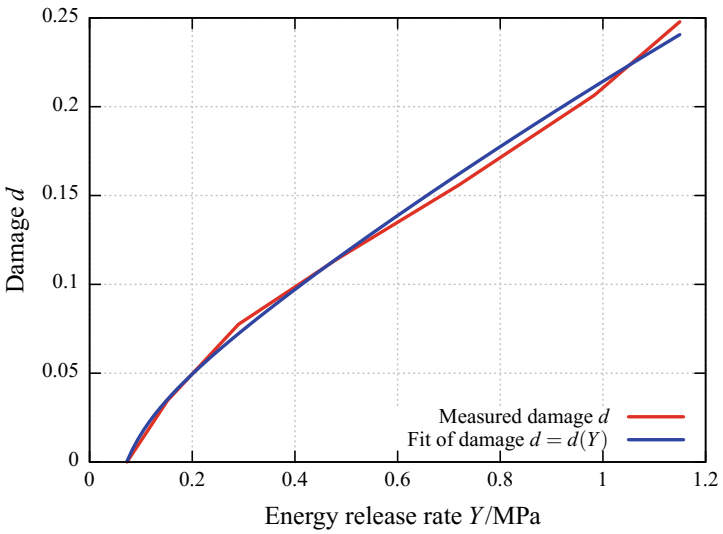

Fig. 3.15 Damage d as function of the energy release rate Y at a testing speed of 1.0 mm/s (first fit)

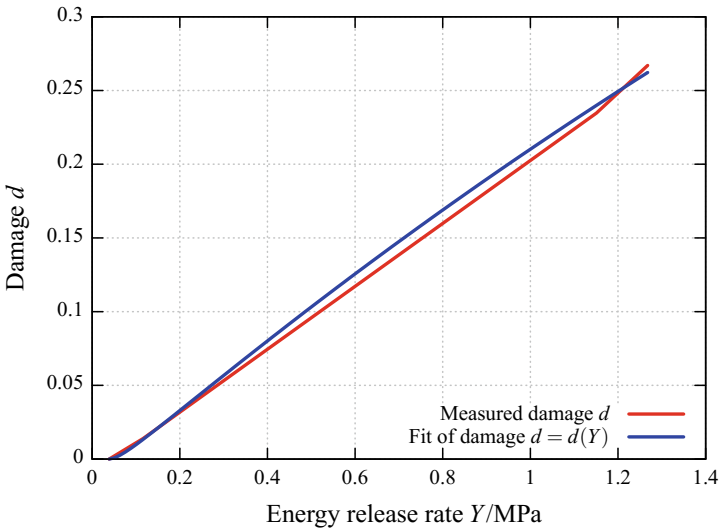

Fig. 3.16 Damage d as function of the energy release rate Y at a testing speed of 10.0 mm/s (first fit)

is increasing with the testing speed. The damage parameters are almost identical. The hardening curves are fitted very well also for very small plastic strains. However, the computed yield stress σ_y is also very small. Therefore, in the second fitting the initial yield stress σ_y is increased to 32.0 MPa, where the value is related to a plastic strain of about 0.05%, and only the remaining material parameters are fitted. At $\sigma = 32.0$ MPa the plastic strain is still below the value R_{p02}, which is usually used as initial yield stress for metallic materials. The initial plastic strain is set to zero for all testing speeds. The resulting elastoplastic material parameters of the second fit are presented in Table 3.4 and in Fig. 3.17. The Voce hardening parameter a_1 is increasing with the testing speed as in the first fit. The second fit of the plastic parameters can be used if small plastic strains are not of interest, see Fig. 3.17. Finally, the cyclic tensile tests are simulated by taking the identified material parameters from Table 3.3 (first fit) and Table 3.4 (second fit). The results of the first and second fit are visualised in Figs. 3.18 and 3.19 for the testing speed of 0.1 mm/s as well as in Figs. 3.20 and 3.21 for the testing speed of 10.0 mm/s. For both

Table 3.4 Material parameter for the pure PBT polymer

Testing speed	v/(mm/s)	0.1	1.0	10.0
von Mises J_2-plasticity with isotropic hardening				
Initial yield stress	σ_Y/MPa	32.0	32.0	32.0
Linear Hardening	H_0/MPa	0.0	0.0	0.0
Voce hardening	a_1/MPa	39.96	43.56	45.45
	δ	642.6	819.0	876.12

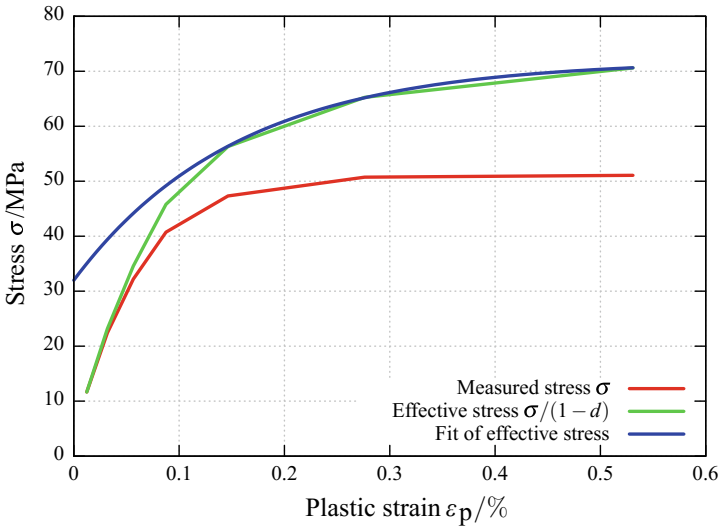

Fig. 3.17 Stress and effective stress as function of the plastic strain at a testing speed of 0.1 mm/s (second fit)

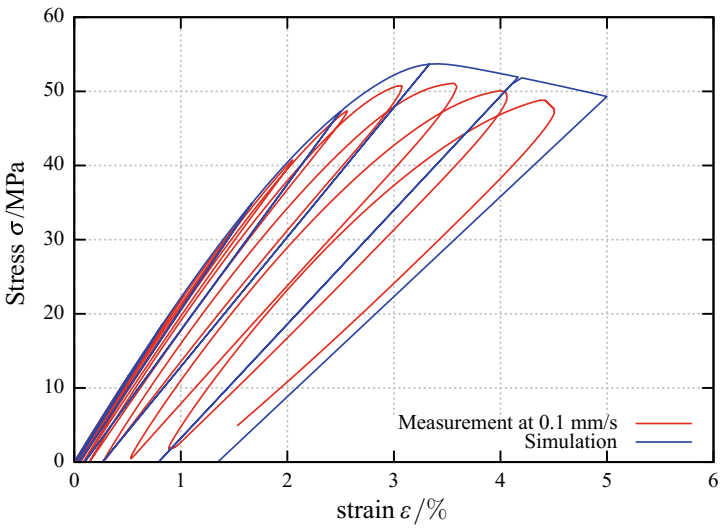

Fig. 3.18 Simulation and measurements of cyclic tensile tests, testing speed 0.1 mm/s (first fit)

testing speeds, there is no essential difference between the simulation results using the plastic material parameters obtained from the first fit or second fit, respectively. A detailed sensitivity analysis for every material parameter is outside the scope of this section. The hysteresis loops (see Figs. 3.18, 3.19, 3.20 and 3.21) due to the viscoelastic behaviour of the PBT polymer are not captured by the time-independent elastoplastic material model with damage which is considered in this section.

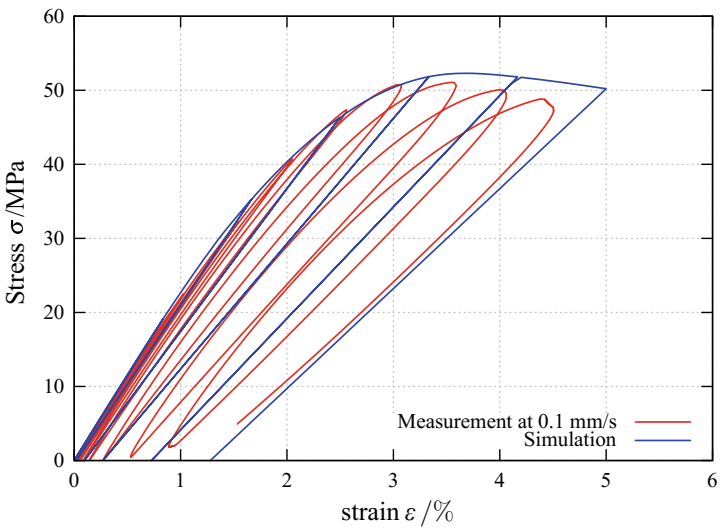

Fig. 3.19 Simulation and measurements of cyclic tensile tests, testing speed 0.1 mm/s (second fit)

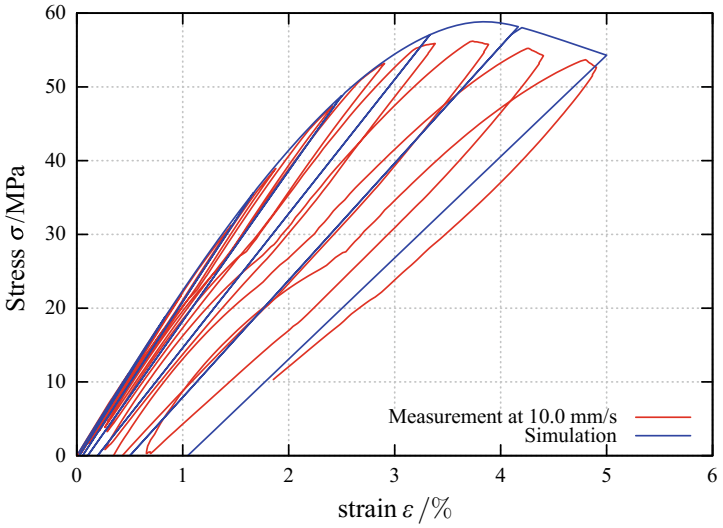

Fig. 3.20 Simulation and measurements of cyclic tensile tests, testing speed 10.0 mm/s (first fit)

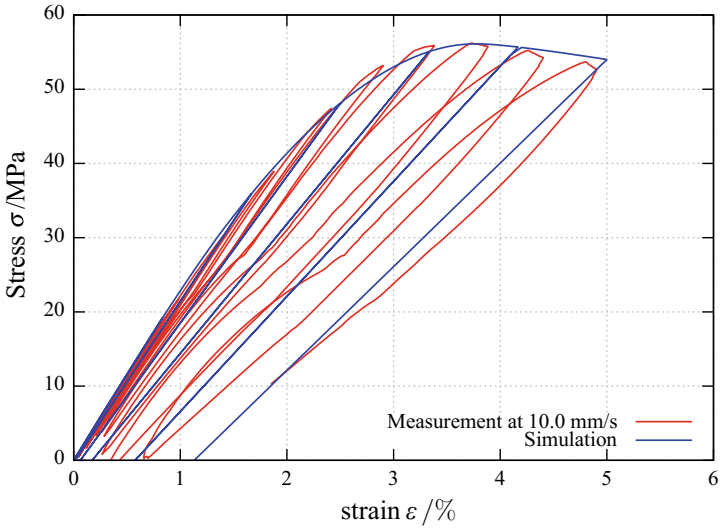

Fig. 3.21 Simulation and measurements of cyclic tensile tests, testing speed 10.0 mm/s (second fit)

3.4 Numerical Solution of Periodic Boundary Problems for Damage Coupled to Elastoplasticity

In the following the governing equations of a periodic boundary value problem and their reformulation in terms of the Lippmann-Schwinger (LS) integral equations are briefly reviewed. Subsequently, the numerical solution of the periodic boundary value problem by application of fast Fourier transforms is outlined.

3.4.1 Formulation of the Periodic Boundary Value Problem

For the computation of the microscopic deformation a periodic boundary value problem (BVP) on a representative volume element (RVE) ω is considered. At the boundary $\partial\omega$ of the RVE an effective strain ε^M is applied. The kinematics for the unknown strains depending on the displacements $\mathbf{u}$ and the fluctuations $\mathbf{u}^*$ are given as

$$\left.\begin{aligned} \varepsilon(\mathbf{u})(\mathbf{x}) &= \varepsilon^M + \varepsilon(\mathbf{u}^*)(\mathbf{x}) \\ \varepsilon(\mathbf{u}^*)(\mathbf{x}) &= \tfrac{1}{2}\left(\operatorname{grad}\mathbf{u}^*(\mathbf{x}) + \operatorname{grad}^T\mathbf{u}^*(\mathbf{x})\right) \end{aligned}\right\} \mathbf{x} \in \omega. \tag{3.8}$$

At the boundary of the domain the following (anti-)periodic boundary conditions are prescribed in terms of the Cauchy stress σ as

$$\left.\begin{aligned} \mathbf{u}^*(\mathbf{x}) &\quad \# \\ \sigma(\mathbf{x})\cdot\mathbf{n} &\quad -\# \end{aligned}\right\} \mathbf{x} \in \partial\omega. \tag{3.9}$$

Therein, # and $-$# denote periodicity or anti-periodicity, respectively. Therefore, the fluctuations at opposite faces of the RVE are equal, whereas the tractions have the same magnitude but point into opposite directions.

The equilibrium condition for the stresses read

$$\operatorname{div}\sigma(\mathbf{x}) = \mathbf{0}, \ \ \mathbf{x} \in \omega. \tag{3.10}$$

The formulation of the BVP is completed by the constitutive functional $\mathscr{F}$, which connects the stresses to the strains and the history of the material via

$$\sigma(\mathbf{x}) = \mathscr{F}\left[\varepsilon(\mathbf{x}), \varepsilon_p(\mathbf{x}), r(x), d(\mathbf{x})\right]. \tag{3.11}$$

According to Sect. 3.3, ε_p denotes the plastic strains and d the damage variable.

In a next step, the differential equation (3.10) for the stress equilibrium is reformulated into the so-called Lippmann-Schwinger integral equation, see [10], according to [23]. To this end the polarisation tensor τ is defined as

$$\tau(\mathbf{x}) = \sigma(\mathbf{x}) - \mathbb{C}^0 : \varepsilon(\mathbf{x}), \tag{3.12}$$

by introduction of a constant homogeneous reference stiffness tensor $\mathbb{C}^0$. The solution of the local equilibrium equation (3.10) can then be obtained by application the non-local Green's operator Γ^0 applied to the stress polarisation

$$\varepsilon(\mathbf{x}) = \varepsilon^M - \left(\Gamma^0 * \tau\right)(\mathbf{x}). \tag{3.13}$$

The Green's operator depends only on the homogeneous reference stiffness and the applied boundary conditions, and thus is independent of the strain fluctuations, see [9]. The convolution operator $*$ in equation (3.13) is defined as

$$\left(\Gamma^0 * \tau\right)(\mathbf{x}) = \int_{\omega} \Gamma^0(\mathbf{x} - \mathbf{y}) : \tau(\mathbf{y})\, \mathrm{d}\mathbf{y}. \tag{3.14}$$

Finally, the nonlinear Lippmann-Schwinger integral equation is obtained as

$$\varepsilon^M = \varepsilon(\mathbf{x}) + \Gamma^0 * \left(\mathscr{F}\left[\varepsilon, \varepsilon_p, d\right] - \mathbb{C}^0 : \varepsilon\right)(\mathbf{x}). \tag{3.15}$$

Please note, that the Green's operator Γ^0 is independent of the fluctuations and therefore only depends on the linear elastic reference stiffness as well as on the boundary conditions, see [9]. In order to further simplify the notation in the following the LS equation is rewritten by application of the operator B_ε as

$$\varepsilon^M = \left((I + B_\varepsilon)\,\varepsilon\right)(\mathbf{x}). \tag{3.16}$$

Therein I denotes the identity operator δ_{ij}, where $\delta_{ij} = 1$ if $i = j$ and $\delta_{ij} = 0$ otherwise. The numerical solution of equation (3.16) is outlined in the following.

3.4.2 Numerical Solution of Lippmann-Schwinger Equation via Fast Fourier Transforms

The numerical solution of the LS integral equation as given in (3.16) can be obtained iteratively by using the Neumann series expansion for inverting the operator $I + B_\varepsilon(\mathbf{x})$. Thus, the iterates of the local strains are obtained as

$$\varepsilon^0(\mathbf{x}) = \varepsilon^M \tag{3.17}$$

$$\varepsilon^{k+1}(\mathbf{x}) = -B_\varepsilon(\mathbf{x})\varepsilon^k(\mathbf{x}) + \varepsilon^M,\ k = 0, 1, 2, ... \tag{3.18}$$

These iterates can be computed efficiently by the so-called basis scheme as proposed by Moulinec and Suquet [11] for linear elastic material behaviour. An extension towards the account of nonlinear material behaviour is given by Moulinec and Suquet in [12].

The basis scheme consists of the following steps, which are repeated until convergence is reached:

1. Solve the constitutive equation in the real space and compute the stress polarisation
$$\tau^k = \sigma - \mathbb{C}^0 : \varepsilon.$$
2. Transformation of the stress polarisation into the Fourier space
$$\hat{\tau}^k = \mathrm{FFT}\left(\tau\right).$$
3. Update the strain field in the Fourier space by application of the Green's operator
$$\hat{\varepsilon^{k+1}} = -\hat{\Gamma}^0 : \hat{\tau}^k.$$
4. Inverse Fourier transformation of the updated strain field
$$\varepsilon^{k+1} = \mathrm{FFT}^{-1}\left(\hat{\varepsilon^{k+1}}\right).$$

Explicit expressions for the Green's operator can be found e.g. in Mura [13]. Alternative solution schemes to the basis scheme which are also applicable to large deformations are summarised in Kabel et al. [7].

3.5 Computational Homogenisation

In the following the computational homogenisation scheme connecting the microscopic and the macroscopic scale is outlined. Here, focus is put onto classical first order homogenisation schemes, see e.g. [8] for details. Basically, the computational homogenisation scheme consists of the following four steps:

1. Generation of a representative volume element (RVE), see Sect. 3.2, and determination of the constitutive behaviour and material parameters of all phases.
2. Selection of admissible microscopic boundary conditions based on macroscopic input quantities.
3. Solution of microscopic boundary value problem (according to Sect. 3.4).
4. Determination of macroscopic output variables in terms of averaged microscopic quantities.

Here, the macroscopic variables are denoted by the index M. The effective macroscopic quantities, stresses or strains respectively, are obtained by averaging the corresponding microscopic solution fields over the volume $\|\omega\|$ of the RVE ω

$$\sigma^M = \frac{1}{|\omega|} \int_\omega \sigma \, \mathrm{d}v \tag{3.19}$$

$$\varepsilon^M = \frac{1}{|\omega|} \int_\omega \varepsilon \, \mathrm{d}v. \tag{3.20}$$

In the numerical examples given in the next section, so called mixed boundary conditions are prescribed to the RVE in order to reconstruct the performed experiments. In case of these boundary conditions macroscopic periodic strains ε^M are prescribed in loading direction (here 0° or 90°) and the other boundaries are stress-free. The effective stiffness in loading direction is then computed as the ratio of the macroscopic strain and stress in the corresponding loading direction.

3.6 Numerical Examples

In the following the results for the purely elastic and the elasto-plastic simulations are given and compared to the experimental data from Chap. 6.

In a first step the elastic behaviour is addressed. Therefore, the PBT matrix is modelled as an isotropic linear elastic material ($E = 2470$ MPa, $\nu = 0.4$). The PBT matrix is reinforced by 20% (weight) linear elastic glass fibres with a Young's modulus of 73,400 MPa and a Poisson's ratio 0.22. The simulations are carried out on the highly resolved (1024^3 voxels) virtual samples from Sect. 3.2. Mixed boundary conditions as described in Sect. 3.5 are applied.

In Fig. 3.22 the simulations and the experimental data are compared for the slowest measured loading. For the simulation of the 90° direction the simulation reflects the measurements well for all 5 regarded samples. In 0° direction the simulation underestimates the stiffness of the composite lightly for all regarded specimens.

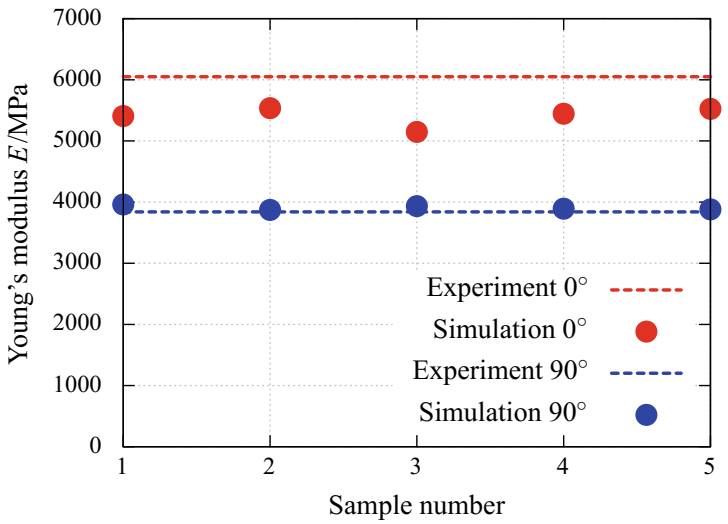

Fig. 3.22 Comparison of simulation and measurement for elastic composite behaviour, Samples 1–5

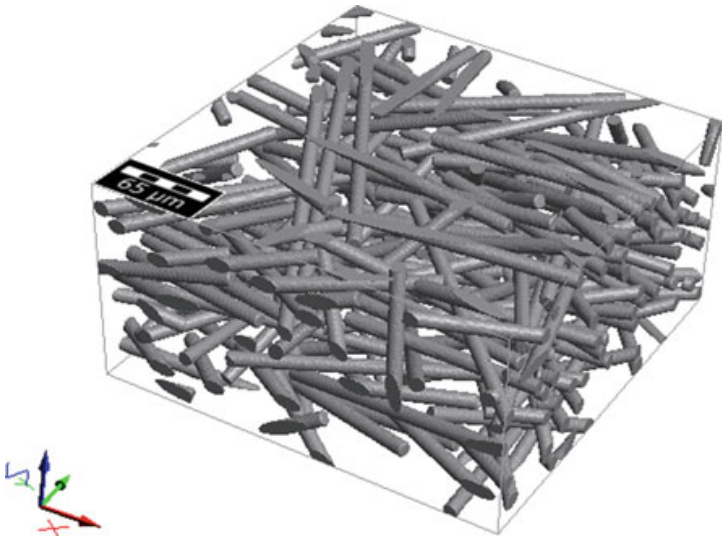

Fig. 3.23 RVE for elasto-plastic simulation, size 512 × 512 × 256 voxel

Nevertheless, from Fig. 3.22 it is concluded that the simulations are in good coincidence with the experimental data. For all realisations similar results are obtained which is connected to the representativeness of the regarded volume elements.

A big advantage of the applied micromechanical approach is that not only the effective quantities like stresses σ^M and strains ε^M are available, but also the local fields in the RVE. In a next step the simulation of the elasto-plastic PBT model including damage is addressed. For this non-linear material behaviour a much higher resolution of the fibres is required. Therefore, only the upper layer of the multi-layered microstructure is considered, see Fig. 3.23. Herein, the fibres are resolved by 16 voxels over their thickness, i.e. the voxel size is chosen as 0.625 µm.

The effective elastic stiffnesses of this one-layered RVE result in $E_0^M = 5301$ MPa for the 0° direction and $E_{90}^M = 3920$ MPa for the 90° direction. Compared to the average stiffness of the layered RVE ($\bar{E}_0^M = 5412$ MPa and $\bar{E}_{90}^M = 3907$ MPa) and the experimental values ($E_0 = 6050$ MPa and $E_{90} = 3840$ MPa) very good results are obtained with the considered one-layered RVE.

For the elasto-plastic simulation the material parameters of the PBT matrix are chosen according to Table 3.4 for the plastic contribution and Table 3.3 for the damage. The simulation results for a loading and unloading scenario are depicted in Fig. 3.24. For the 90° direction very good coincidence of the simulation and the measurement are archived. For the 0° direction the simulation underestimates the stresses, which follows from the fact that for the considered RVEs also the elastic response yields lower stresses than the experiments.

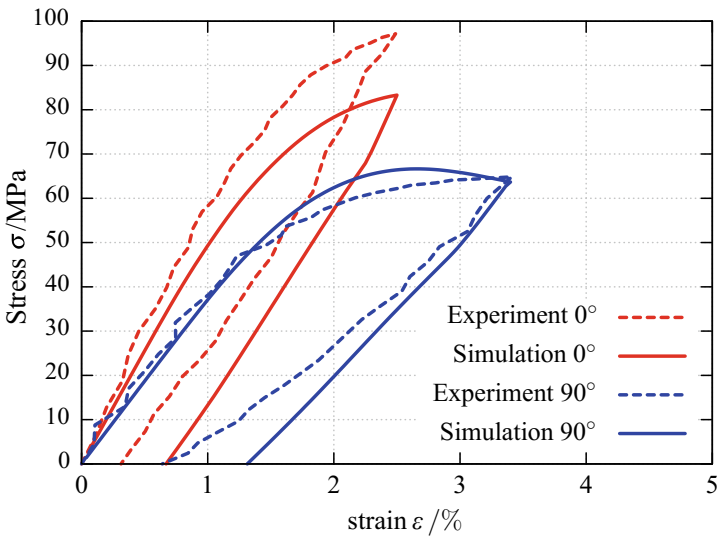

Fig. 3.24 Comparison of simulation and experiment for elasto-plastic model including damage

3.7 Conclusion

In summary, this section explains how the nonlinear behavior of the composite can be simulated in an RVE using only the material characterization of the pure polymer and the morphology of the microstructure.

Mechanical tests on the composite are not required.

References

1. Baur, E., Osswald, T.A., Rudolph, N., Brinkmann, S., Schmachtenberg, E. (eds.): Saechtling Kunststoff Taschenbuch, 31st edn. Hanser (2013)
2. Fisher, N., Lewis, T., Embleton, B.: Statistical Analysis of Spherical Data. Cambridge University Press, Cambridge, UK (1987)
3. Frangi, A., Niessen, W., Vincken, K., Viergever, M.: Multiscale vessel enhancement filtering. In: Proceedings of the Medical Image Computing and Computer-Assisted Intervention, pp. 130–137 (1998)
4. Fraunhofer ITWM, Department of Image Processing: MAVI—modular algorithms for volume images. http://www.mavi-3d.de (2005)
5. GeoDict.: www.geodict.com. Accessed 16 Jan 2019
6. Ju, J.: On energy-based coupled elastoplastic damage theories: constitutive modeling and computational aspects. Int. J. Solids Struct. **25**(7), 803–833 (1989)
7. Kabel, M., Böhlke, T., Schneider, M.: Efficient fixed point and Newton-Krylov solvers for FFT-based homogenization of elasticity at large deformations. Comput. Mech. **54**(6), 1497–1514 (2014)
8. Kouznetsova, V., Brekelmans, W., Baaijens, F.: An approach to micro-macro modeling of heterogeneous materials. Comput. Mech. **27**(1), 37–48 (2001)
9. Kröner, E.: Bounds for effective elastic moduli of disordered materials. J. Mech. Phys. Solids **25**(2), 137–155 (1977)
10. Lippmann, B., Schwinger, J.: Variational principles for scattering processes. Phys. Rev. **79**, 469–480 (1950)

11. Moulinec, H., Suquet, P.: A fast numerical method for computing the linear and nonlinear mechanical properties of composites. Comptes rendus de l'Académie des sciences. Série II, Mécanique, physique, chimie, astronomie **318**(11), 1417–1423 (1994)
12. Moulinec, H., Suquet, P.: A numerical method for computing the overall response of nonlinear composites with complex microstructure. Comput. Methods Appl. Mech. Eng. **157**(1–2), 69–94 (1998)
13. Mura, T.: Micromechanics of Defects in Solids, 2nd, revised edn. Mechanics of Elastic and Inelastic Solids. Martinus Nijhoff Publishers, Dordrecht (1987)
14. Niedziela, T., Strautins, U., Hosdez, V., Kech, A., Latz, A.: Improved multiscale fiber orientation modeling in injection molding of short fiber reinforced thermoplastics: simulation and Experiment. Int. J. Multiphys. Special Edition: Multiphys. Simul. Adv. Methods Ind. Eng. 357–366 (2011)
15. Ohser, J., Schladitz, K.: 3D Images of Materials Structures: Processing and Analysis. Wiley VCH (2009)
16. Onate, E. (ed.): Multiscale modeling of progressive damage in elasto-plastic composite materials (2014)
17. Otsu, N.: A threshold selection method from gray level histograms. IEEE Trans. Syst. Man Cybern. **9**, 62–66 (1979)
18. Schneider, R., Weil, W.: Stochastic and Integral Geometry. Probability and Its Applications. Springer, Heidelberg (2008)
19. Spahn, J., Andrä, H., Kabel, M., Müller, R.: A multiscale approach for modeling progressive damage of composite materials using fast Fourier transforms. Comput. Methods Appl. Mech. Eng. **268**, 871–883 (2014)
20. Stoyan, D., Kendall, W., Mecke, J.: Stochastic Geometry and Its Applications, 2nd edn. Wiley, Chichester (1995)
21. Wirjadi, O.: Models and algorithms for image-based analysis of microstructures. Ph.D. thesis. Technische Universität Kaiserslautern (2009)
22. Wirjadi, O., Schladitz, K., Easwaran, P., Ohser, J.: Estimating fibre direction distributions of reinforced composites from tomographic images. Image Anal. Stereol. **35**(3), 167–179 (2016)
23. Zeller, R., Dederichs, P.H.: Elastic constants of polycrystals. Phys. Status Solidi (b) **55**(2), 831–842 (1973)

Composites Science and Technology 183 (2019) 107786

Contents lists available at ScienceDirect

Composites Science and Technology

journal homepage: www.elsevier.com/locate/compscitech

Local fiber orientation from X-ray region-of-interest computed tomography of large fiber reinforced composite components

Thomas Baranowski[a], Dascha Dobrovolskij[b,c], Kilian Dremel[d], Astrid Hölzing[d], Günter Lohfink[e], Katja Schladitz[c,*], Simon Zabler[d]

[a] Ford Research and Innovation Center Aachen, Ford-Werke GmbH, Germany
[b] Hochschule Darmstadt, Schöfferstraße 3, 64295, Darmstadt, Germany
[c] Fraunhofer-Institut für Techno-und Wirtschaftsmathematik, Fraunhofer-Platz 1, 67663, Kaiserslautern, Germany
[d] Fraunhofer-Entwicklungszentrum Röntgentechnik, Josef-Martin-Weg 63, 97074, Würzburg, Germany
[e] Montaplast GmbH, Morsbach, Germany

ARTICLE INFO

Keywords:
Non-destructive testing
Glass fiber reinforced polymers
Fiber orientation distribution
Second order orientation tensor
Injection molding

ABSTRACT

The local fiber orientation is a micro-structural feature crucial for the mechanical properties of parts made from fiber reinforced polymers. It can be determined from micro-computed tomography data and subsequent quantitative analysis of the resulting 3D images. However, although being by nature non-destructive, this method so far has required to cut samples of a few millimeter edge length in order to achieve the high lateral resolution needed for the analysis.

Here, we report on the successful combination of region-of-interest scanning with structure texture orientation analysis rendering the above described approach truly non-destructive. Several regions of interest in a large bearing part from the automotive industry made of fiber reinforced polymer are scanned and analyzed. Differences of these regions with respect to local fiber orientation are quantified. Moreover, consistency of the analysis based on scans at varying lateral resolutions is proved. Finally, measured and numerically simulated orientation tensors are compared for one of the regions.

1. Introduction

Many structural components in the automotive and aircraft industries are made from fiber reinforced plastic (FRP) composite material. The fibers can be made of glass, carbon, or other materials, they can be short cut, long or even continuous, of various thicknesses and volume concentrations. Typically, the fiber component comprises 10–35% of the volume for injection molded materials [1] and up to 50–60% for laminar FRP [2–5] and consists of 6–15 μm thick carbon fiber bundles or 10–18 μm thick glass fibers (e. g. 10 μm in [1], 12 μm in [6], 18 μm in [7]).

When the components are molded, usually thermoplastics like polypropylene [8], polybutylene terephthalate [6], polyamide 66 [9], polyamide 6, acrylonitrile butadiene styrene are used as host material to which the fibers are added. Since FRP components generally undergo mechanical and/or thermal stresses during their service life, their load bearing capacity/strength is of critical importance for the components' design.

The structural properties of injection molded FRP materials are locally anisotropic due to the fiber component being anisotropically oriented [9–11] (for short fibers), [12] (for long fibers). This anisotropy in turn is caused by the fibers moving with the liquid flow in the mold [13]. For complex shaped parts, the resulting fiber orientations are difficult to predict and control. As a consequence, structurally weak spots or areas can appear and may lead to early failure of the component. In order to avoid this, components are often designed too thick. This in turn thwarts the weight saving intention in using FRP.

Numerical simulations can predict the liquid flow [14] and thus indicate critical areas where material weaknesses might occur. Yet, these simulations are not perfect and need validation. Moreover, prediction of the local materials properties relies on orientation information as input, typically in the form of the 2nd order orientation tensor [10].

Fiber orientations can be analyzed essentially by four types of methods. Historically, before X-ray micro computed tomography (μCT) became widely available, fiber orientations were evaluated through image analysis of polished 2D sections. See [[15], Section 11.6.4] for a summary of stereological methods based on counting intersections in

* Corresponding author. Fraunhofer-Institut für Techno- und Wirtschaftsmathematik, Fraunhofer-Platz 1, 67663 Kaiserslautern, Germany
E-mail address: katja.schladitz@itwm.fraunhofer.de (K. Schladitz).

https://doi.org/10.1016/j.compscitech.2019.107786
Received 22 February 2019; Received in revised form 15 August 2019; Accepted 22 August 2019
Available online 25 August 2019
0266-3538/

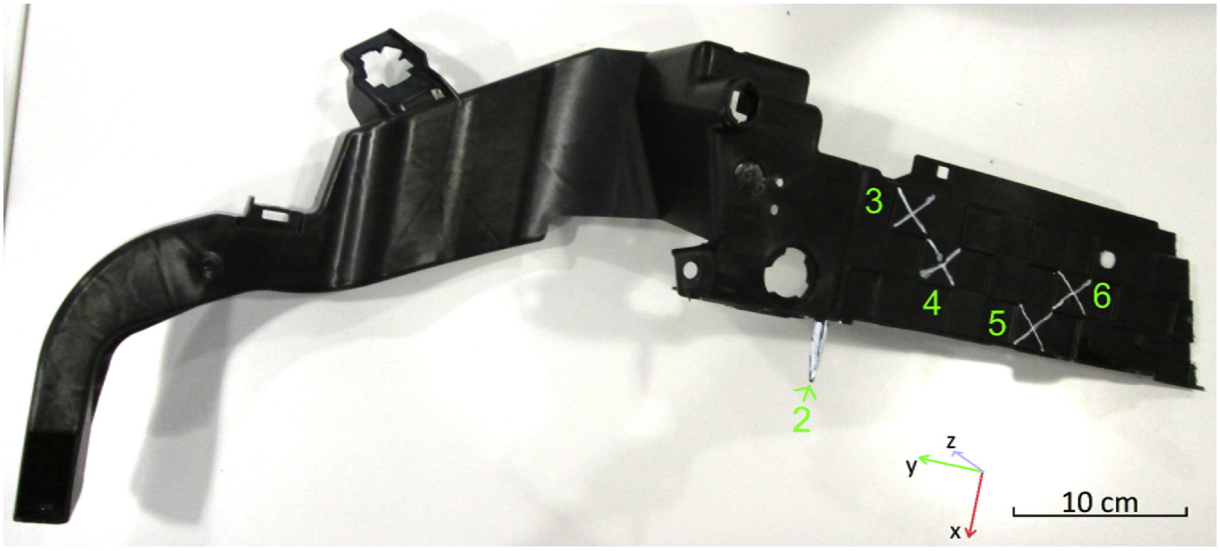

Fig. 1. Bearing component made of polypropylene with 30 wt% reinforcing long glass fibers. Regions of interest (RoI) are marked white. As indicated, the analyzed component is mostly oriented in the x-y-plane and positive z is the thickness direction. Throughout, this coordinate system is used.

slices at varying angles and [16,17] for orientations deduced from the shape of the observed elliptical cross-sections. These methods are not only destructive but the latter suffers also from the need for rather high resolutions and ambiguities due to the fact that there are always two 3D orientations generating the same cross-sectional ellipse. Therefore, critical areas of damaged/failed thermoplastic parts (or field returns) are nowadays predominantly analyzed by CT techniques, nevertheless for detailed verification optical microscopy of polished micro-sections is still commonly used.

X-ray micro computed tomography (μCT) can be employed to analyze non-destructively the fiber orientation in structural components. Based on the resulting three-dimensional images, fiber orientations can be analyzed for the whole field of view (FoV) by the mean intercept length (MIL [13]) or by measuring the length of generalized projections and obtaining the orientation distribution via the inverse cosine transform [[18], Section 5.4]. Both methods are designed to be applied to the whole FoV, they can however be localized by applying them to small sub-volumes. Nevertheless, in order to get an orientation in each voxel, one would have to center the sub-volume in each voxel. While inverting the cosine transform faces numerical instabilities, the MIL method has been applied successfully, see [13] also for a comparison to analysis of 2D virtual slices from the CT data as well as of 2D images of polished surfaces.

Local fiber orientation can of course be determined via single fiber segmentation. These approaches are typically very demanding with respect to image quality (contrast as well as lateral resolution), fiber volume fraction and spatial arrangement of the fibers. On the other hand, if successful they yield additional valuable information, in particular the fiber length distribution [19,20] or positions with respect to failure regions [21]. Single fiber segmentation usually relies on tracking fiber center lines or cross-sections from slice to slice [2,5] or local approximation of fibers by line segments [22,23], ellipsoids [24], or cylinders [25–27]. [24] reconnects fragments based on local orientation, while [25,26] just use the fragment orientations. All these approaches have in common that they demand rather slow orientation changes within one fiber (see the detailed discussion in [21]) and the fiber diameter to be resolved by at least 8 voxels. Viguié [28] and Kronenberger [21] do not need the former but [28] thrives on high image quality as provided by tomography using synchrotron radiation and both rely on resolutions of 8 voxels per fiber diameter and more. Pinter [27] claims 5 voxels per diameter to be sufficient, whereas the efficiency of the circular voting filter drops significantly for the lower resolution of 3 voxels per fiber diameter. In [9], orientations of short fibers or clusters of them are used to derive the homogenized orthotropic behaviour for cuboidal sub-volumes for use in FEM simulations.

Here, we concentrate on estimation of the local fiber orientation in the sense of assigning an orientation vector to each voxel belonging to the fiber system without fiber separation. For this purpose, several methods based on local approximation of fibers by ellipsoids [29–31] and on local gray value derivatives of first [32] and second order [33] have been proposed. The first order gray value derivatives are subsumed into the so called structure tensor and are applied e. g. in [34] and in VG STUDIO MAX, see e. g. [35]. Note that the structure tensor is not the orientation tensor as described in [10] and given in Equation (1) below. The second order derivatives form the so called Hessian matrix and are applied e. g. in MAVI [8]. The rationale behind both methods is that locally the fiber orientation is the one in which gray values change or are curved the least. In [33], all four methods are compared comprehensively based on simulated single fibers with a diameter of 10 voxels. In applications, the derivative based methods usually use 2–4 voxels per diameter [7,8,20,33] while [30] rather demands 10. An exception is [34] applying the structure tensor at fiber bundle instead of fiber level thus allowing for voxel sizes of 50 μm. In [36], the authors present a different technique, the dark field scanning, for derivation of fiber orientation results in FRP. This method allows for even coarser resolutions of 86 μm.

All local and single fiber based orientation analysis methods described above except [34,36] require the fiber diameter to be sampled by at least 2–4 voxels [8,37,38]. Sampling the fibers coarser than this causes them to crumble in the digital image. That is, a fiber sampled at less than 2 voxels for its diameter is endangered to form more than one connected component. Thus, similar to the microscopic imaging of planar sections - μCT is limited in its FoV to some mm^3. E. g., if glass fibers of diameter 10 μm are analyzed, orientation analysis limits the voxel size to at most 5 μm and consequently the FoV to 10 μm/3×2 048≈7 mm size. This FoV usually covers the component's thickness. However, the lateral dimensions of injection molded parts can be as large as some meters. So far, we used CT to analyze fiber orientations in small molded parts. These results have been used to verify simulation results of injection molding simulation software. Large molded parts could not be analyzed due to the limitations of CT devices used in the polymer industry. The part analyzed in this paper, shown in Fig. 1, is about 1 m long.

As a consequence, very often the sample size is reduced to match the

FoV determined by the needed resolution by cutting small pieces of a few millimeters edge length from the part thereby rendering μCT an utterly destructive inspection technique [9,39].

With this work we demonstrate two strategies which aim at employing μCT for fully non-destructive analysis of local fiber orientation in injection molding FRP parts:

1. The imaging technique is applied as region of interest CT (RoI CT) [40]. That is, the components are not cut and the FoV can be significantly smaller than the components size, at least in one dimension.
2. Instead of the local fiber orientation distribution, a local "texture orientation" is derived. More precisely, the local orientation is determined in small cubic sub-volumes (boxes). Boxes not containing enough voxels belonging to the fiber component are not taken into account. Thus, the spatial sampling of the fiber diameter can be reduced to less than one voxel, allowing for an FoV 10 times larger than required for a local fiber orientation analysis.

By combining these two aspects into one novel method the analysis of local fiber orientation in meter-sized glass FRP components becomes readily feasible.

While in synchrotron μCT experiments RoI (axial or laminography) scans are performed routinely on carbon FRP material [41] this acquisition mode is still new in laboratory μCT. One reason for this is the compactness of commercial μCT scanners which, given a high geometric magnification, leave little to no space between X-ray source window and sample. The present scanner uses a variable source-detector distance which allows for RoI CT in samples of 100 mm width while maintaining a high magnification and microscopic voxel sampling.

2. Materials and methods

The object used to demonstrate our technique is a long glass fiber composite carrier, see Fig. 1. Built into the upper front end of the car, this part fulfills several functions: It carries the hood damper and yields mounting points for the lights as well as for the radiator package. The latter is provided with air by the carrier, too. Moreover, jointly with the crash absorber, the carrier contributes to fulfilling the legal regulations w.r.t. pedestrian protection.

In a polypropylene matrix, 30 wt% glass fibers of 10–20 μm thickness and 10–15 mm length before processing are embedded. The carrier has been scanned several times with different parameters. Thus, data has been acquired at several resolutions revealing different local features of the particular regions. The scanned regions were chosen to evaluate the effect of flow on fiber orientations along the part. Table 1 summarizes physical and digital sizes of the scans. The largest analyzed RoI scan A3.1 was scanned at the coarse resolution of 44 μm/voxel edge by the Tomosynthesis scanner at a the Fraunhofer Institute in Fürth (EZRT), Germany. This scanner has a maximum source-detector distance of 2 m, while its detector has 100 μm pixel pitch thus the scanner does not allow for very fine voxel samplings (< 5 μm) while maintaining a large source-object distance (in the present case at least 100 mm). We therefore used the metRIC scanner at EZRT Würzburg for the remaining scans. The metRIC allows for voxel samplings down to 2.33 μm with 100 mm source-object distance thanks to its very large detector X-axis (up to 3.3 m) and a pixel pitch of 74.8 μm. Thus, metRIC allows for higher resolutions while coping with large size of the scanned component. So that, we scanned the RoI A2, A4 and A5 at higher resolutions of 10–20 μm/voxel edge. In order to compare the local analysis at several resolutions, the region A3.2, has been imaged at coarse (45 μm/voxel, A3.2m), intermediate (21 μm/voxel, A3.2h), and high resolutions (10 μm/voxel, A3.2uh). The scans A3.2m, A3.2h and A3.2uh have been acquired by changing exclusively the source-object-distance/source-detector- distance leading to the corresponding dimensions of the scanned RoI. Finally, RoI A3.3 has been scanned at the highest resolution of 3 μm/voxel edge. Next, we describe the CT-data acquisition set-ups. Afterwards, we present the orientation analysis results for the CT-data and compare them with Moldflow® simulations.

Table 1
RoI scanned at varying resolutions.

RoI	CT device	dimensions in x-y-plane [cm^2]	voxels	voxel size [μm]
A2	MetRIC	2.7 × 0.9	604 × 200 × 205	45
A3.1	Tomosyn	6.2 × 4.8	1 422 × 1 102 × 450	44
A3.2m	MetRIC	4.9 × 2.5	1 084 × 556 × 172	45
A3.2h	MetRIC	2.0 × 1.4	949 × 686 × 307	21
A3.2uh	MetRIC	1.0 × 0.7	972 × 726 × 543	10
A3.3	MetRIC	0.6 × 2.3	1 944 × 8 832 × 1 944	3
A4	MetRIC	3.0 × 1.9	1 860 × 1 150 × 360	17
A5	MetRIC	5.2 × 5.6	1 210 × 1 300 × 250	44

2.1. X-ray approach for entire components (RoI CT)

RoI CT of large glass FRP components requires certain degrees of freedom in the CT scanner as well as sufficient space for displacement of the sample. This is realized in the Tomosynthesis scanner. The scanner allows for precise x, y, and z movements over more than 1 m range, thereby placing FoV at any position and of variable size and detail between X-ray source and detector. The X-ray source is an open microfocal transmission anode which provides X-ray spot sizes down to 1 μm. The X-ray projections of the sample are recorded on a digital detector array which covers an area of 40 cm×40 cm (Varian PaxScan). The sample is mounted vertically on the object table and the RoI is positioned on the marked positions covering 5 cm FoV which are sampled at 22.4 μm/voxel (geometric magnification 4.45×). Binning of two detector pixels results in the final effective voxel edge length of 45 μm. Reconstruction of the volume images from 3000 projections is achieved through standard Feldkamp back-projection.

In addition to the low and medium resolution scans of RoI A2, A3.1, A3.2, A4 and A5, we applied high resolution local tomography to the same sample. The RoI A3.3 covers the region marked by the elongated red box in Fig. 3. The RoI CT scanner MetRIC (see Fig. 2) has been designed and constructed recently at the EZRT in Würzburg, Germany. The X-ray source is an X-RAY WorX microfocus transmission anode (XWT-190-THCE PLUS) which can be operated at up to 190 kV acceleration voltage and provides a spot size down to below 1 μm with the high-resolution target (1 μm W on 250 μm Be). The setup comprising source, sample manipulator, and detector offers 10° of freedom and a precisely encoded positioning of the sample and probed RoI. The flat-panel detector (PerkinElmer Dexela 1512 NDT, 14-bit CMOS, Gd_2O_2S:Tb DRZS-scintillation screen) features a pixel size of 74.8 μm on a sensitive area of 154.4 mm×114.9 mm. Especially the extended movement of up to 2.5 m of the detector stack along the horizontally oriented X-ray direction as well as of the X-ray source (up to 1.3 m) enhances an optimized arrangement of encoded source, sample, and detector positions for well-balanced magnification (source-object-distance/source-detector-distance), resolution and scanning time of each sample and RoI. The encoding of all axes enables CT scans without manual movement of the sample and the RoI can be reproduced at any time. The encoded x-y-stage on top of the rotary table as well as the z-movement of the sample stack allow for selection of several RoI without repositioning the sample. Consequently, all data is generated automatically in the same coordinate system.

Our scanner allows for an extensive focus-detector distance (here 3.3 m) which in turn enables voxel samplings as small as 3 μm/voxel,

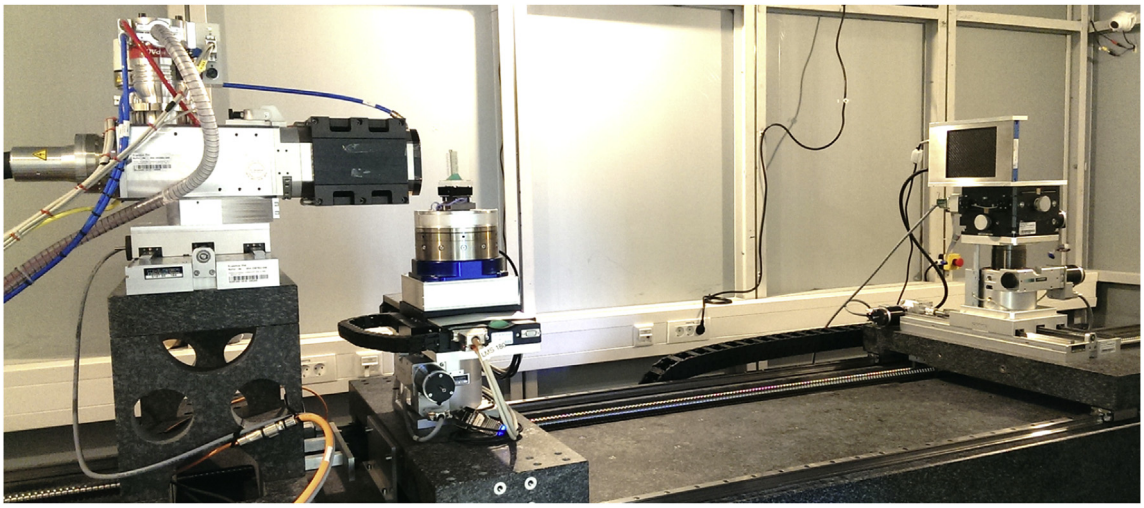

Fig. 2. RoI CT scanner MetRIC at EZRT in Würzburg.

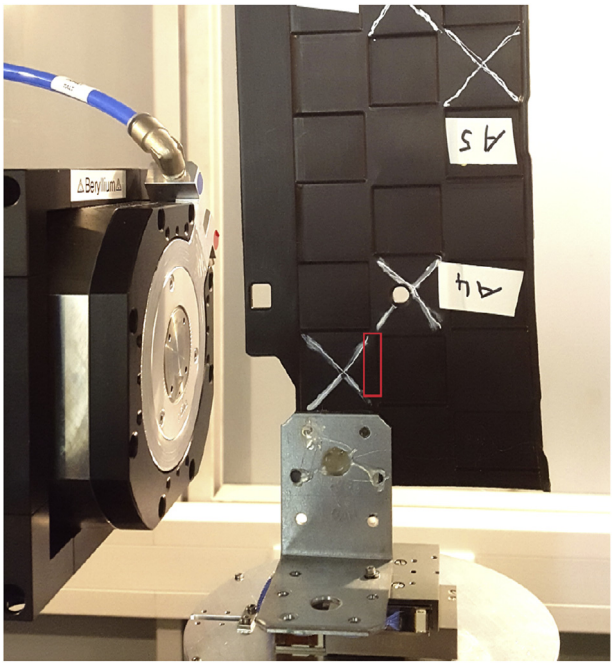

Fig. 3. The red box marks the RoI which has been scanned at finest resolution, divided into six sub-volumes. The stack of six scans covers approximately the entire red box. Fig. 4(a) shows the volume rendering of the segmented fiber component of the whole RoI A3.3. (For interpretation of the references to color in this figure legend, the reader is referred to the Web version of this article.)

even in parts which are several cm wide. Moreover, on top of the air bearing rotation, a piezo positioning system lets the user choose an arbitrary RoI with sub-µm precision.

The minimum resolution of all CT scanners depends on the sample size. Tomosynthesis as well as MetRIC enable resolutions down to 2–3 µm. Tomosynthesis offers additionally the option to scan very large samples with high resolution. On the other hand, MetRIC has a smaller focal spot size reaching even higher resolutions for smaller samples. The degree of freedom for movements and total distances is higher and thus allows more variable sample geometries.

Although the 3D volume reconstruction of RoI CT data gives the chance to achieve high resolution images, it suffers from a few specific problems. If an area of the scanned object overlaps the reconstructable FoV in direction of the beam at a certain angle, this area will become part of the corresponding radiography. Therefore, in the image reconstruction process, this outer area will become part of the reconstructed volume. Moreover, problems occur when the projection of the scanned object is bigger than the horizontal detector size. Filtered back-projection of the radiographies involves high-pass filtering. As a consequence, the detector edge leads to reconstruction artifacts near the boundaries of the imaged volume.

Both problems are treated adequately at MetRIC. The scan is performed “on-the-fly” using a non-stop rotational movement. That way, parts of the sample that are located outside the FoV will move faster during object rotation. Hence, the blurring of these areas is increased proportional to their distance to the center of rotation. In the resulting image slices, this leads to a constant gray value offset only. The horizontal overlap is handled by padding as the high-pass filter used for backprojection is less sensitive of the projected image. Thus, cupping artifacts in the outer areas of the reconstructed slices are avoided.

2.2. Measuring local fiber orientation from 3D image data

In this paragraph, we shortly summarize the method for local 3D fiber orientation analysis based on 2nd order gray value derivatives. That is, the method based on an eigenvalue analysis of the Hessian matrix in each voxel of a 3D image.

State of the art methods for analyzing the fiber orientation in µCT images of FRP parts determine the fiber orientation in each voxel without need to identify individual fibers [32,33,38,42]. More precisely, in each voxel belonging to the fiber system, a local fiber orientation is derived. These voxel-wise measurements yield the volume weighted orientation distribution of the fiber system observed in the 3D image. As discussed in the Introduction, in general, segmenting individual fibers requires higher resolutions than the voxel-wise orientation analysis. The latter being reported to work at spatial sampling of the fiber diameter by 2–3 voxels [8,37,38], allows for an FoV considerably larger than required for single fiber analysis.

Here however, in the coarser scans, the mean fiber diameter of approximately 10 µm is sampled by less than one voxel. Due to the local orientations not rapidly changing spatially, local orientation analysis is nevertheless possible, see [43] analyzing bundles of glass fibers in sheet molding compound samples at a nominal resolution of 17.3 µm in virtual 2D slices using the method from [29,34] applying the structure tensor [32] to prepreg platelet compression molded samples for 3D orientation analysis at 50 µm nominal resolution. The gray value of an image voxel represents in that case the averaged energy absorbed by several neighboring fibers.

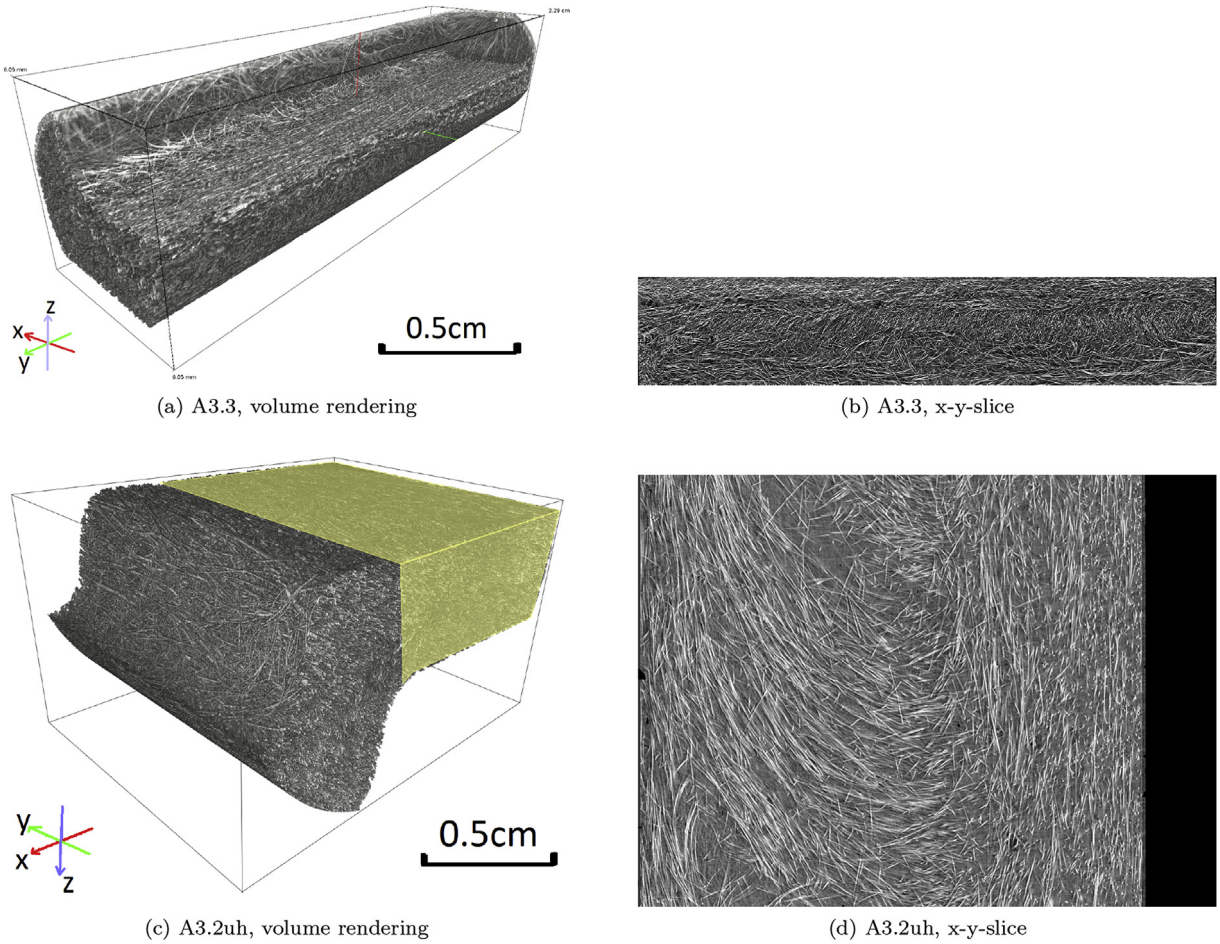

(a) A3.3, volume rendering

(b) A3.3, x-y-slice

(c) A3.2uh, volume rendering

(d) A3.2uh, x-y-slice

Fig. 4. Visualizations of the reconstructed CT images of RoI A3.3 and A3.2uh, with pixel sizes of 3 and 10 μm, respectively.

2.3. Local fiber orientation analysis

The regions scanned are not simply cuboidal. Thus, first of all, masks for the RoI of the part are derived from the CT image data. To this end, solid matter is separated from the surrounding air by a manually chosen global gray value threshold. The resulting rough edges are smoothed by a morphological opening with a 3×3×3 voxel cube.

The local orientations are measured in each voxel exploiting the second order partial derivatives of the local gray values. That is, the Hessian matrix is computed in each voxel. Subsequent analysis of the eigenvalues of the Hessian yields the local orientation of bright locally fiber like structures as the eigenvector corresponding to the smallest (in magnitude) eigenvalue. Following [33], we define a fiber like structure to be a subset of a dilated random fiber system which in turn is a collection of rectifiable curves. See [44,45] for mathematical background. The idea behind the eigenvalue analysis is that standing on a (gray value) mountain ridge, the orientation of the ridge is the one in which the (gray value) relief is curved the least [46]. In [33], this method has been proven to be equivalent to the structure tensor based one of [32] and to outperform methods discretizing the orientation space, namely orientation derived from maximal response of anisotropic Gaussian filters [29] or from the moments of intertia [30].

Here, the Hessian matrix based method is slightly altered. In [33], the fiber diameter is assumed to be known. Calculation of the 2nd order partial gray value derivatives in each voxel is proceeded by smoothing with a Gaussian filter whose parameter is chosen to meet exactly the fiber radius. This choice is motivated by the interpretation of a bright glass fiber within a darker matrix forming a ridge in the gray value relief and the desire to observe the highest points of the ridge exactly at the center line of the fiber. Recent experiments [42] shed some doubt on this empirically deduced rule of thumb and this issue is currently being investigated. Clearly, choosing the width of the Gaussian as the fiber diameter is impossible if the diameter is resolved with less than 3 voxels. Thus, in these cases, a minimal smoothing filter with a 3×3×3 voxel mask approximating a Gaussian is used.

The presented local orientation analysis is based on the mathematical concept of the typical point of a random closed set [15,18,47]. Very roughly speaking, one looks at the world from a point chosen “uniformly” within the random set. As long as the fibers are of equal thickness and do not intersect, the resulting distribution of the fiber orientation in this typical point is the same as if just the one-dimensional fiber cores are taken into account. Let R be the distribution of the local fiber orientation in the typical point. That is, R is a probability measure on the space of direction – the upper half-sphere S^2_+. The 2nd order orientation tensor [10] can be interpreted as the 2nd moment of R. Let $u_i, \quad i \in \{x, y, z\}$ denote the component of some normalized direction vector u in coordinate direction i. Then the second order orientation tensor is defined as (a_{ij}) with

$$a_{ij} = \int_{S^2_+} u_i u_j \, R(du), \quad i, j \in \{x, y, z\}, \tag{1}$$

see [33].

Finally, the local orientation information is exploited for those voxels assigned to the fiber system by a global gray value threshold, only. This threshold is found by multiplying Otsu's threshold [48] by 1.25, the rationale behind that being that the observed orientation distribution is not distorted if voxels at the fiber edges are systematically not taken into account.

An eigenvalue analysis for the 2nd order orientation tensor yields

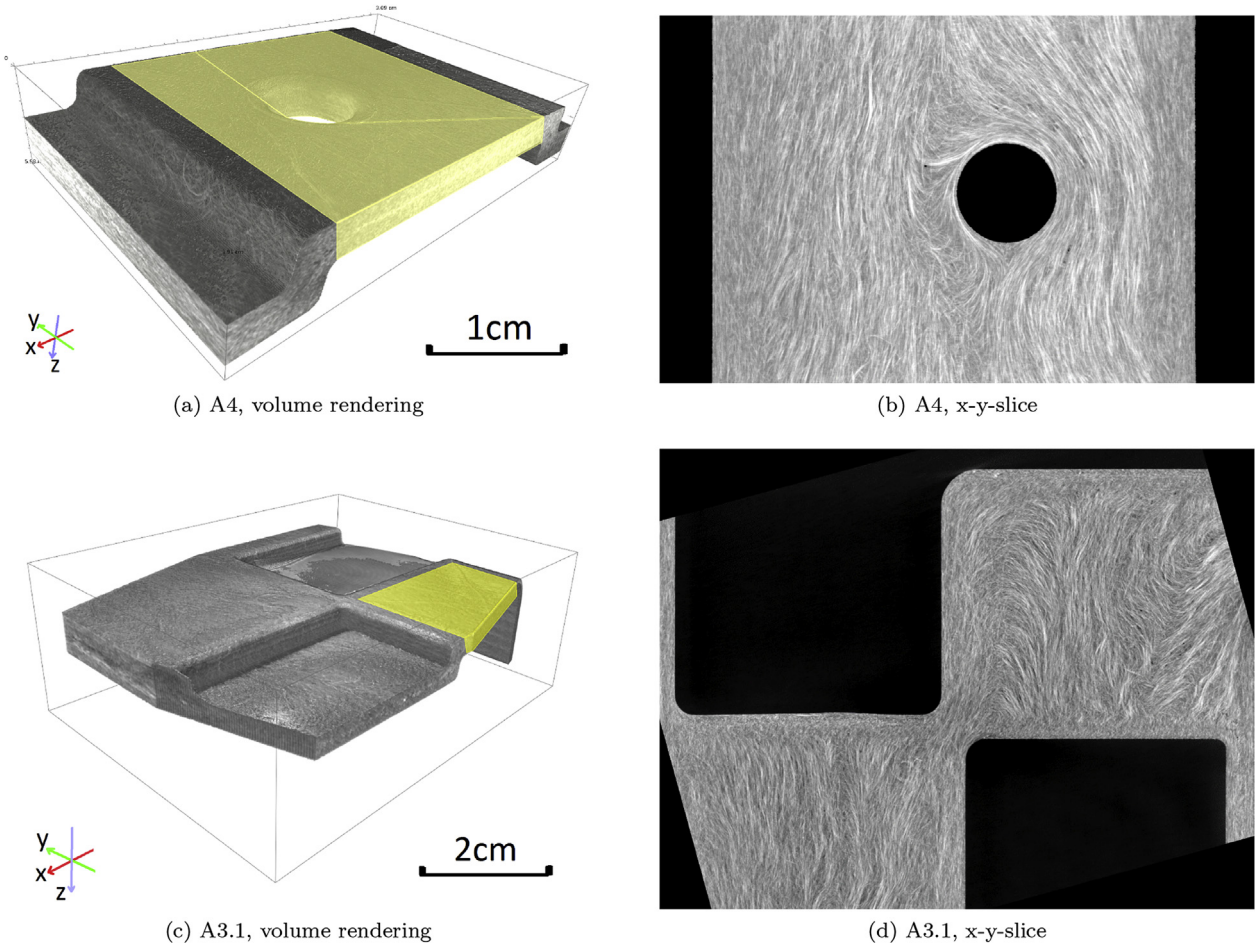

(a) A4, volume rendering

(b) A4, x-y-slice

(c) A3.1, volume rendering

(d) A3.1, x-y-slice

Fig. 5. Visualizations of the reconstructed CT images of RoI A4 and A3.1, with pixel sizes of 17 and 44 µm, respectively.

Table 2
Orientation analysis results for the entire RoI, as specified in Table 1. Note that the mean fiber direction is indicative only if the anisotropy index exceeds 0.6. The respective vectors are therefore not reported if the anisotropy is below this bound.

RoI	mean fiber direction	anisotropy index	orientation tensor a_{xx}, a_{yy}, a_{zz}	voxel size [µm]
A2	not applicable	0.55	0.52, 0.23, 0.23	45
A3.1	not applicable	0.55	0.25, 0.51, 0.23	44
A3.2m	$(-0.07,\ 0.99,\ -0.00)^T$	0.61	0.23, 0.54, 0.21	45
A3.2h	$(-0.08,\ 0.99,\ -0.02)^T$	0.60	0.22, 0.54, 0.22	21
A3.2uh	$(-0.06,\ 0.99,\ -0.05)^T$	0.65	0.21, 0.58, 0.21	10
A3.3	$(-0.06,\ -0.\ 99,\ -0.03)^T$	0.78	0.18, 0.66, 0.17	3
A3.3.1	$(-0.11,\ -0.99,\ 0.03)^T$	0.75	0.18, 0.63, 0.18	3
A3.3.2	$(-0.03,\ -0.99,\ -0.03)^T$	0.78	0.16, 0.67, 0.16	3
A3.3.3	$(-0.08,\ -0.99,\ -0.04)^T$	0.76	0.18, 0.64, 0.16	3
A3.3.4	$(-0.05,\ -0.99,\ -0.05)^T$	0.78	0.17, 0.65, 0.16	3
A3.3.5	$(-0.04,\ -0.99,\ -0.04)^T$	0.77	0.18, 0.63, 0.17	3
A3.3.6	$(0.01,\ 0.99,\ 0.04)^T$	0.77	0.19, 0.63, 0.17	3
A4	not applicable	0.50	0.26, 0.48, 0.24	17
A5	not applicable	0.57	0.22, 0.51, 0.25	44

the preferred local direction as the eigenvector to the largest eigenvalue $\ell_{\max}$ as well as an index reflecting the strength of anisotropy [43]. More precisely, consider $\alpha = 1 - \ell_{\min}/\ell_{\max}$, where $\ell_{\min}$ is the smallest eigenvalue of the orientation tensor. This index assumes values in the range [0,1] with 0 indicating perfect isotropy. A value of 1 is achieved in two cases - perfect unidirectional fibers or a transversally isotropic fiber system. Tensile tests for glass FRP reported in [43] suggest that samples with $\alpha < 0.6$ behave as isotropic samples. Thus calculating a mean fiber direction is not sensible in this case.

3. Results

Here, we present first the results of the RoI CT scans by volume renderings and slice views in Section 3.1. The following Section 3.2 contains the 3D orientation analysis results, both locally as well as averaged for each region. Finally, for regions A3.2 and A3.3, local fiber orientations deduced from the image data are compared for several resolutions in Section 3.3 and for A3.3 to those obtained by numerical simulation of the injection molding process, see Section 3.4.

All orientations are analyzed in 3D, in each voxel, see [37]. There, the Hessian matrix based method is applied to data of FRP samples showing pixel-wise orientation results. In [49], the authors discussed the existing problems and challenges around the visualization of volumetric microstructures by means of FRP. Size and complexity of the imaged regions necessitate a reduction of orientation information. Here, we concentrate on the orientation tensor diagonal element a_{yy} as the y-direction is the dominating one. Therefore, results are averaged in cubic sub-volumes and often 2D slices or projections are chosen for better illustration. Sub-volume sizes are nevertheless chosen with particular attention to formed layers, so called shell and core layers [50–52], in the components' microstructure.

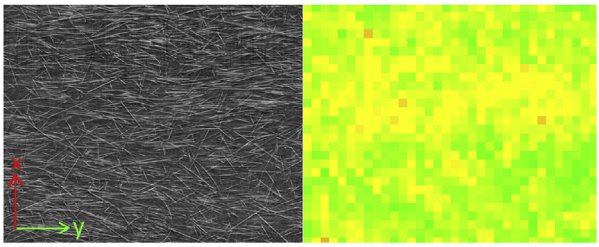

(a) A3.2uh, upper layer

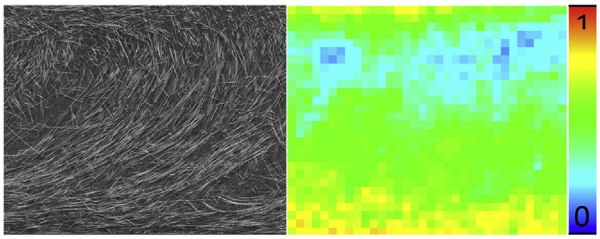

(b) A3.2uh, center layer

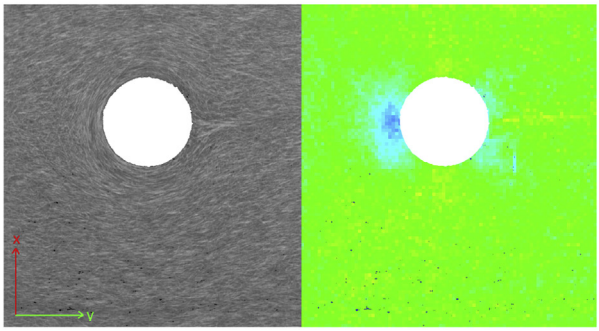

(c) A4, upper layer

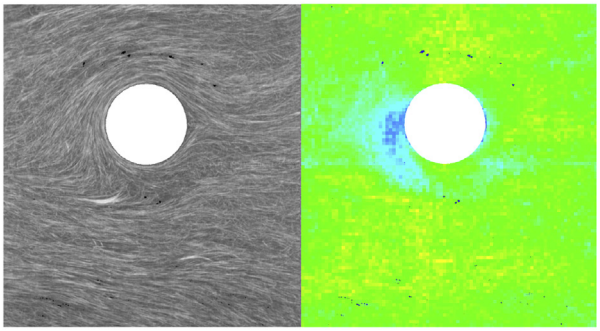

(d) A4, center layer

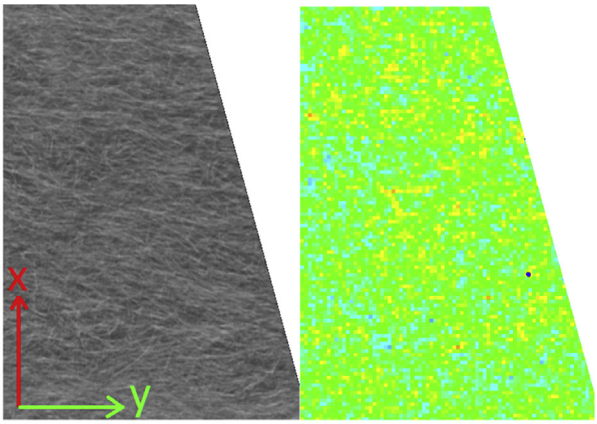

(e) sub-sample of A3.1, upper layer

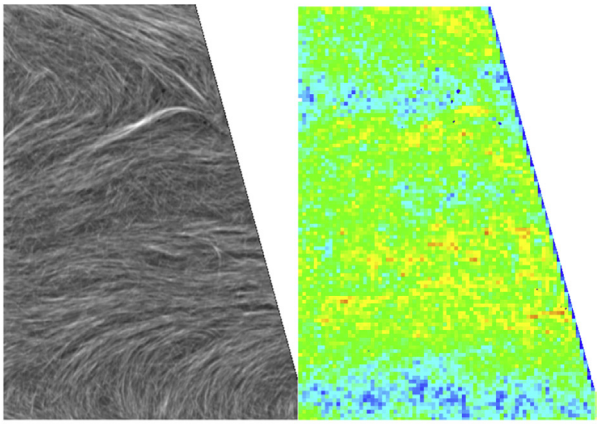

(f) sub-sample of A3.1, center layer

Fig. 6. Orientation estimation results for three regions marked yellow in Figs. 4 and 5. 2D slices from the original 3D images and from the image holding the corresponding computed local tensor component a_{yy} are shown next to each other. The orientation tensors are computed in cubic sub-volumes of $(218\,\mu m)^3$ for all data sets. (For interpretation of the references to color in this figure legend, the reader is referred to the Web version of this article.)

Fig. 7. A3.3, cropped to the plate region, resulting in a $1\,200 \times 8\,832 \times 1\,000$ voxel sub-volume. The area closest to the reader is close to an edge where fibers are forced to bend.

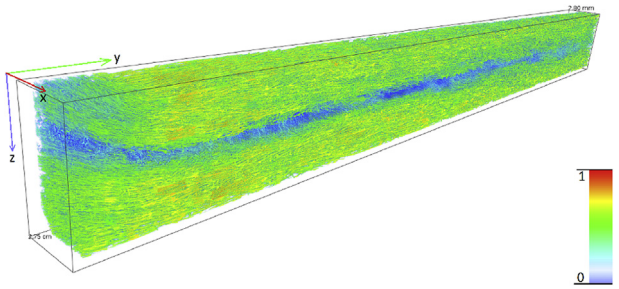

Fig. 8. Clipped visualization of the evaluated area. The orientation tensor component a_{yy} is shown in the analyzed sub-volumes of edge length 65 pixels (about 200 µm) leading to a grid of 17×135×13 cubes. Averaged over the whole analyzed volume, the orientation tensor diagonal components are $a_{xx} = 0.20$, $a_{yy} = 0.63$, $a_{zz} = 0.15$. The anisotropy index is 0.75 and the mean fiber direction $(-0.00,\ -0.99,\ -0.01)^T$.

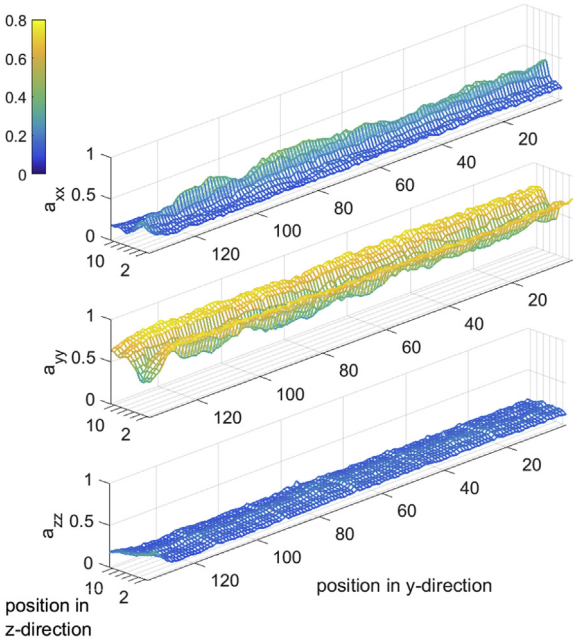

Fig. 9. Orientation tensor diagonal components for the RoI scan A3.3. The mesh is based on the analysis in 135×13 sub-volumes, where the results are averaged over 17 sub-volumes along the x-axis.

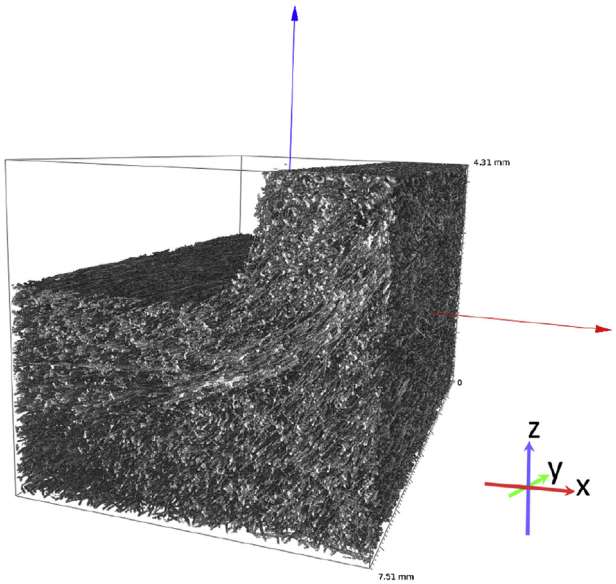

Fig. 10. Volume rendering of the sub-volume used for the comparison in Fig. 11.

3.1. RoI CT scans

Altogether, four regions are scanned. Region A3 is scanned five times with A3.1, A3.2m, A3.2h, A3.2uh, and A3.3 being ordered w.r.t. ascending resolution. See Table 1 for dimensions and voxel sizes.

Figs. 4 and 5 give a visual impression of a representative selection of the analyzed scans. Volume renderings and 2D slices of RoI A3.2uh, A4 and A3.1 reveal the differences in acquired data caused by varying resolutions and the micro-structure in the imaged RoI respectively. The data sets are cascaded in Figs. 4 and 5 starting at the finest resolution and getting coarser towards the bottom. Simultaneously this cascade emphasizes the differences in the sample volume covered by the RoI, too. The 2D slices in Figs. 4 and 5 are taken from the central layer of the plate. All scans are subsequently analyzed. However, local orientation analysis results are visualized only for the selected regions marked yellow in Figs. 4 and 5.

3.2. Local fiber orientation tensors from 3D image analysis

The computed orientation results are summarized in Table 2. We derive the fiber component as described in Section 2.2. The orientation tensors are computed based on a tiling by cubes of size 218 µm×218 µm×218 µm. Clearly the y-direction is preferred (long axis of the carrier) for regions A3.1, A3.2, A3.3 and A5. In RoI A4, the y-direction is less dominant due to the reorientation around the hole in this region. RoI A2 is a special case as the component's shape differs significantly from the remaining plate-like shape in this spur region. A2 features a_{xx} as the highest component. This finding is not surprising due to x being the longitudinal direction of the spur, see Fig. 1.

In the following Fig. 6, we show the local orientation results for the regions marked yellow in Figs. 4 and 5. The Figure shows slices from the upper (left) and central (right) layers of the plate like sub-regions. The color map visualizes the orientation tensor diagonal element a_{yy} in flow direction y. For all resolutions, as expected, fiber orientations cluster around the flow direction in the upper layer and deviate stronger from this preferred direction in the central layer. Note that the orientation results in Table 2 are averaged over the entire regions. Thus, fibers being reoriented along the edges due to shaping are taken into account, too. This might decrease the anisotropy index as well as the dominating diagonal orientation tensor element. The yellow marked regions are tightly limited to the areas in plane and thus avoid the reorientation of fibers due to shaping procedures. Orientation results for these regions are visualized in Fig. 6 for the coarse resolution scans and the sequence of Figs. 7–9 for the finest resolution scan.

Figs. 7 and 8 show the 'edge' in region A3 which was scanned at the highest resolution (3 µm/voxel). The orientation tensor is averaged in boxes of edge length 200 µm. The expected central layer deviating from the dominating y-orientation [6] is clearly visible in the rendering. Fig. 9 shows the orientation tensor diagonal elements, averaged along the x-axis of the shown volume. These graphs reveal that the central layer has a pronounced x-orientation (a_{xx} rising from 0.2 to approximately 0.5 along the entire strap) at the expense of y-alignment (dropping from 0.6 to 0.3) while the $a_{zz} \approx 0.2$ tensor component is constant over the entire thickness (Fig. 9(c)). Moreover, Fig. 7 indicates a slight reorientation of fibers at one ending of the elongated volume. This visual impression is backed by Fig. 9. Clearly, fibers are oriented mostly in plane in the first 120 sub-volumes along the y-axis in contrast to the last 15 sub-volumes, where higher a_{zz} values are observed. This is exactly where the fibers are reoriented due to shaping.

3.3. Comparison of local fiber orientation tensors derived from scans at varying resolutions

In order to compare the local orientations derived from scans at varying lateral resolutions quantitatively, we chose a sub-volume of A3 that is covered by several scans. More precisely, the chosen volume lies in the intersection of the RoIs A3.3, A3.2uh, A3.2h, and A3.2m, scanned with voxel sizes 3–45 µm. See Fig. 10 for a volume rendering. We averaged the orientation results in sub-volumes of edge-length 200 µm and subsequently along the y-axis in order to preserve the characteristic differences between shell and core layers. Fig. 11 shows the remarkable consistency of the orientation results even for the coarsest resolution at 45.3 µm. Nevertheless, the quality of orientation results drops for the coarser resolutions. This becomes obvious by the lower color contrasts between shell and core layers from left to right. Moreover, the component a_{zz} orthogonal to the plate varies the most when resolved at 45.3 µm. These two observations clearly show a bias towards isotropy in the analysis results.

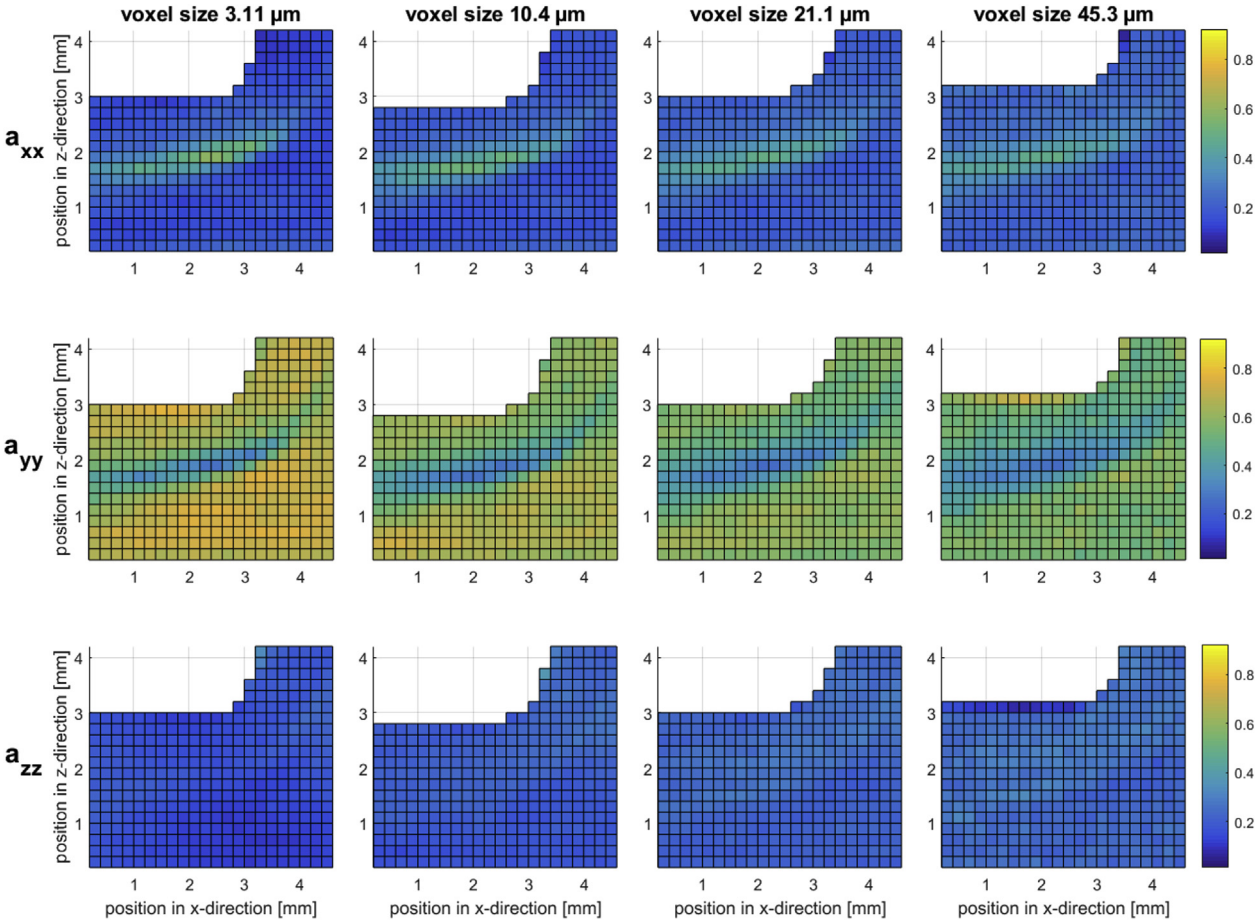

Fig. 11. Comparison of local results for varying voxel sizes: Orientation tensor diagonal components for the RoI scan, color coded. A volume rendering of the corresponding sub-volume is shown in Fig. 10. (For interpretation of the references to color in this figure legend, the reader is referred to the Web version of this article.)

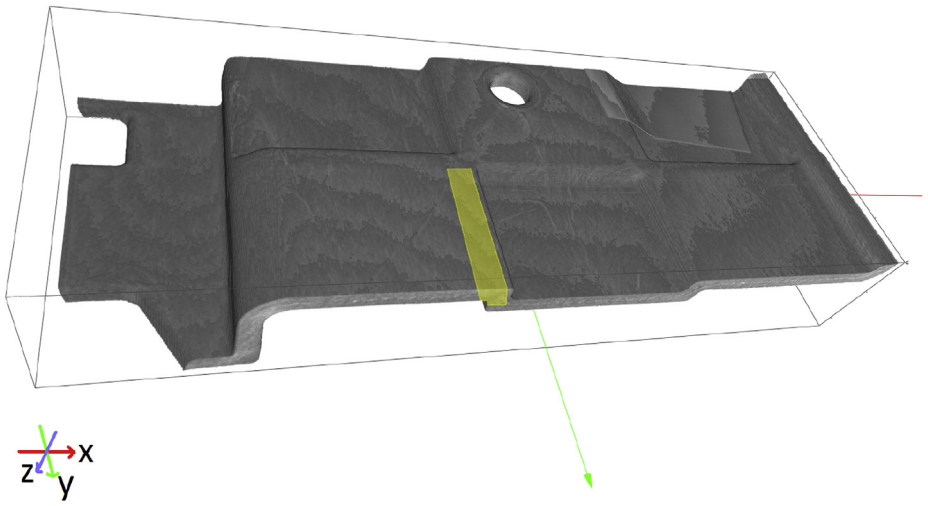

Fig. 12. Visualization of a coarse CT scan around RoI A3.3 (marked yellow) that has been used for injection simulation. (For interpretation of the references to color in this figure legend, the reader is referred to the Web version of this article.)

3.4. Comparison to local fiber orientation tensors from injection molding simulation

For three sub-regions of A3, we compare the 2nd order orientation tensors calculated in the previous section with the values obtained by Moldflow® simulations. The region is highlighted in yellow in Fig. 12.

The compared positions p_1 to p_3 are marked by triangles and rectangles in Fig. 13 for simulation and µCT data respectively. The tetrahedral Moldflow mesh can be seen in Fig. 13 along with three tetrahedra for which we calculated orientation tensors for comparison with the results from µCT.

The used mesh size is app. 2 mm (element edge length in-plane). 12 layers are used over the part thickness (out-of-plane) for the calculations. The entire carrier has around 17 0000 elements using Dual

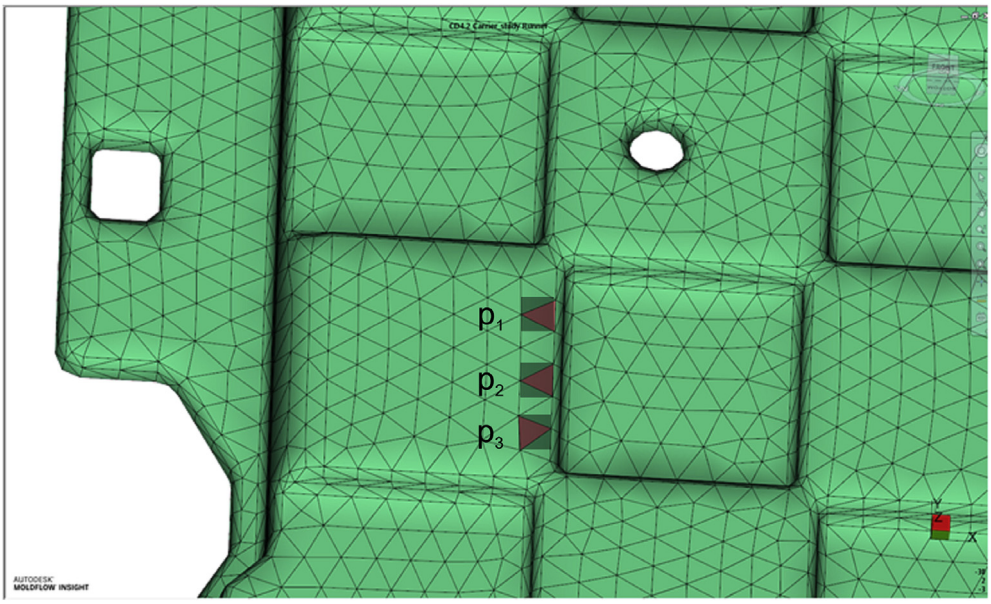

Fig. 13. Mesh of the area around A3.3 that has been used for injection simulation in the software Autodesk Moldflow Insight 2017. p_1, p_2 and p_3 mark the positions where the simulation results have been extracted. The simulated orientation tensor is averaged in the marked triangle, whereas the analysis based on the CT data averages in cubes.

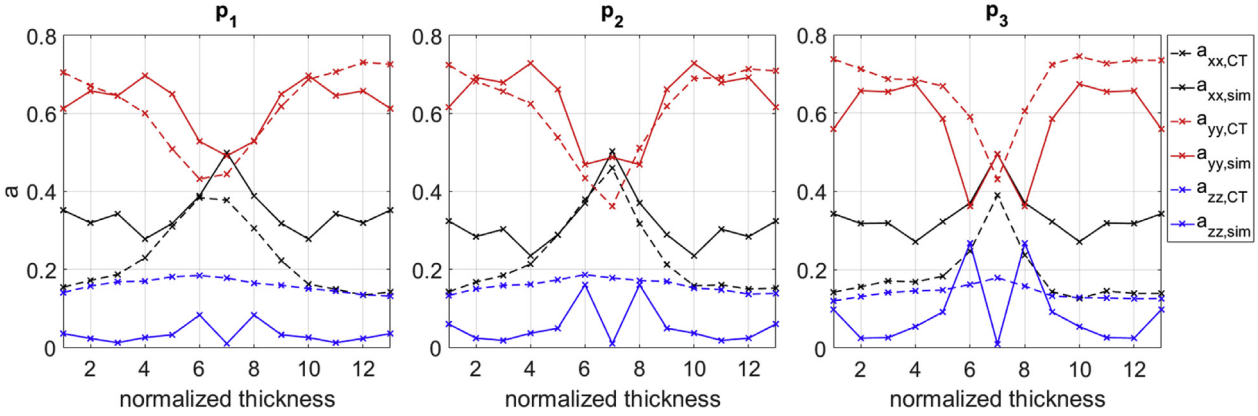

Fig. 14. Comparison of simulated and CT image data based orientation tensors for region A3.3.

Domain mesh. For the orientation calculation, the Moldflow Rotational Diffusion model is used [53]. Its parameters – fiber interaction coefficient Ci and coefficients of asymmetry $D1$, $D2$ and $D3$ – are set as "automatic calculations". That is, the default values $D1 = 1.0$, $D2 = 0.8$, $D3 = 0.15$ are used. The µCT data is processed in a way to fit the grid of simulated data. The plate thickness is subdivided in 12 cuboidal sub-volumes. The orientation results are obtained by averaging along x- and y-axis (in plane).

Fig. 14 shows the three diagonal tensor elements a_{xx}, a_{yy}, and a_{zz} from both the simulation and the measurement. The components a_{xx} and a_{yy} agree qualitatively well with a_{xx} peaks in the central layer and decreasing to the outside and a_{yy} showing the opposite behaviour for both methods. The a_{zz} component however is more pronounced in some measurement points in the simulation while it is almost negligible throughout in the measurement with a slight exception around the center of p_3. In particular the a_{yy} and a_{zz} components feature kinks in the central layer that are neither explained by standard flow dynamics nor backed by the µCT measurements.

4. Conclusion

Based on an off-the-shelf part from the automotive industry, we showed that RoI CT is readily applicable to large FRP components provided that the CT scanner has the required motor axes and degrees of freedom. We scanned an injection molded automotive glass FRP component that is 0.9 m long, 0.35 m wide, and has a wall thickness of 2 mm.

It is commonly assumed that a single fiber has to be sampled by at least 2–4 voxels per diameter, see the corresponding discussion in the Introduction. We clearly proved this assumption to be false. Sampling the fiber diameter by less than a voxel still allows for 3D orientation analysis in each voxel predominantly representing the fiber phase. The analysis method of choice gains local orientation information in each voxel from the gray value curvature captured by the Hesse matrix. The results are stabilized by averaging the 2nd order orientation tensor over small sub-volumes. By this method we achieved good and consistent results for voxel sizes between 45 µm and 3 µm for the same material. Measuring the local orientation of individual fibers would require a much higher spatial sampling and therefore impose a much smaller FoV.

The 3D image analysis reveals strong anisotropy in the local fiber orientation. For all RoI except the spur shaped A2, the injection direction y is as expected the preferred one, see Table 2. Local effects like the typical thickness-dependent changes in the mean fiber orientation caused by flow turbulences in the central layer are captured, regardless the image quality, see Figs. 6 and 11. Caution is however advised when it comes to a quantitative comparison as blurred structural information induces a bias of the orientation analysis results towards isotropy, see the right column of Fig. 11. Comparing the analysis results for A3.1 and A3.2, see Table 2, shows that nominal resolution is however not the

decisive parameter here.

For the best resolved RoI μCT scan A3.3, the local fiber orientations observed in the RoI CT data can be compared to those derived by injection molding simulation (Fig. 14). Although deviating quantitatively, the results do agree qualitatively and particularly well for the dominating tensor component. This proves clearly that the measured orientation results can be used to validate simulation results. Thus RoI μCT combined with 3D image analysis as applied here, enables truly non-destructive 3D micro-structure characterization for large FRP components.

To summarize, we proved RoI μCT to be a potential standard tool for local fiber orientation analysis in glass fiber-reinforced automotive parts. Also, we applied successfully the proposed RoI scanning technique in combination with the orientation analysis method to carbon FRP [54]. Our results are very encouraging and suggest that the method is applicable to both short and long fiber reinforced composites. Unlike methods which try to find single individual fibers and which therefore require a very high resolution and consequently cover a very small measurement volume, our method allows the extension of the latter to some 2000 times the fiber diameter, hence 3 cm for 15 μm thick glass fibers.

Acknowledgements

This work has been supported by the Fraunhofer Society under project MEF 3DVolant. DD has been supported by the German Federal Ministry of Education and Research (BMBF) under grant 05M13RCA.

References

[1] H. Andrä, M. Gurka, M. Kabel, S. Nissle, C. Redenbach, K. Schladitz, O. Wirjadi, Geometric and Mechanical Modeling of Fiber-Reinforced Composites, in: D. Bernard (Ed.), Proceedings of the 2nd International Congress on 3D Materials Science, Springer, Cham, 2014, pp. 35–40.
[2] G. Requena, G. Fiedler, B. Seiser, P. Degischer, M. Di Michiel, T. Buslaps, 3D-quantification of the distribution of continuous fibres in unidirectionally reinforced composites, Compos. Appl. Sci. Manuf. 40 (2) (2009) 152–163.
[3] R. Sencu, Z. Yang, Y. Wang, P. Withers, C. Rau, A. Parson, C. Soutis, Generation of micro-scale finite element models from synchrotron X-ray CT images for multi-directional carbon fibre reinforced composites, Compos. Appl. Sci. Manuf. 91 (2016) 85–95.
[4] F. Heieck, F. Hermann, P. Middendorf, K. Schladitz, Influence of the cover factor of 2d biaxial and triaxial braided carbon composites on their in-plane mechanical properties, Compos. Struct. 163 (2017) 114–122.
[5] M.J. Emerson, K.M. Jespersen, A.B. Dahl, K. Conradsen, L.P. Mikkelsen, Individual fibre segmentation from 3D X-ray computed tomography for characterising the fibre orientation in unidirectional composite materials, Compos. Appl. Sci. Manuf. 97 (2017) 83–92.
[6] H. Andrä, D. Dobrovolskij, K. Schladitz, S. Staub, R. Müller, Modeling of Geometrical Microstructures and Mechanical Behaviour of Constituents, in: S. Diebels, S. Rjasanow (Eds.), Multi-Scale Simulation of Composite Materials. Results from the Project MuSiKo, Springer, Berlin Heidelberg, 2019.
[7] C. Hannesschläger, V. Revol, B. Plank, D. Salaberger, J. Kastner, Fibre structure characterisation of injection moulded short fibre-reinforced polymers by X-ray scatter dark field tomography, Case Stud. Nondestruct. Test. Eval. 3 (2015) 34–41.
[8] O. Wirjadi, M. Godehardt, K. Schladitz, B. Wagner, A. Rack, M. Gurka, S. Nissle, A. Noll, Characterization of multilayer structures in fiber reinforced polymer employing synchrotron and laboratory X-ray CT, Int. J. Mater. Res. 105 (7) (2014) 645–654.
[9] A. Ayadi, H. Nouri, S. Guessasma, F. Roger, Determination of orthotropic properties of glass fibre reinforced thermoplastics using X-ray tomography and multiscale finite element computation, Compos. Struct. 136 (2016) 635–649.
[10] S. Advani, C. Tucker, The use of tensors to describe and predict fiber orientation in short fiber composites, J. Rheol. 31 (8) (1987) 751–784.
[11] H. Miled, L. Silva, J.F. Agassant, T. Coupez, Numerical simulation of fiber orientation and resulting thermo-elastic behavior in reinforced thermo-plastics, In: Mechanical Response of Composites. Computational Methods in Applied Sciences, 10 Springer, Dordrecht, 2008, pp. 293–313.
[12] S. Fliegener, T. Kennerknecht, M. Kabel, Investigations into the damage mechanisms of glass fiber reinforced polypropylene based on micro specimens and precise models of their microstructure, Compos. B Eng. 112 (2017) 327–343.
[13] A. Bernasconi, F. Cosmi, P. Hine, Analysis of fibre orientation distribution in short fibre reinforced polymers: a comparison between optical and tomographic methods, Compos. Sci. Technol. 72 (16) (2012) 2002–2008.
[14] S. Schmidt, D. Niedziela, K. Steiner, J. Zausch, CoRheoS, Multiphysics solver framework and simulation infrastructure for complex rheologies, Proceedings of Nafems World Congress 2013, Salzburg, Austria, 2013.
[15] D. Stoyan, W.S. Kendall, J. Mecke, Stochastic Geometry and its Applications, second ed., Wiley, Chichester, 1995.
[16] B. Mlekusch, E. Lehner, W. Geymayer, Fibre orientation in short-fibre-reinforced thermoplastics I. Contrast enhancement for image analysis, Compos. Sci. Technol. 59 (4) (1999) 543–545.
[17] C. Eberhardt, A. Clarke, Fibre-orientation measurements in short-glass-fibre composites. Part I: automated, high-angular-resolution measurement by confocal microscopy, Compos. Sci. Technol. 61 (10) (2001) 1389–1400.
[18] J. Ohser, K. Schladitz, 3d Images of Materials Structures – Processing and Analysis, Wiley VCH, Weinheim, 2009.
[19] D. Salaberger, K.A. Kannappan, J. Kastner, J. Reussner, T. Auinger, Evaluation of computed tomography data from fibre reinforced polymers to determine fibre length distribution, Int. Polym. Process. 26 (3) (2011) 283–291.
[20] M. Teßmann, S. Mohr, S. Gayetskyy, U. Haßler, R. Hanke, G. Greiner, Automatic determination of fiber-length distribution in composite material using 3D CT data, EURASIP J. Appl. Signal Process. 1 (2010) 545030 2010.
[21] M. Kronenberger, K. Schladitz, B. Hamann, H. Hagen, Fiber segmentation in crack regions of steel fiber reinforced concrete using principal curvature, Image Anal. Stereol. 37 (2) (2018) 127–137.
[22] C. Eberhardt, A. Clarke, Automated reconstruction of curvilinear fibres from 3d datasets acquired by X-ray microtomography, J. Microsc. 206 (1) (2002) 41–53.
[23] K. Sandau, J. Ohser, The chord length transform and the segmentation of crossing fibres, J. Microsc. 226 (1) (2007) 43–53.
[24] H. Altendorf, Analysis and Modeling of Random Fiber Networks, in: J.B.T.M. Roerdink (Ed.), PhD Thesis, TU Kaiserslautern and Mines ParisTech, 2012.
[25] H. Shen, S. Nutt, D. Hull, Direct observation and measurement of fiber architecture in short fiber-polymer composite foam through micro-ct imaging, Compos. Sci. Technol. 64 (13) (2004) 2113–2120.
[26] T. Mishurova, N. Rachmatulin, P. Fontana, T. Oesch, G. Bruno, E. Radi, I. Sevostianov, Evaluation of the probability density of inhomogeneous fiber orientations by computed tomography and its application to the calculation of the effective properties of a fiber-reinforced composite, Int. J. Eng. Sci. 122 (2018) 14–29.
[27] P. Pinter, B. Bertram, K.A. Weidenmann, Novel Method for the Determination of Fibre Length Distributions from μCT-data, Proc. 6th Conf. on Industrial Computed Tomography (iCT), Wels, Austria, 2016.
[28] J. Viguié, P. Latil, L. Orgéas, P. Dumont, S.R. du Roscoat, J.-F. Bloch, C. Marulier, O. Guiraud, Finding fibres and their contacts within 3d images of disordered fibrous media, Compos. Sci. Technol. 89 (2013) 202–210.
[29] K. Robb, O. Wirjadi, K. Schladitz, Fiber orientation estimation from 3d image data: practical algorithms, visualization, and interpretation, Proc. 7th Int. Conf. Hybrid Intelligent Systems, Kaiserslautern, Germany, 2007, pp. 320–325.
[30] H. Altendorf, D. Jeulin, 3d directional mathematical morphology for analysis of fiber orientations, Image Anal. Stereol. 28 (3) (2009) 143–153.
[31] O. Wirjadi, K. Schladitz, A. Rack, T. Breuel, Applications of anisotropic image filters for computing 2d and 3d-fiber orientations, in: V. Capasso, G. Aletti, A. Micheletti (Eds.), Stereology and Image Analysis - 10th European Congress of ISS, Milan, Italy, 2009, pp. 107–112.
[32] M. Krause, J. Hausherr, B. Burgeth, C. Herrmann, W. Krenkel, Determination of the fibre orientation in composites using the structure tensor and local X-ray transform, J. Mater. Sci. 45 (4) (2010) 888–896.
[33] O. Wirjadi, K. Schladitz, P. Easwaran, J. Ohser, Estimating fibre direction distributions of reinforced composites from tomographic images, Image Anal. Stereol. 35 (3) (2016) 167–179.
[34] B.R. Denos, D.E. Sommer, A.J. Favaloro, R.B. Pipes, W.B. Avery, Fiber orientation measurement from mesoscale ct scans of prepreg platelet molded composites, Compos. Appl. Sci. Manuf. 114 (2018) 241–249.
[35] E. Belmonte, M. De Monte, T. Riedel, M. Quaresimin, Local microstructure and stress distributions at the crack initiation site in a short fiber reinforced polyamide under fatigue loading, Polym. Test. 54 (2016) 250–259.
[36] F. Prade, F. Schaff, S. Senck, P. Meyer, J. Mohr, J. Kastner, F. Pfeiffer, Nondestructive characterization of fiber orientation in short fiber reinforced polymer composites with x-ray vector radiography, NDT E Int. 86 (2017) 65–72.
[37] C. Redenbach, A. Rack, K. Schladitz, O. Wirjadi, M. Godehardt, Beyond imaging: on the quantitative analysis of tomographic volume data, Int. J. Mater. Res. 2 (2012) 217–227.
[38] P. Pinter, S. Dietrich, B. Bertram, L. Kehrer, P. Elsner, K. Weidenmann, Comparison and error estimation of 3d fibre orientation analysis of computed tomography image data for fibre reinforced composites, NDT E Int. 95 (2018) 26–35.
[39] A. Wonisch, A. Wüst, More precise part design: accurate simulation of fiber orientation of glass fiber-reinforced plastics, Kunststoffe International (2014) 80–83.
[40] S.C. Garcea, Y. Wang, P. Withers, X-ray computed tomography of polymer composites, Compos. Sci. Technol. 156 (2018) 305–319.
[41] D. Bull, S. Spearing, I. Sinclair, L. Helfen, Three-dimensional assessment of low velocity impact damage in particle toughened composite laminates using micro-focus X-ray computed tomography and synchrotron radiation laminography, Compos. Appl. Sci. Manuf. 52 (2013) 62–69.
[42] D. Dobrovolskij, J. Persch, K. Schladitz, G. Steidl, Structure detection with second order Riesz transform, Image Anal. Stereol. 38 (1) (2019) 107–119.
[43] K. Schladitz, A. Büter, M. Godehardt, O. Wirjadi, J. Fleckenstein, T. Gerster, U. Hassler, K. Jaschek, M. Maisl, U. Maisl, S. Mohr, U. Netzelmann, T. Potyra, M. Steinhauser, Non-destructive characterization of fiber orientation in reinforced SMC as input for simulation based design, Compos. Struct. 160 (2017) 195–203.
[44] J. Mecke, W. Nagel, Stationäre räumliche Faserprozesse und ihre Schnittzahlrosen, Elektron. Informationsverarb. Kyb. 16 (1980) 475–483.

[45] W. Nagel, Dünne Schnitte von stationären räumlichen Faserprozessen, Math. Operationsforsch. Stat., Ser. Stat 14 (1983) 569–576.
[46] D. Eberly, R. Gardner, B. Morse, S. Pizer, C. Scharlach, Ridges for image analysis, J. Math. Imaging Vis. 4 (4) (1994) 353–373.
[47] R. Schneider, W. Weil, Stochastic and Integral Geometry, Probability and its Applications, Springer, Heidelberg, 2008.
[48] N. Otsu, A threshold selection method from gray level histograms, IEEE Trans. Systems, Man and Cybernetics 9 (1979) 62–66.
[49] J. Weissenböck, A. Amirkhanov, W. Li, A. Reh, A. Amirkhanov, E. Gröller, J. Kastner, C. Heinzl, Fiberscout: an interactive tool for exploring and analyzing fiber reinforced polymers, 2014 IEEE Pacific Visualization Symposium, IEEE, 2014, pp. 153–160.
[50] P. Hine, R. Duckett, P. Caton-Rose, P. Coates, Fibre orientation structures and their effect on crack resistance of injection moulded transverse ribbed plate, Plastics, rubber and composites 33 (1) (2004) 43–53.
[51] M. De Monte, E. Moosbrugger, M. Quaresimin, Influence of temperature and thickness on the off-axis behaviour of short glass fibre reinforced polyamide 6.6–cyclic loading, Compos. Appl. Sci. Manuf. 41 (10) (2010) 1368–1379.
[52] M. De Monte, E. Moosbrugger, M. Quaresimin, Influence of temperature and thickness on the off-axis behaviour of short glass fibre reinforced polyamide 6.6–quasi-static loading, Compos. Appl. Sci. Manuf. 41 (7) (2010) 859–871.
[53] H.-C. Tseng, R.-Y. Chang, C.-H. Hsu, Comparison of recent fiber orientation models in injection molding simulation of fiber-reinforced composites, J. Thermoplast. Compos. Mater. (2018), https://doi.org/10.1177/0892705718804599.
[54] S. Zabler, K. Schladitz, K. Dremel, J. Graetz, D. Dobrovolskij, Region-of-interest X-ray tomography for the non-destructive characterization of local fiber orientation in large fiber composite parts, 22nd Symposium on Composites, Key Engineering Materials, 809, Trans Tech Publ, 2019, pp. 587–593.